



MOMENTUM EXCHANGE BETWEEN ATMOSPHERE, SEA ICE AND OCEAN

by

Giulia Castellani

A thesis submitted in partial fulfillment of the
requirements for the degree of

**Doctor of Philosophy
in Geosciences**

Approved Dissertation Committee:

Prof. Dr. **Rüdiger Gerdes**

Prof. Dr. Michael Bau

Dr. Martin Losch

Dr. Christof Lüpkes

Date of Defense:
13 November 2014

“Il grado di libertà di un uomo si misura dall'intensità dei suoi sogni.”
-A. MERINI-

“The degree of freedom of a man is measured by the intensity of his dreams.”

Abstract

The Arctic is experiencing ongoing dramatic changes. The strongest evidence of these changes is in the sea ice. The ice cover showed a reduction in areal extent and total volume. Older ice is giving space to new and thinner ice, and large surface topographic elements are disappearing accompanied by an increase of melt ponds and smaller topographic features. Moreover, the sea ice, which is not a stationary cover but moves in response to external forcing, showed an increase in drift speed over the last 30 years. The ice is coupled to the ocean and the atmosphere by exchanging heat and momentum, thus changes in sea ice may affect the other two components through mechanisms that are not fully understood yet.

In the light of these recent changes, a good understanding of the factors determining the lifetime, movement and evolution of the ice is becoming necessary, together with a proper investigation of the coupling of sea ice with atmosphere and ocean. It is known that the intensity of the atmosphere-ice and ocean-ice interactions depend on the roughness of the separation interface; the roughness of the ice surface is determined by the concentration and shape of the topographic elements.

The aim of this thesis is to estimate the momentum fluxes over the entire Arctic Basin as function of sea-ice topography. The present study splits in two parts: as first the momentum fluxes between atmosphere and ice and between ice and ocean are estimated based on real topography data. Then the results are upscaled with numerical simulations. This second step allows also to evaluate the impact of a more detailed physical description of the atmosphere-ice-ocean interactions on the ocean circulation.

The study based on sea-ice topography data showed a high variability in space and time of the ice surface, such variability is then reflected in the momentum fluxes. The concentration of large and small topographic elements differs from region to region according to the age of ice and to the deformation history. In particular, this study revealed that considering only the large topographic elements is not enough to characterize the degree of deformation of an ice field and thus to evaluate the strength of the air-ice-ocean interactions.

The model study showed that by introducing a topography dependent description of the atmosphere-ice-ocean interaction, the sea ice is affected in its thickness, areal

extent and drift. Moreover, changes in the ice topography affect the ocean to a large extent: the ocean shows changes not only in the surface circulation, but also in the circulation of the deeper Atlantic water. This reveals that in order to obtain correct predictions for the future of the Arctic a better description of subgrid processes, like the formation of surface roughness elements and their impact on the drag coefficients, is needed.

Contents

1	Introduction	1
1.1	The Arctic and its Ocean	3
1.2	Sea Ice	5
1.2.1	Sea-Ice Topography	7
1.2.2	Sea-Ice Drift	8
1.3	Aim of the Present Work	10
1.4	Data and Methods	10
1.4.1	Sea-Ice Surface Topography and Drag Coefficients	10
1.4.2	Numerical Models	12
1.4.3	Representation of Sub-Grid Processes	15
1.5	Overview of the Scientific Papers	16
2	Paper I	19
	Variability of Arctic Sea Ice Topography and its Impact on the Atmospheric Surface Drag	
2.1	Introduction	20
2.2	Data and Methods	22
2.2.1	Methods for Estimating Sea Ice Topography and Selected Data Sets	22
2.2.2	Processing of Laser Profiles	23
2.2.3	Parameterization of Drag Coefficients	25
2.3	Results	28
2.3.1	Surface Topography	28
2.3.2	Drag Coefficients	32
2.4	Discussion	41
2.5	Summary and Conclusion	43

3	Paper II	45
	Impact of Sea Ice Bottom Topography on the Ekman Pumping	
3.1	Introduction	46
3.2	Data and Methods	47
3.3	Calculation of Oceanic Drag Coefficients	49
3.4	Ekman Pumping	51
3.5	Summary and Conclusion	52
4	Paper III	55
	Sea Ice Drag as Function of Deformation and Ice Cover: Effects on Simulated Sea Ice and Ocean Circulation in the Arctic	
4.1	Introduction	56
4.2	Methods	58
4.2.1	Model Description and Setup	58
4.2.2	Parameterization of Atmospheric and Oceanic Drag Coefficients	59
4.3	Results	61
4.3.1	Simulated Deformation Energy and Drag Coefficients	62
4.3.2	Sea Ice	63
4.3.3	Ocean	67
4.4	Discussion	69
4.4.1	Sensitivity to Different Constant Drag Coefficients	73
4.5	Summary and Conclusion	75
5	Conclusion	79
5.1	Outlook	81
	Bibliography	85
	Acknowledgments	99

Chapter 1

Introduction

“The whole surface of the ice was a chaos of movement. It looked like an enormous jigsaw puzzle, the pieces stretching away to infinity and being shoved and crunched together by some invisible but irresistible force. The impression of its titanic power was heightened by the unhurried deliberateness of the motion. Wherever two thick floes came together, their edges butted and ground against one other for a time. Then, when neither of them showed signs of yielding, they rose, slowly and often quiveringly, driven by the implacable power behind them. Sometimes they would stop abruptly as the unseen force affecting the ice appeared mysteriously to lose interest. More frequently, though, the two floes -often 10 feet thick or more- would continue to rise, tenting up, until one or both of them broke and toppled over, creating a pressure ridge.

Endurance, Shackleton’s Incredible Voyage

-A. Lansing-

Shackleton and his crew spent over a year on the Antarctic sea ice after their ship, the “*Endurance*”, was captured and crushed by the ice. During their stay, they had to move constantly to find better ice floes where to camp. The presence of pressure ridges created a big obstacle to their migration on the ice, but also a refuge from the wind and a good lookout for sighting the presence of animals.

But what is this “invisible and irresistible force” that acts on the ice field? And what do these pressure ridges mean for the lifetime, movement and evolution of the sea ice? The last decades revealed an increasing interest in the sea ice and in its future. Nowadays, we know that the deformation of sea ice, and thus the appearance of topographic elements such as pressure ridges, is an indicator of the action of wind and of ocean currents. Moreover, we know that the more deformed is the ice field, the more effective will be the force exerted by the wind blowing on it. Thus, starting from the time of the first polar expedition, we have learnt that sea-ice deformation

is the result of the ice motion, but also that the sea-ice motion is itself affected by the surface roughness.

Nevertheless, many questions are still waiting for an answer. Through which mechanisms does the sea-ice roughness influence the ice movement? How is the coupling with the atmosphere and the ocean affected by the topographic elements on the ice? What do we expect for the future of sea ice in terms of deformation degree and movement of the ice field?

In this PhD thesis I investigate how the presence of topographic elements, such as pressure ridges, affect the strength of the atmosphere-ice and ice-ocean interactions. I focus on the Arctic Basin since sea ice in this region showed the largest changes over the last decades. In the light of recent climate changes, the investigation of the atmosphere-ice-ocean dynamic interaction represents one step towards a better understanding of the future of our planet.

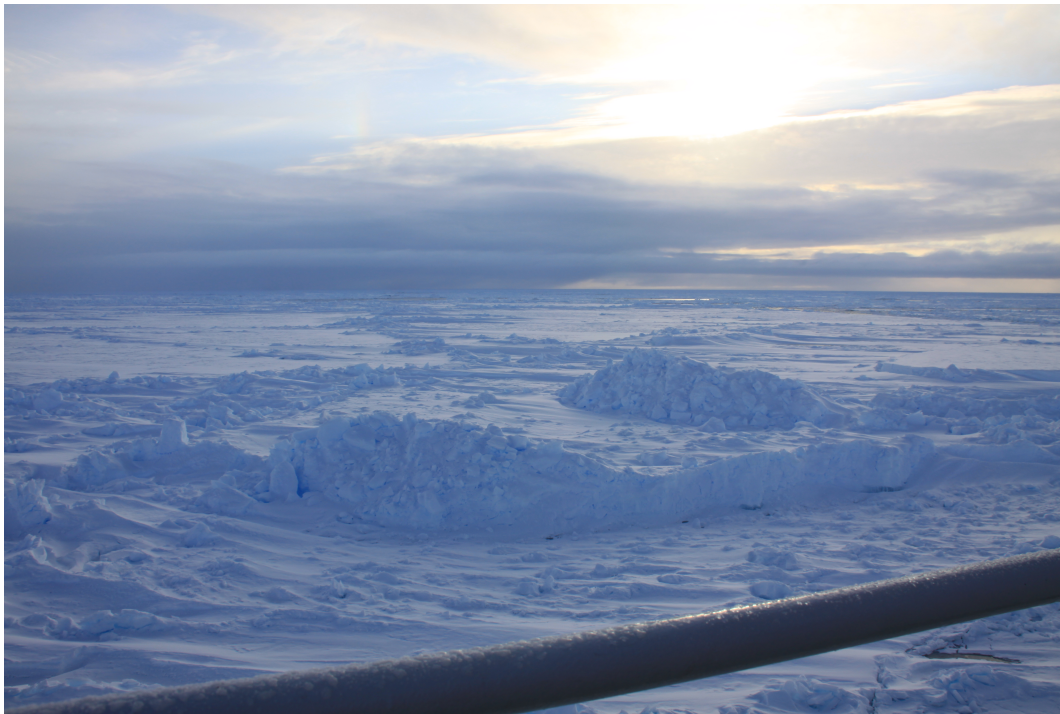


Figure 1.1: Topographic structures as result of deformation events in an ice field. Photo taken during the *RV Polarstern* cruise ANTXXIX/9 in the Weddell Sea by Giulia Castellani.

This thesis is organized in the following. The introductory chapter presents the background information and the motivation of this study. In particular, Sections 1.1 and 1.2 introduce the geographic environment that creates the frame of this study. Section 1.3 presents the aim of this work and Section 1.4 gives an overview of the available data and of the methods used for the investigation. Section 1.5 contains an introduction to the scientific papers that represent the three main chapters (Chapter 2, 3, and 4) of this thesis.

Finally, Chapter 5 gives a summary of the thesis and the main findings of this PhD project.

1.1 The Arctic and its Ocean

The Arctic is defined as the region north of the Arctic Circle ($66^{\circ} 33' \text{ N}$). The Arctic Ocean is enclosed by the land masses of Europe, Asia and North America (see Figures 1.2 and 1.4). It includes the Greenland Sea, the Iceland Sea and the Norwegian Sea (the Nordic Seas). The Arctic Ocean occupies an area of $9.4 \times 10^6 \text{ km}^2$ (*Rudels, 2004*) and has an average depth of 1361 m with a maximum of 5260 m located near the Gakkel Ridge of the Eurasian basin (*Jakobsson, 2002*).

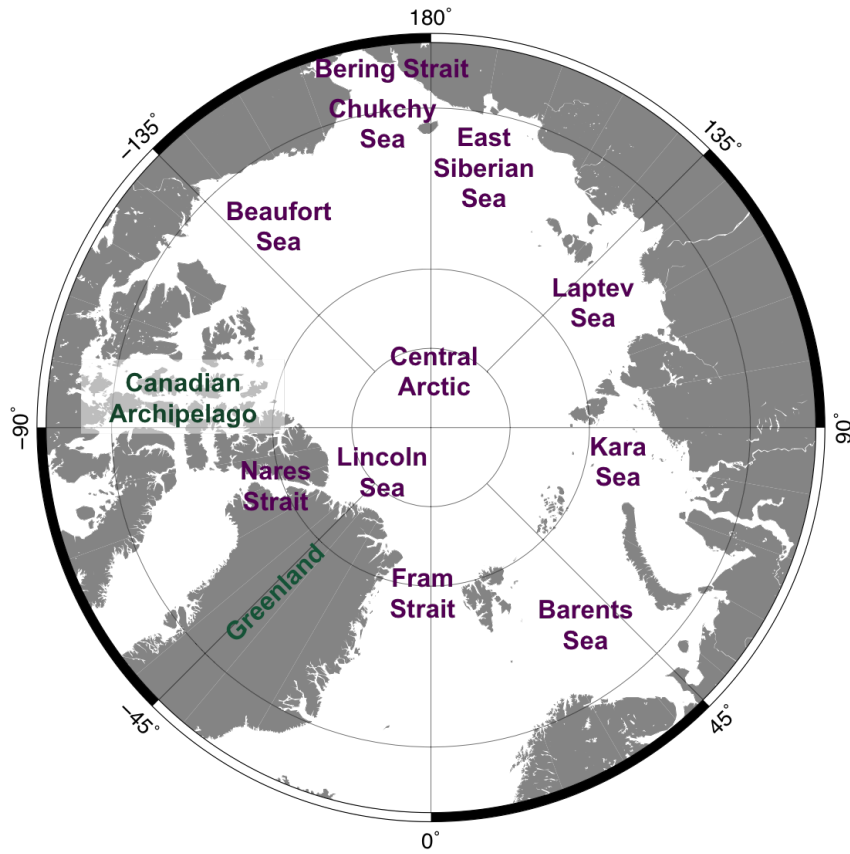


Figure 1.2: Map of the Arctic Ocean and its Seas.

The deep basin of the Arctic Ocean is divided into the Canadian and Eurasian basins by the Lomonosov Ridge that, at a depth of about 1400 m, divides the deep water masses (*Lewis E. L., 1982*). The Eurasian Basin is further divided into the Nansen Basin ($\sim 4000 \text{ m}$ deep) and the Amundsen Basin ($\sim 4500 \text{ m}$ deep) by the Gakkel Ridges, while the Canadian Basin is separated by the Alpha Ridge and the

Mendeleyev Ridge into the Makarov (~ 4000 m deep) and the Canada Basin (~ 3800 m deep). A large part of the Arctic Basin, 53 %, consists of shallow shelves: the Barents Sea (200-300 m), the Kara Sea (50-100 m), the Laptev Sea (< 50 m), the East Siberian Sea (< 50 m) and the Chukchi Sea (50-100 m). The Arctic Ocean is connected to the other world oceans by three topographic gaps (*Thomas and Dieckmann, 2010*): the Fram Strait, the Bering Strait and the channels between the Canadian Archipelago.

Most of the water masses in the Arctic Ocean (79 %) originates in the Atlantic Ocean and only 19 % in the Pacific Ocean. The fresh water contributes 2 % of the entire water masses, which is a large contribution compared to other oceans.

The Arctic Ocean is a strongly salinity stratified ocean, its vertical structure is characterized by a mixed layer extending from the surface to a depth of 30-50 m; below this layer and until a depth of about 150-200 m the water is well stratified (*Carmack, 2000*). In this stratified layer lie both the Pacific and Atlantic haloclines (Figure 1.3).

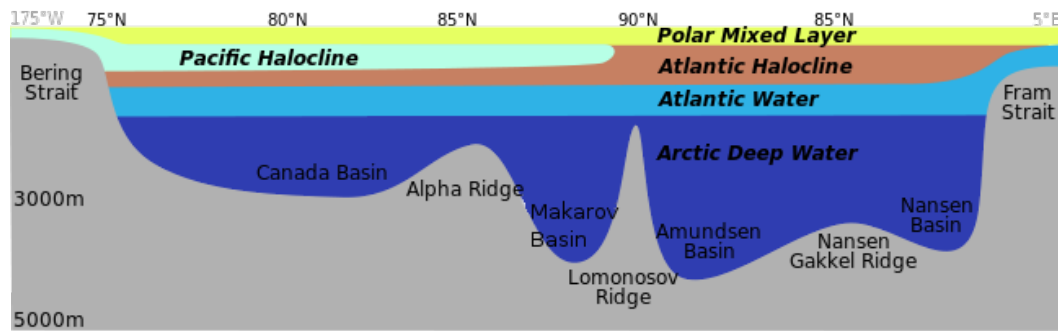


Figure 1.3: Vertical stratification of the Arctic Ocean. Credit: Florian Greil, University of Houston.

Underneath this layer and until about 1200 m, there is the Atlantic Water Layer (AWL) (*Aagaard et al., 1981; Aagaard, 1989; Rudels et al., 1994; Karcher et al., 2007*), a layer of warm and saline water flowing from the Atlantic Ocean into the Eurasian basin through the Fram Strait. Finally, beneath the AWL there is the deep water that is prevented from circulating freely below 1400 m by the Lomonosov ridge.

Surface waters move in response to wind forcing (*Rudels, 2004*). In particular, the interannual variability in strength and location of the ocean surface current system components depends on the Sea Level Pressure (SLP) over the Amerasian Basin and North Atlantic (*Proshutinsky and Johnson, 1997*) (See also Section 1.2.2). The upper ocean circulation shows two characteristic patterns: an anticyclonic Gyre in the Canada Basin, known as Beaufort Gyre, and a Transpolar Drift (TPD) which carries waters from the Canada Basin and the Siberian shelves towards the Fram Strait (see also Figure 1.6).

Atlantic water primarily enters the Arctic Basin in the West Spitzbergen Current (WSC) through the Fram Strait and in small part also via the Barents Sea through the Franz Joseph Land-Novaya Zemlya passage (*Aagaard, 1982*) (Figure 1.4). Before entering the central Arctic Basin, the Atlantic water loses its characteristics of saline and warm water by melting sea ice and mixing with fresh water of Arctic origin (*Beszczyńska-Möller et al., 2012*). The temperature of the Atlantic water decreases from 7-10 °C at the entrance in the Nordic Sea to 3-3.5 °C when entering the Arctic Ocean through Fram Strait (*Beszczyńska-Möller et al., 2012*). The Atlantic Water forms cyclonic gyres in the Makarov and Canada Basin (*Aagaard, 1989; Rudels et al., 1994*). In particular, in the Canada Basin the surface anticyclonic circulation contrasts the cyclonic circulation of the AWL that occurs mainly following the shelf breaks. During its passage through the Arctic basin, the warm Atlantic water loses heat and this is associated with vertical fluxes that affect the ice distribution and concentration in different selected areas of the central Arctic.

River runoff and the low salinity Pacific water are the main sources of liquid fresh water into the Arctic Ocean. In the central Arctic, changes in the fresh water content can affect the stability of the water column with consequences for the heat transfer and for the depth of the mixed layer. Once the fresh water is exported through the Fram Strait and the Canadian Archipelago into regions of deep water formation in the Nordic Seas and in the North Atlantic, it has an effect on the large scale ocean circulation such as the Atlantic Meridional Overturning Circulation and the horizontal gyres (*Rabe et al., 2011; Gerdes et al., 2008; Brauch and Gerdes, 2005*). Freshwater exists also in the form of sea ice. This relatively thin layer of ice is transported over long distances (*Köberle and Gerdes, 2003; Martin and Gerdes, 2007*) thus changing the distribution of fresh water in the central Arctic. *Dickson et al. (1988)* and *Häkkinen (1993)* showed that the export of sea ice from the Arctic Ocean can have important consequences for the equilibrium of the thermohaline circulation; evidence of this are events like the "Great Salinity Anomaly" in the 1970s (*Köberle and Gerdes, 2003*). Thus, the mechanisms regulating the drift of the sea ice, as well as its changes in velocity and direction, represent key parameters in the investigation of the equilibrium of the Arctic Ocean and of the global ocean circulation.

1.2 Sea Ice

During all seasons, a large part of the Arctic Ocean is covered by sea ice. Sea ice is subject to local growth and melt, horizontal transport and deformation. All these processes alter the thickness of the ice and its spatial distribution, and involve the exchange and transport of mass and energy with the atmosphere and the oceans.

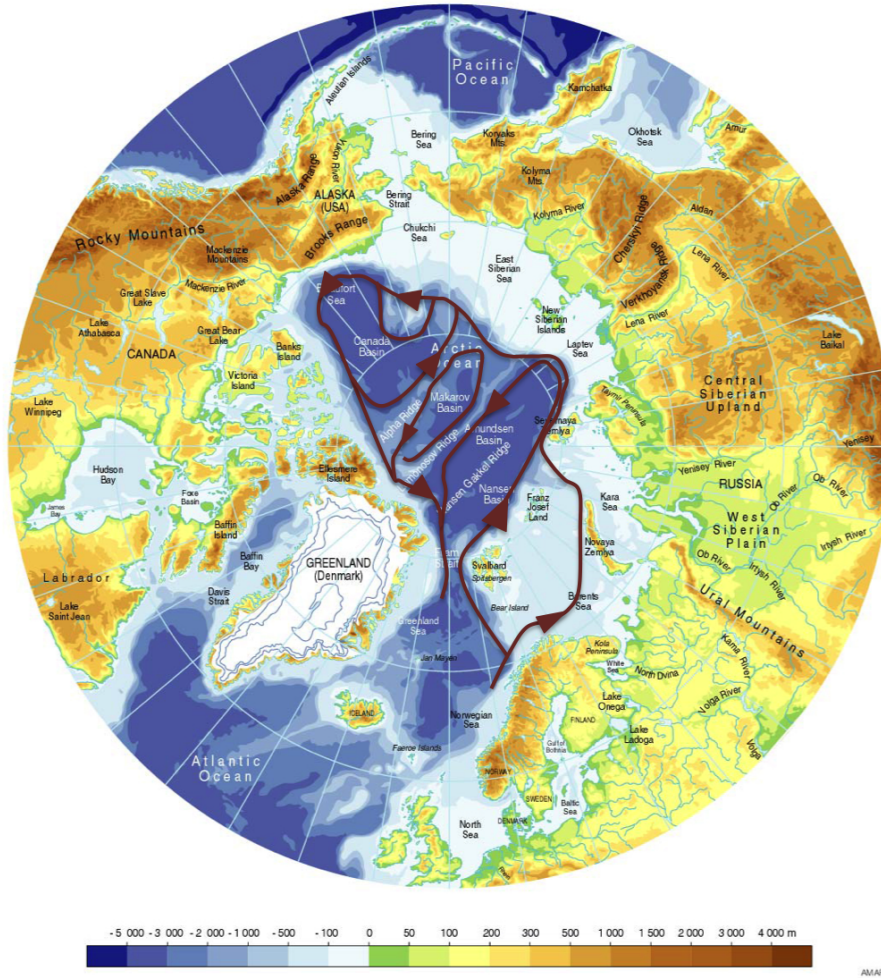


Figure 1.4: Bathymetry of the Arctic basin. Image taken from *AMAP Assessment Report* (1998). The red arrows illustrate schematically the main pattern of the Atlantic water circulation.

The presence of sea ice in polar regions affects the atmosphere, the oceans and the climate of our planet (*McPhee*, 2008). Sea ice insulates the ocean from the cold polar atmosphere, reduces the outgoing longwave radiation from the ocean and limits the convective heat exchange. Because of its bright color compared to sea water, sea ice reflects a much higher portion of incoming short wave radiation than open water. The ratio between reflected and incoming solar radiation is called *albedo*, thus the sea ice has a higher albedo than the ocean. During ice formation, salt is rejected into the ocean creating cold and saline water that has low buoyancy. This cold and saline water sinks in narrow plumes to depth where it is buoyant. These depths can be below the halocline thus the result of this process is a change in the density of the ocean. Driven by wind, sea ice can drift long distances, carrying its reservoir of fresh water and thus affecting the salt distribution. Finally, during the drift of sea ice a drag is exerted between ice and ocean promoting the formation of several

phenomena, such as upwelling, downwelling and Ekman transport (*Ekman*, 1905). The main physical parameters describing the large-scale sea-ice cover are: concentration, thickness and drift; but other small scale features can also reflect large scale trends in sea ice. In particular, topographic characteristics of the ice are the results of deformation events and are important for the ice-atmosphere and ice-ocean interactions.

Arctic sea ice showed a strong reduction in areal extent and in thickness (*Parkinson and Cavalieri*, 2012; *Serreze et al.*, 2003, 2007; *Haas et al.*, 2008; *Stroeve et al.*, 2007; *Kwok et al.*, 2009; *Kwok and Rothrock*, 2009; *Stroeve et al.*, 2011; *Winton*, 2011), together with a loss of older and thick ice (*Maslanik et al.*, 2007; *Kwok et al.*, 2009; *Comiso*, 2012; *Rabenstein et al.*, 2010). Moreover, it was documented in recent years that the sea-ice drift speed increased over the last three decades (*Rampal et al.*, 2009; *Sprenn et al.*, 2011; *Kwok et al.*, 2013; *Olason and Notz*, 2014).

In the light of these recent changes, more and more attention has been paid to the reasons and consequences of changing sea ice. The effort of the scientific community addresses the improvement of the available observations, in terms of amount and accuracy, as well as model simulations of Arctic sea ice. In the line with this investigation, the present PhD work focuses on improving our knowledge of the atmosphere-ice-ocean interaction and on the feedback mechanisms between them, by using both observations and model simulations.

1.2.1 Sea-Ice Topography

Besides the large scale physical parameters of the ice (concentration, thickness and drift), there are other small scale properties that distinguish the sea ice in different areas of the Arctic Ocean. First Year Ice (FYI) is distinguished from Multi Year Ice (MYI). The latter is defined to have survived the summer melt and its average thickness is about 3-4 meters (*Wadhams and Comiso*, 1992). The FYI is newly formed ice, its thickness is less than the multi year ice and it has a lower albedo. The larger albedo of MYI is due to a higher vapor bubble density and a thicker scattering layer at the surface that increases the capacity of reflecting the incoming shortwave radiation (*Maykut*, 1986). Besides thickness and albedo, MYI and FYI differ in salt content and vertical salt distribution, in crystal structure and layers and in surface topography. The surface topography of the ice is the result of the deformation history of an ice field.

There are two main types of deformation taking place in the ice pack: ridging and rafting. During rafting two ice layers slide one over the other without breaking in pieces. On the other hand, when the ice is thick enough (*Parmeter*, 1975), it breaks in blocks that accumulate along the fracture line to form pressure ridges (Figures 1.1 and 1.5a). Ridges consist of two parts: a sail above the sea level and a keel that

extends into the sea water. They are usually much longer than wide and thick, they are made up of fragments of the parent ice and they can incorporate sea water during their formation. Other products of sea-ice deformation are hummocks, rubbles fields (randomly scattered and tilted ice blocks) and piles of ice.

Finally, a phenomenon common in Arctic summer (*Flocco and Feltham, 2007; Flocco et al., 2010*) that contributes to shaping the surface of sea ice, is the formation of melt ponds. These are created by accumulation of water, as consequence of snow and ice melt, on the sea-ice surface (Figure 1.5b).



Figure 1.5: (a) A pressure ridge in the central Arctic. Photo taken during the *RV Polarstern* expedition in summer 2011 by Mario Hoppmann. (b) Melt ponds in the central Arctic. Picture taken from <http://earthobservatory.nasa.gov/>. People are included for a sense of scale.

1.2.2 Sea-Ice Drift

Sea ice is not a stationary cover of the ocean but, at all time, moves as result of the different forces acting on it. The general scheme of sea-ice drift (Figure 1.6) is well established and primarily follows the ocean surface circulation patterns already mentioned in Section 1.1: the Beaufort Gyre and the TPD (*Vinje, 1982*). The Beaufort Gyre is an anticyclonic gyre, typically covering the Beaufort Sea and parts of the central Arctic Ocean between the East Siberian Sea and the North Pole. The Beaufort Gyre causes a recirculation of ice leading to a residence time of more than 10 years in the western Arctic (*Martin, 2007*). The TPD crosses the central Arctic Ocean directed from the Laptev and East Siberian Seas towards the Fram Strait with small branches feeding it from the Lincoln Sea and Kara Sea, thus representing the most important driving factor for the export of ice out of the polar basin southward Greenland. These two main mechanisms are subject to changes due to the variability in the atmospheric circulation and in the atmospheric pressure patters. This variability shows mainly two wind-driven drift regimes: anticyclonic and cyclonic. The anticyclonic drift regime (Figure 1.6a) dominates during winter and it is characterized by a larger and stronger Beaufort Gyre, covering large part

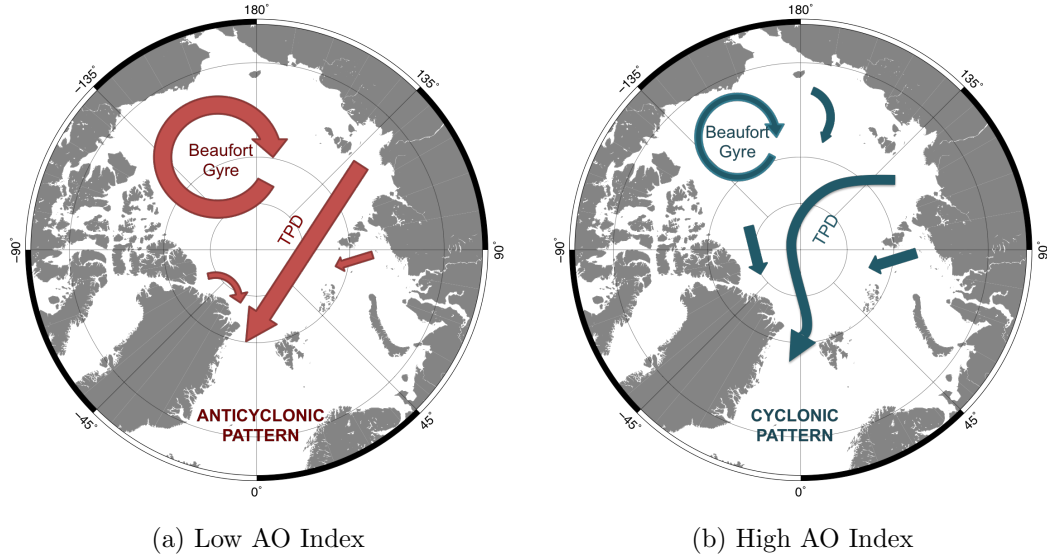


Figure 1.6: Sea-ice drift. Figure a) shows the anticyclonic pattern with a strong Beaufort Gyre and a straight Transpolar Drift (TPD). Figure b) shows the cyclonic pattern with a weaker Beaufort Gyre that causes an extension of the TPD towards the West Arctic.

of the Canadian Basin (*Proshutinsky et al.*, 2002). The cyclonic drift regime (Figure 1.6b) is common in summer and it is characterized by a weaker Beaufort gyre confined mostly in the Barents Sea, and by a TPD that turns cyclonically over the north pole and it is fed by large branches coming from the Lincoln sea, the Kara Sea and the East Siberian sea.

The alternation of these two regimes is related to the North Atlantic Oscillation (NAO) and the Arctic Oscillation (AO) (*Rigor et al.*, 2002). A strong positive AO leads to a weaker anticyclonic circulation in the Amerasian Basin creating thus the cyclonic pattern (Figure 1.6b). On the other hand, a negative AO is associated with the anticyclonic pattern of the ice drift.

The main physical mechanisms responsible for the ice drift in the Arctic are the direct driving forces of the wind and the ocean currents, the latter usually counteracting the wind forces except in cases of weak winds. Another mechanism that modifies, redistributes and dissipates the driving force energy is the stress gradient within the ice. Near to the coast or in conditions of very compact pack ice, the internal stress can be as large as the forces due to wind and currents. Minor contributions to the sea-ice drift are the Coriolis force, the tilt of the ocean surface, inertia and steady currents (*Hibler and Flato*, 1992).

In the equation that describes the ice motion, the intensity of air-ice and water-ice interactions, and thus the strength of the wind and ocean action, is mathematically expressed through the drag coefficients (see also Section 1.4.2). These must account for the impact of sea-ice surface characteristics on the near-surface transport of

momentum. Because of the spatial and temporal inhomogeneities of the sea-ice surface, we can expect a spatial and temporal variation of the drag coefficients as well.

1.3 Aim of the Present Work

The main aim of this work is to evaluate the momentum fluxes between atmosphere, sea ice and ocean as function of sea-ice topography over the whole Arctic Basin.

The first step in this direction is to investigate the variability of the sea-ice surface and bottom topography in different regions of the Arctic, different years and different seasons. The second step is to assess the variability of the atmospheric and oceanic drag coefficients as function of the concentration and size of the topographic elements. Both goals could be achieved if sufficient observations of sea-ice topography parameters were available.

Since the Arctic is inaccessible during most of the year due to the severe weather conditions, in-situ observations are very sparse and usually confined to spring and summer seasons. In order to upscale the results obtained with in-situ measurements, we can use numerical models since they allow us to perform basin-wide simulations. Also numerical models present several limitations. One such limitation is the inability to represent processes whose spatial scale is smaller than the domain discretization (see also Section 1.4.3). Nevertheless, numerical simulations allow to investigate feedback mechanisms of coupled systems, such as atmosphere, ice and ocean. Thus, numerical models can be used to achieve another aim of the present study i.e., to understand how the performed simulations vary in the representation of ice drift, thickness and concentration when we consider the atmospheric and oceanic drag coefficients variability.

Another aim of the present study is to evaluate to which extent the variations of drag coefficients can affect the ocean circulation. Sea ice is also transmitting and transferring wind stress to the ocean. This stress is responsible for the ocean surface circulation, for the depth of the mixed layer and for the formation of phenomena such as upwelling and downwelling in the ocean interior. The variability of the surface drag can thus translate into a deeper mixed layer and in a stronger or weaker Ekman pumping.

1.4 Data and Methods

1.4.1 Sea-Ice Surface Topography and Drag Coefficients

Measurements of sea-ice topography have been performed over the last decades on different scales and with different methods. We can distinguish three main meth-

ods, namely in-situ observations, remote sensing techniques applied from aircraft, helicopters, ships and moorings, and satellite-based remote sensing.

With in-situ measurements it is possible to collect information on ice properties and also on ice thickness by drilling (*Nortala-Hoikkanen et al.*, 1994). Despite the high spatial resolution, in situ observations cover only small areas. This limitation can be overcome by remote sensing measurements of sea-ice surface topography to obtain ridge statistics (*Ketchum*, 1971), and by Upward-Looking Sonar (ULS) measurements (*Wadhams and Davy*, 1986; *Melling and Riedel*, 1995; *Fissel et al.*, 2004; *Davis and Wadhams*, 1995) of the bottom topography.

Another device, introduced in 2001, is the so-called EM-bird (HEM) (*Haas*, 2004b). This is a combination of an electromagnetic device (EM) which measures the distance to the surface underneath the ice, and a laser for sea-ice surface elevation. These pieces of information are combined to obtain the sea-ice thickness.

The satellite-based remote sensing of sea-ice freeboard and surface properties has undergone many improvements in the last years, mostly with the launch of the two missions ICESat (*Kwok et al.*, 2004) and CryoSat (*Wingham et al.*, 2006). The advantage of satellite data compared to other methods is the large spatial coverage, but to the detriment of spatial resolution. The resolution allows to detect only the major topographic features such as the pressure ridges, whereas smaller undulations of the surface are not visible.

In this study we use only laser altimeter data and EM bird data since they provide the best compromise between area coverage and spatial resolution. From these data we can obtain information of the height and density of topographic features.

Many campaigns for measuring the atmospheric turbulent fluxes took place in different regions of the Arctic basin and Antarctic ocean since at least four decades. A summary of the results from these campaigns is given in e.g., *Overland* (1985), *Lüpkes and Birnbaum* (2005), *Andreas et al.* (2010), *Lüpkes et al.* (2012), and most recently by *Andreas et al.* (2012). Many of the available data sets were obtained in the Marginal Sea Ice Zone (MIZ) by both aircraft and shipborne observations. In particular, we cite here the aircraft flux measurements during the Arctic Ice Dynamics Joint Experiment (AIDJEX) in the seventies (*Untersteiner*, 1980) and the Marginal Ice Zone Experiment (MIZEX) in 1983 (*Fairall and Markson*, 1987; *Guest and Davidson*, 1987) and 1984 (*Anderson*, 1987) with measurements over the Fram Strait MIZ. While most of the MIZEX observations were obtained from masts installed on ships, a later campaign (REFLEX, Radiation and Eddy Flux Experiment) was performed by aircraft over the Fram Strait MIZ in September/October 1991 (*Hartmann et al.*, 1994) and March/April 1993 (*Kottmeier et al.*, 1994). During REFLEX, low level turbulence measurements and laser observations of the sea-ice topography were carried out simultaneously. The same strategy was applied during

the Arctic Radiation and Turbulence Interaction Study (ARTIST) in March 1998. The ARTIST data were used by *Garbrecht et al.* (2002) and *Vihma et al.* (2003) to validate parameterizations of drag coefficients. During some of these campaigns, also oceanic drag coefficients were measured, but there are only few observations of ice-ocean momentum fluxes compared to the ice-atmosphere fluxes. A detailed list of observed ice-ocean drag coefficients can be found in *Lu et al.* (2011).

Besides these measurement campaigns, there is a lack of studies performed with the aim to relate the variability of the drag coefficients to the surface topography. In recent years, many parameterizations have been developed that describe the dependence of the drag coefficients on pressure ridges (*Garbrecht et al.*, 1999, 2002; *Andreas*, 1995) on floes distribution (*Birnbaum et Lüpkes*, 2002; *Lüpkes and Birnbaum*, 2005), on melt ponds (*Lüpkes et al.*, 2012, 2013; *Andreas et al.*, 2010), and on keels distribution (*Lu et al.*, 2011) in the case of the ice-ocean drag coefficient. In order to relate surface roughness to atmospheric and oceanic fluxes, we select for our study a parameterization that depends on the height (depth) and concentration of topographic features.

1.4.2 Numerical Models

Besides observations, the main tool of our investigation is a coupled ocean-sea ice model. Since the 1970s, numerical models have been developed to study the large-scale processes of the polar regions (*Ukita and Moritz*, 1995) and particular attention has been paid to the study of Arctic pack ice. Sea-ice models based on the work from *Hibler* (1979) are used to conduct simulations of seasonal and interannual variability in the Arctic Ocean. Most of these models are then coupled with the other components of the climate system (hydrosphere, atmosphere, lithosphere) in order to allow large scale climate simulations. In particular, sea-ice models are coupled with oceanic and atmospheric models via both the thermodynamics and the dynamics, the latter coupling accounts for the momentum exchange at the interface between ice and atmosphere and between ice and ocean. The momentum equation is solved to determine the velocity field of the ice-ocean system. The momentum equation for the sea ice is:

$$m \frac{D\mathbf{u}}{Dt} = -mf\mathbf{k} \times \mathbf{u} + \boldsymbol{\tau}_a + \boldsymbol{\tau}_w - mg\nabla H + \mathbf{F}, \quad (1.1)$$

where m is the sea-ice mass, \mathbf{u} the sea-ice velocity, f the Coriolis parameter, g the gravitational acceleration, H the ocean surface topography and $\boldsymbol{\tau}_a$ and $\boldsymbol{\tau}_w$ are the surface air and water stress (see Equations 1.2 ad 1.3). Thus, the ice motion depends on the Coriolis force (first term on the right hand side), the wind and oceanic currents, the ocean surface tilt proportional to the gradient of the sea surface (∇H)

and the internal forces in the ice (\mathbf{F}).

The stress exerted by the atmosphere $\boldsymbol{\tau}_a$ and by the ocean $\boldsymbol{\tau}_w$ depends on the fluid flow velocity, on its direction, and on the surface roughness of the object. The general form of the total vertical flux of momentum in the atmosphere and in the ocean are:

$$\boldsymbol{\tau}_a = \rho_a C_a |\mathbf{U}_a - \mathbf{u}| R_a (\mathbf{U}_a - \mathbf{u}), \quad (1.2)$$

$$\boldsymbol{\tau}_w = \rho_w C_w |\mathbf{U}_w - \mathbf{u}| R_w (\mathbf{U}_w - \mathbf{u}), \quad (1.3)$$

where $\rho_{a,w}$ is the air or water density, $\mathbf{U}_{a,w}$ is the velocity of the wind or currents, \mathbf{u} is the velocity of the ice, $R_{a,w}$ are rotation matrices that act on the wind or current vector to account for unresolved Ekman layers. The two terms C_a and C_w are called atmospheric and oceanic drag coefficients respectively, and are a measure of the intensity of the air-ice and water-ice interactions.

The internal forces are described as the divergence of the stress tensor:

$$\mathbf{F} = \nabla \cdot \boldsymbol{\sigma}. \quad (1.4)$$

In order to describe the connection between the stress tensor $\boldsymbol{\sigma}$ and the strain rate tensor $\dot{\boldsymbol{\varepsilon}}$, we use a viscous-plastic rheology as suggested by *Hibler (1979)*. According to this choice, the constitutive law for the ice is assumed to be:

$$\sigma_{ij} = 2\eta \dot{\varepsilon}_{ij} + \left[(\zeta - \eta) \dot{\varepsilon}_I - \frac{P}{2} \right] \delta_{ij}. \quad (1.5)$$

The term δ_{ij} is the Kronecker delta, while ζ and η are the bulk and shear viscosities respectively; they are functions of the maximal compressive sea-ice strength P according to:

$$\zeta = \frac{P}{2\Delta} \quad (1.6)$$

$$\eta = \frac{\zeta}{e^2}, \quad (1.7)$$

where

$$\Delta = \sqrt{(\dot{\varepsilon}_{11}^2 + \dot{\varepsilon}_{22}^2) \left(1 + \frac{1}{e^2} \right) + \frac{4}{e^2} \dot{\varepsilon}_{12}^2 + 2\dot{\varepsilon}_{11}\dot{\varepsilon}_{22} \left(1 - \frac{1}{e^2} \right)} \quad (1.8)$$

and $e = 2$ is the ratio of the semi-axes of the elliptical yield curve. The sea-ice strength is:

$$P = P^* h e^{-C^*(1-A)} \quad (1.9)$$

with A the sea-ice concentration, h its effective thickness and the constants P^* and C^* are the strength parameters.

Relationships 1.5-1.9 hold under the assumptions that (1) sea ice is isotropic on the horizontal length scale of the model, (2) the effective tensile strength of the ice is small under all states of deformation, whereas the compressive strength is substantial under convergence, and (3) stresses are independent of strain magnitude (*Hibler, 1979*).

Two invariants of the stress tensor are:

$$\sigma_I = \frac{1}{2} (\sigma_{11} + \sigma_{22}), \quad (1.10)$$

$$\sigma_{II} = \sqrt{\eta^2 (\dot{\epsilon}_{11} - \dot{\epsilon}_{22})^2 + \eta^2 4\dot{\epsilon}_{12}^2}, \quad (1.11)$$

whereas two invariants of the strain rate tensor are:

$$\dot{\epsilon}_I = \dot{\epsilon}_{11} + \dot{\epsilon}_{22}, \quad (1.12)$$

$$\dot{\epsilon}_{II} = \sqrt{(\dot{\epsilon}_{11} - \dot{\epsilon}_{22})^2 + 4\dot{\epsilon}_{12}^2}. \quad (1.13)$$

For this study we use the Massachusetts Institute of Technology general circulation model (MITgcm) (*Marshall et al., 1997; MITgcm group, 2014*). The MITgcm is a numerical model developed for studying the state of the climate system in all its components. In the MITgcm, the sea-ice package is fully coupled with the ocean and both are driven by prescribed realistic atmospheric conditions. For this reason, the MITgcm represents a suitable tool for studying the interaction between atmosphere, sea ice and ocean.

The sea-ice package is based on a variant of the viscous-plastic (VP) dynamic-thermodynamic sea-ice model presented by *Zhang and Hibler (1987)*. The main aspects and many further numerical options and parameterizations are described in *Losch et al. (2010)*. In the chosen configuration, the MITgcm regional model domain encloses the northern North Atlantic, the Nordic Seas and the Arctic Ocean as shown in Figure (1.7). The southern model open boundary is located at approximately 50° N in the Atlantic. Another model open boundary is located in the North Pacific, south of the Bering Strait. The domain is discretized in 243×170 points with a resolution of $\frac{1}{4}$ of a degree which corresponds to approximately 25-28 km and it is rotated in order to have the same resolution over the entire model domain. The ocean model has 33 irregularly-spaced vertical levels, with thickness ranging from 10

m (upper layers) to 350 m (at maximum depth).

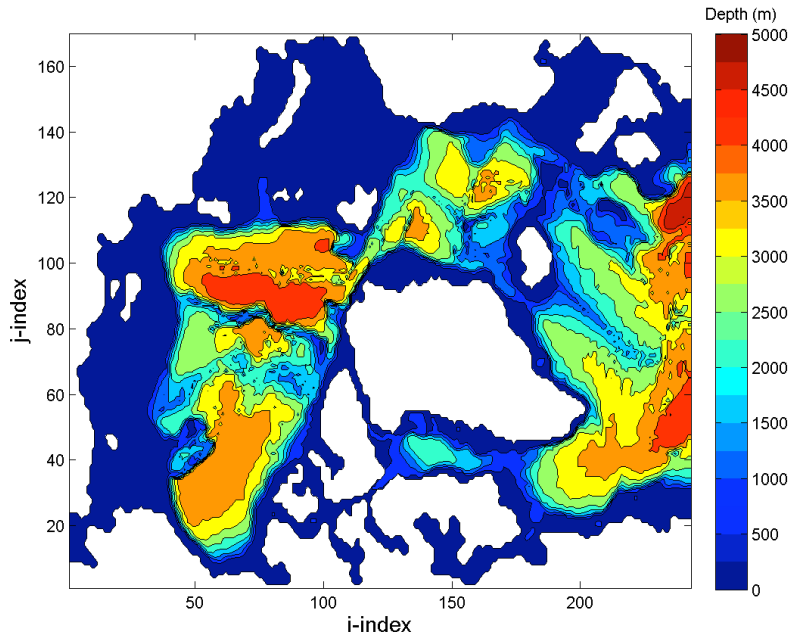


Figure 1.7: Bathymetry and domain used in the MITgcm configuration. The model domain encloses the Arctic Ocean, the Nordic Seas and the North Atlantic.

1.4.3 Representation of Sub-Grid Processes

As described in Section 1.2.1, sea ice presents many topographic features, such as pressure ridges, that affect the momentum exchange. These features have a characteristic length scale of tens of meters, while numerical models have a horizontal resolution that typically varies from 10 to 30 km and beyond. Thus, these surface properties must be parameterized. The same holds for the dependency of the drag coefficients on the sea-ice topography.

Several approaches can be found in literature for a ridging parameterization (*Schulkes*, 1995). The most widely used in numerical models consists in the introduction of a thickness redistribution function (ψ) in the evolution equation for the probability density distribution of thickness \mathcal{G} . The thickness redistribution function can assume really simple forms (*Hibler*, 1979; *Gray and Morland*, 1994) representing more a restriction on the ice concentration than a description of the ridging process, or a more complex form (*Shinohara*, 1990; *Gray and Killworth*, 1996; *Thorndike et al.*, 1975); in this latter case, the ψ function takes into account several physical processes involved in ridge formation, such as that open water can close more readily than the ice can deform, and that thin ice starts to deform before thick ice. The ψ function also describes how sea ice is redistributed between a range of thicker classes. Other

approaches, like in *Steiner et al. (1999)*, *Lensu et al. (2003)* and *Harder and Lemke (1994)*, focused on obtaining information regarding the characteristic ridge parameters: sail (keel) height and sail (keel) density. In particular, *Steiner et al. (1999)* introduced the evolution of a new variable called deformation energy (R). Newly formed ice has no stored deformation energy. During the ridging process the energy absorbed by fracture, elastic deformation and friction is stored as deformation energy. This energy is lost during melting. In this sense, the deformation energy is interpreted as “sea-ice surface roughness”. The equation for R can be implemented without affecting previously implemented physical processes in the model. From the solution for R , values for the sail density and sail height can be directly obtained (*Steiner et al., 1999*) through empirical formulae. The same holds for the atmospheric and oceanic drag coefficients.

Many current numerical models (including the MITgcm) do not parameterize the surface topography of the ice and use a constant drag coefficient for the momentum transfer without differentiating between areas where the surface roughness can not be neglected. This can lead to errors in the evaluation of the real momentum transfer.

1.5 Overview of the Scientific Papers

In the first paper:

Giulia Castellani, Christof Lüpkes, Rüdiger Gerdes, and Stefan Hendricks. 2014: **Variability of Arctic sea-ice topography and its impact on the atmospheric surface drag.** *Journal of Geophysical Research - Oceans*.

We investigate the temporal and spatial variability of sea-ice surface topography and the impact on the atmospheric drag coefficients. With this aim, we use laser altimeter measurements of sea-ice surface collected in many key regions of the Arctic Oceans over the period 1995-2011. These data are filtered in order to detect topographic features such as ridges, hummocks, and piles of ice. For these topographic features we register the height and the spacing. The analysis of the surface topography is done by means of PDFs of obstacles height and spacing averaged over 10 km flight sections. Then, the mean height of the topographic features and the mean separation between them are used to compute the drag coefficients by applying a parameterization for the surface atmospheric drag which depends on these averaged quantities. The whole topographic spectrum is further divided into small obstacles (the topographic features whose height is between 0.2 m and 0.8 m) and large obstacles (the topographic features whose height is larger than 0.8 m). This artificial division is done to assess the impact of the two different ranges on the drag coefficients. Such analysis gives an overview of the predominant sea-ice regime in each region and also on the type of obstacles that has the larger impact on the atmosphere-ice transfer

of momentum.

In the second paper:

Giulia Castellani, Rüdiger Gerdes, Martin Losch, and Christof Lüpkes. 2015: **Impact of sea-ice bottom topography on the Ekman pumping**. In: *Towards an interdisciplinary approach in Earth System Science: Advances of a Helmholtz Graduate Research School*, (Springer Earth System Science) editors: Gerrit Lohmann, Helge Meggers, Vikram Unnitan, Dieter Wolf-Gladrow, Justus Notholt, Astrid Bracher.

We investigate the variability of oceanic drag coefficients as function of sea-ice bottom topography and the impact on the Ekman vertical velocity. For this study we select one data set used already in the previous study, in particular we use data taken in 2011 in the central Arctic. We combine the surface topography data with the thickness measurements collected with the EM bird, in order to obtain the bottom profile of the ice. Also in this case, we apply a parameterization for the oceanic drag coefficients that depends on the mean depth of the keels and on the mean separation between them. These values of the drag coefficients are then used to calculate the stress applied to the ocean surface in an idealized numerical experiment. Such experiment allows the evaluation of the contribution of variable drag coefficients to the Ekman pumping.

The results obtained on the basis of observations are then validated and upscaled by using numerical models. Thus, in the third paper:

Giulia Castellani, Martin Losch, and Rüdiger Gerdes. 2014: **Sea ice drag as function of deformation and ice cover: Effects on simulated sea ice and ocean circulation in the Arctic**. *In preparation* to be submitted to Ocean Modelling.

We study the variability of atmospheric and oceanic drag coefficients in a coupled sea ice-ocean model. In particular, we implement a parameterization for drag coefficients in an Arctic Ocean regional setup of the MITgcm. According to the chosen parameterization, the drag coefficients are calculated as function of the deformation degree of the ice in each grid cell and of the ice concentration. With this study, besides upscaling the results shown in the first and second papers, we also investigate the impact of variable drag coefficients on the sea-ice drift and ocean circulation. With this aim, the variable drag coefficients are used to calculate the surface drag entering the momentum equation for the sea ice and the ocean. The analysis of the effects on the sea-ice and ocean circulation is performed by comparing two model

simulations: a control run with constant drag coefficients and a run with variable drag coefficients.

Chapter 2

Paper I: Variability of Arctic Sea Ice Topography and its Impact on the Atmospheric Surface Drag

Abstract

Over the polar oceans, near-surface atmospheric transport of momentum is strongly influenced by sea-ice surface topography. The latter is analyzed on the basis of laser altimeter data obtained during airborne campaigns between 1995 and 2011 over more than 10000 km of flight distance in different regions of the Arctic Ocean. Spectra of height and spacing between topographic features averaged over 10 km flight sections show that typical values are 0.45 m for the mean height and about 20 m for the mean spacing. Nevertheless the variability is high and the spatial variability is stronger than the temporal one. The total topography spectrum is divided into a range with small obstacles (between 0.2 m and 0.8 m height) and large obstacles (≥ 0.8 m). Results show that large pressure ridges represent the dominant topographic feature only along the coast of Greenland. In the Central Arctic the concentration of large ridges decreased over the years, accompanied by an increase of small obstacles concentration and this might be related to decreasing multi-year ice. The application of a topography dependent parameterization of neutral atmospheric drag coefficients reflects the large variability in the sea-ice topography and reveals characteristic differences between the regions. Based on the analysis of the two spectral ranges we find that the consideration of only large pressure ridges is not enough to characterize the roughness degree of an ice field, and the values of drag coefficients are in most regions strongly influenced by small obstacles.

2.1 Introduction

The topography of Arctic sea ice can be grouped into three main categories: smooth level ice, rough deformed ice, and open (or surface) water. The smooth level ice appears to be quite plane, with a thickness ranging from a few millimeters (newly refrozen leads) to several meters; the rough deformed ice is the product of mechanical processes such as rafting and ridging. In particular, ridges form in the presence of a pressure field when the ice is thick enough (*Parmeter*, 1975). In this case ice blocks pile up and form a line along the original fracture zone. Rafting occurs when a block of thin ice slides over another one; other topographic features are fractures and hummocks. Finally, open (or surface) water consists of leads and polynyas that form in the ice, and of melt ponds. The melt ponds form on the Arctic sea ice during summer owing to the accumulation of melt water formed from the melting of snow and the upper layers of ice.

The predominance of one or more of the topography types differs from year to year, from season to season, and from region to region. This has a strong link to weather and climate conditions. In warmer summers, we would expect a stronger melting of the ice and consequently a smoothing of obstacles like ridges and an increase of melt pond concentration. On the contrary, in regions exposed to many storm events, the abundance of deformed ice, in general, increases relatively to that of undeformed ice. Furthermore the topography is also related to the sea-ice type, for example the first-year ice (FYI) is expected to have fewer ridges than the second-year ice (SYI) or multi-year ice (MYI).

The ice pack in the Arctic Ocean moves as a result of the balance of forces. In particular, the main driving factors are the internal forces, the local winds and the ocean currents (*Thorndike and Colony*, 1982; *Steele et al.*, 1989, 1997). In the momentum balance equation that describes the ice motion, the intensity of air-ice and water-ice interactions depends on the drag coefficients. These must account for the impact of sea-ice surface characteristics on the near-surface transport of momentum. Thus, because of the spatial and temporal inhomogeneities of the sea-ice surface, we can expect a spatial and temporal variation of the drag coefficients as well.

In most state-of-the-art coupled atmosphere-ice-ocean numerical models, the characteristics of the sea-ice surface are, however, not described. The same holds for the dependence of the atmospheric drag coefficients on the surface topography of the ice and for the oceanic drag coefficients on the bottom topography respectively: Over closed sea ice both coefficients are usually set constant.

Nevertheless, parameterizations have been developed in recent years that describe the dependence of the drag coefficients on pressure ridges (*Garbrecht et al.*, 2002; *Andreas*, 1995) on the floe distribution (*Birnbaum et Lüpkes*, 2002; *Lüpkes and Birnbaum*, 2005), on melt ponds (*Lüpkes et al.*, 2012, 2013; *Andreas et al.*, 2010),

and on the keel distribution (*Lu et al.*, 2011) in the case of the ice-ocean drag coefficient. It was shown by *Lüpkes et al.* (2012, 2013) that the introduction of such parameterizations can explain the observed variability in measured drag coefficients.

However, atmospheric climate models are not always coupled with sophisticated sea-ice models that can simulate topographic features and account for the spatial variations of drag coefficients. Thus, it is the main goal of the present work to consider the regional variability of sea-ice topography and drag coefficients on the basis of high resolution topography data and of a parameterization of drag coefficients that was validated by aircraft measurements of turbulent fluxes.

The study presented here is based on a large and comprehensive data set of laser altimeter measurements, partially already presented in other studies. This kind of data has been largely analyzed by many authors with goals that, nevertheless, differ from the purpose of the present study. In particular, part of the data we use have been analyzed by *Von Saldern et al.* (2006) to link surface roughness characteristics of the ice with specific sea-ice regimes, including FYI and MYI. In *Rabenstein et al.* (2010) and *Haas et al.* (2008) data from 2001, 2004, and 2007 are used, together with ice thickness data, to investigate changes in the sea-ice main properties with main focus on ice thickness and ice age in the Transpolar Drift (TPD). Most of these data have been analyzed also by *Martin* (2007) to gain information on ridges with emphasis on ridge height, density, and shape. The obtained ridge parameters have been used to characterize the degree of deformation in different Arctic regions and also to validate model results (*Martin*, 2006).

The data set has been extended now by incorporating new data from summer 2011. Moreover, the novel nature of the present study consists in its main focus not only on sea-ice surface properties but on their link with atmospheric drag coefficients. The topography data obtained by laser measurements are used to investigate the regional dependence of those ice surface characteristics that are relevant for an existing parameterization of drag coefficients used in the present study. This analysis will help, furthermore, to distinguish different sea-ice regimes that are predominant in distinct regions. Thus a further novel goal of this paper is to investigate whether the large or small obstacles dominate the values of the atmospheric drag coefficients. This goal is achieved by splitting the total topography spectrum into "large topographic features" and "small topographic features" and by using the different spectral ranges to determine the drag coefficients.

The paper is structured as follows: we first present the used data sets and describe the chosen parameterization of drag coefficients (Section 2.2). In Section 2.3 we present the results and then we discuss the most relevant findings in Section 2.4.

2.2 Data and Methods

2.2.1 Methods for Estimating Sea Ice Topography and Selected Data Sets

Measurements of sea-ice topography have been performed over the last decades on different scales and with different methods. A detailed review of these methods can be found in *Martin (2007)*. Here, we present only a short summary of his description. We can distinguish three main methods. The first one consists of in-situ measurements which provide high spatial resolution, but cover only small areas. The second method consists of airborne laser measurements applied from aircraft, helicopters, ships and moorings. Finally, the satellite-based remote sensing, which has undergone many improvements in the last years, allows a much larger spatial coverage, but to the detriment of spatial resolution. Here, we use only measurements collected with a helicopter borne laser so that we obtain the best compromise between area coverage (on the order of 10^5 m) and spatial resolution (less than 1 m). The data result from several campaigns with the ice breaker *RV Polarstern*, during the *Surface Heat Budget of the Arctic Ocean* experiment (SHEBA) and during the *Greenlandic Arctic Shelf Ice and Climate* experiment (GreenICE).

Another set of laser altimeter data is the IceBridge data set available since 2009 (*Kurtz et al., 2013*). It is, however, not considered in the present work since the publically available data offer a spatial resolution that is not enough for our investigation. Nevertheless, in future work this data set could perhaps be included to obtain a once more improved coverage of the Arctic region.

In Table 2.1, all expeditions whose data are used here are listed with the year, the region, and the season during which the data have been collected, and the corresponding total length of the flights (see also Figure 2.1). Both ARKXI/1 (1995) and ARKXII (1996) took place in the Laptev and Kara seas, the latter extended also toward the North Pole near the Lomonosov Ridge (*Rachor, 1997; Augstein, 1997*). The expeditions ARKXVII/2 (2001), ARKXXII/2 (2007) and ARKXXVI/3 (2011) were carried out in the Arctic Trans-Polar Drift (TPD). ARKXVII/2 took place along the Gakkel Ridges and east of the North Pole (*Thiede, 2002*). ARKXXII/2 was carried out north of the Barents Sea and at the Pacific-Siberian side of the North Pole (*Schauer, 2008*), whereas ARKXXVI/3 was in the Kara Sea and in the region around the North Pole. The expedition ARKXIX (2003) (*Haas and Lieser, 2001*) and a part of ARKXXII/2 (2007) took place in the Fram Strait. The expedition ARKXX/2 (2004) was carried out north of the Fram Strait (*Bud us and Lemke, 2007*). The measurements within the framework of the European Union project GreenICE were carried out in 2004 and 2005 in the Lincoln Sea, north of Greenland and Ellesmere Island (*Dal  et al., 2005; Haas, 2004b; Haas et al., 2006*). The mea-

Table 2.1: List of all expeditions during which laser measurements have been carried out. For each expedition, the year, the region, the season, the prevalent sea-ice regime, and the total length of the profile used for the present work is specified. We consider the period July-September as summer and the period April-May as winter. (We refer to summer as the period ranging from July to late September. Winter period is defined here as the period from December to late May.)

Expedition	year	Region	Season	Length [km]	prevalent sea-ice regime
ARKXI/1	1995	Laptev/Kara Sea	July-Sept	680	FY ^a
ARKXII	1996	Laptev/Kara Sea	July-Sept	1730	FY ^a
		Central Arctic			MY ^a
SHEBA	1998	Beaufort Sea	Aug-Sept	300	MYI ^b
ARKXVII/2	2001	TPD	Aug-Sept	250	MY ^c
ARKXIX/1	2003	Fram Strait	April	710	FY ^d
ARKXX/2	2004	Fram Strait	July-Aug	790	MY ^e
GreenIce	2004	Lincoln Sea	May	710	MY ^e
GreenIce	2005	Lincoln Sea	May	490	MY ^f
ARKXXII/2	2007	TPD/Fram Strait	Aug-Sept	3390	FY ^g
ARKXXVI/3	2011	TPD	Aug-Sept	1570	FY ^h

a) Haas and Eicken (2001), b) <http://www.eol.ucar.edu/projects/sheba/>, c) Haas and Lieser (2001), d) Von Saldern et al. (2006), e) Lieser (2005), f) Haas et al. (2006), g) Schauer (2008), h) personal communication (Stefan Hendricks)

surements performed during the SHEBA campaign were carried out in 1998 in the Beaufort Sea region [<http://www.arm.gov/campaigns/nsa1997sheba>].

Most of the expeditions were undertaken in the period July-September, so during or directly after the melt season, except for ARKXIX/1 and GreenICE which represent winter conditions. Winter is defined here as the period between December and the beginning of ice melt which occurs in most Arctic regions not before May.

2.2.2 Processing of Laser Profiles

The measurement campaigns prior to 2001 were conducted with a downward-looking laser altimeter *IBEO PS100E* with a wave length of 905 nm, a sampling frequency of 2 kHz and an accuracy of ± 3 cm. With a typical helicopter speed of 30-40 m s⁻¹, the effective measurement points spacing is about 1.5-2 cm, that was later resampled to 15-20 cm in order to have a spatial resolution closer to the one obtained with the instrument introduced in 2001. The Riegl Laser LD90-3100HS introduced in 2001 has a wavelength of 905 nm, a sampling frequency of 100 Hz and an accuracy of ± 1.5 cm. The point spacing is about 30-40 cm.

The profiles recorded by the laser altimeter show an altitude variation due to the surface roughness of the ice and, at a lower frequency, altitude changes of the helicopter. In order to remove this unwanted signal component, and because high precision GPS information was not available for all the data sets, a combination of low and high pass filters is used (Hibler, 1972). The result obtained is not the actual

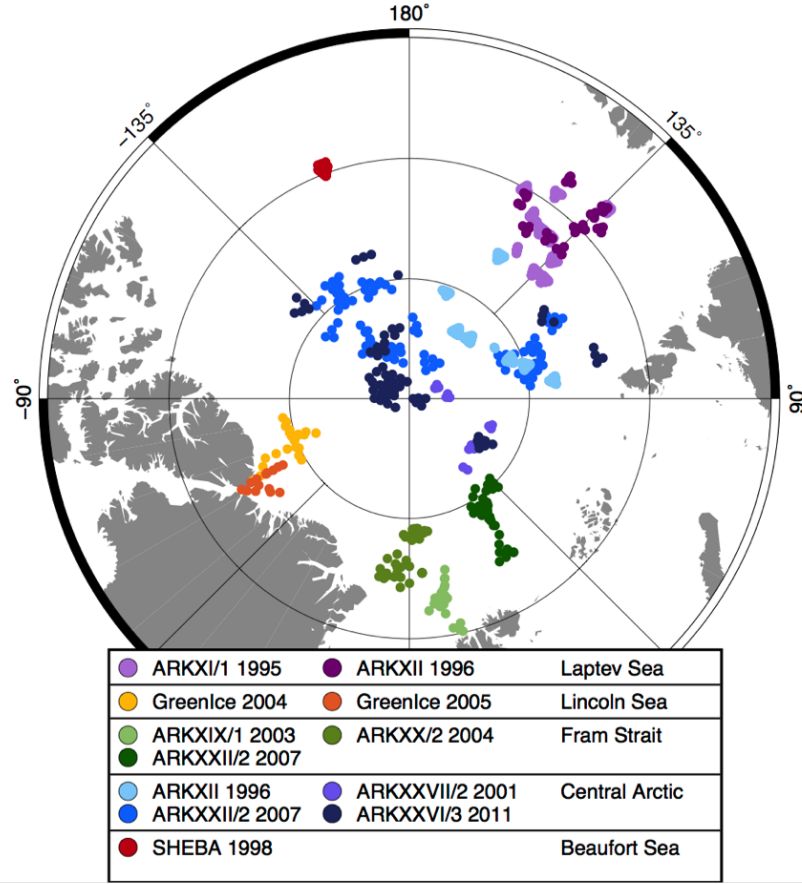


Figure 2.1: Map of the Arctic Ocean with the location of the laser altimeter measurements divided into five regions: Laptev Sea (shades of violet), Lincoln Sea (shades of Orange), Central Arctic (shades of blue), Fram Strait (shades of green) and Beaufort Sea (red). Note that this map is very similar to Figure 4.1 in *Martin* (2007). The differences are that here we include data from 2007 (Central Arctic and Fram Strait) and 2011 (Central Arctic), whereas we omit data in the Kara Sea and Barents Sea.

freeboard of the ice but the surface topography elevation with respect to level ice. A routine is then applied to the filtered profiles to select maxima that are higher than a certain threshold value. Following former works involving laser altimeter data by e.g., *Garbrecht et al.* (2002); *Ropers* (2013), we use in this study a cut-off height of 0.2 m in order to detect all topographic features such as pressure ridges, rubble fields and hummocks. A value smaller than 0.2 m, as used by e.g., *Mai et al.* (1996); *Hartmann et al.* (1994), which would have allowed to identify further topographical features, such as the edges of melt ponds, was not used due to uncertainties in the determination of errors in the filtering procedure. Later, a threshold of 0.8 m is used, as in *Rabenstein et al.* (2010); *Martin* (2007), to select only large pressure ridges. Moreover, two adjacent topographical elements have to fulfill the Rayleigh criterion: two maxima points must be separated by a point whose height is smaller than half of

the value of the maxima in order to be resolved as separate elements (*Hibler, 1975; Wadhams and Horne, 1980; Wadhams and Davy, 1986*).

In former works (see e.g., *Rabenstein et al. (2010)*), the dropouts in the laser signal are used to estimate the fraction of open water along the transects. Nevertheless, reflections of the laser signal can be missed by the instrument due to small pitch and roll movements, thus the accuracy of the absolute melt pond and water concentration is very uncertain. Moreover, in August and September (when most of the expeditions were carried out), the melt ponds were already refrozen. For these reasons, we do not detect melt ponds from the laser data.

The analysis of the topography presented here differs from previous work (see, e.g., *Rabenstein et al. (2010); Martin (2007)*) by concentrating on the ensemble of 10 km profiles. This choice is motivated by the following reasons (see also Section 2.2.3): parameterizations of drag coefficients need, as input, topography related parameters that are averaged over the grid cell. 10 km is the grid length of a high resolution regional climate model. Furthermore, the value 10 km is proposed by *Lüpkes et al. (2012)* as a reasonable minimum grid size for the kind of parameterizations used here. The choice of 10 km is furthermore, most convenient for the analysis of the laser data which were obtained from flight sections mostly between 10 and 40 km length.

For each profile, the topographic features are detected with the method described above. The height of each obstacle and the spacing between two adjacent obstacles are recorded. Then, the height and the spacing averaged over 10 km sections are calculated for each profile. The analysis of sea-ice topography presented here is based on these mean quantities. Such a choice might level out the variability that can be found in profiles of such length, but as shown by *Vihma et al. (2003)* the modelled fluxes of momentum based on 10 km averages of topography parameters reproduce well the observed fluxes. Moreover, the validity of the typical exponential fit for individual heights distribution (*Rabenstein et al., 2010*) and of the lognormal fit for individual spacings distribution (*Wadhams and Davy, 1986*) is independent from the mean. The mean values presented in this study are related to the value of the fitting parameters of the exponential and log-normal distributions (for details see *Martin (2007)* and *Rabenstein et al. (2010)*, their Table 2 and 3).

2.2.3 Parameterization of Drag Coefficients

Atmospheric neutral drag coefficients over sea ice covered regions show a variability over roughly half an order of magnitude. This finding is based on the analyses of data collected during many campaigns in different regions of the Arctic basin and Antarctic oceans since at least four decades. A summary of the results from these campaigns is given in e.g., *Overland (1985), Lüpkes and Birnbaum (2005), Andreas*

et al. (2010), *Lüpkes et al.* (2012), and most recently by *Andreas et al.* (2012). Many of the available data sets were obtained in the marginal sea ice zones by both aircraft and shipborne observations. In particular, turbulence measurements were collected during the Arctic Ice Dynamics Joint Experiment (AIDJEX) in the seventies (*Untersteiner*, 1980), during the Marginal Ice Zone Experiment (MIZEX) in 1983 (*Fairall and Markson*, 1987; *Guest and Davidson*, 1987) and 1984 (*Anderson*, 1987), during the Radiation and Eddy Flux Experiment (REFLEX) in 1991 (*Hartmann et al.*, 1994) and 1993 (*Kottmeier et al.*, 1994), and during the Arctic Radiation and Turbulence Interaction Study (ARTIST) in 1998 (*Garbrecht et al.*, 2002; *Vihma et al.*, 2003). Finally, the most comprehensive data set with drag coefficients for the inner Arctic was obtained during the SHEBA campaign in 1998.

The sea ice data described in Section 2.2.1 do not contain turbulent fluxes. Thus the basic idea of the present investigation is to use one of the available parameterizations relating the measured sea-ice topography to 10 m neutral drag coefficients. Possible parameterizations are those from *Lüpkes et al.* (2012, 2013) or similar ones discussed therein (see also *Tsamados et al.* (2014)) and from *Garbrecht et al.* (2002). Here, we use the latter parameterization, which is explained in more detail in the following including its differences to the *Lüpkes et al.* (2012, 2013) scheme.

The *Garbrecht et al.* (2002) parameterization is based on a partitioning concept introduced for sea ice already by *Arya* (1973) and *Arya* (1975). This concept distinguishes between the influence of small-scale roughness (skin drag) and larger distinct obstacles (form drag). Thus the neutral drag coefficients are given by

$$C_{dn10} = C_{dn10,i} + C_{d10,f} \quad (2.1)$$

where $C_{dn10,i}$ and $C_{d10,f}$ are the skin drag and form drag coefficients related to 10 m height. $C_{d10,f}$ is parameterized as a function of the mean ridge height H_e and mean spacing x_e between them. A constant value for the skin drag coefficient ($C_{dn10,i} = 8.38 \cdot 10^{-4}$) is chosen which was determined from flights over very smooth ice by *Garbrecht et al.* (2002). The form drag coefficient for neutral conditions is given by their Equation 8 (also similar in *Hanssen-Bauer and Gjessing* (1988))

$$C_{d10,f} = \frac{c_w}{\pi x_e} \left(\frac{1}{\ln(10/z_0)} \right)^2 \int_{z_0}^{H_e} \left[\ln \left(\frac{z}{z_0} \right) \right]^2 dz, \quad (2.2)$$

that, once integrated, leads to:

$$C_{d10,f} = \frac{c_w}{\pi} \frac{H_e}{x_e} \frac{\left[\ln \left(\frac{H_e}{z_0} \right) - 1 \right]^2 + 1 - 2 \frac{z_0}{H_e}}{\left[\ln \left(\frac{10}{z_0} \right) \right]^2}. \quad (2.3)$$

z_0 is the surface roughness length over smooth ice and is connected with $C_{dn10,i}$ according to

$$z_0 = 10 \exp\left(-\frac{\kappa}{\sqrt{C_{dn10,i}}}\right). \quad (2.4)$$

$\kappa = 0.4$ is the v. Karman constant so that $z_0 \approx 1 \cdot 10^{-5}$ m. π occurs in the form drag coefficient since the orientation of ridges to the mean wind is assumed to be randomly distributed. H_e and x_e are calculated for each 10 km profile as explained in Section 2.2.2. Note that the value of z_0 is relatively small and we can neglect the term z_0/H_e .

c_w is the coefficient of resistance of a single ridge and must be prescribed. Different approaches are possible, *Garbrecht et al.* (2002) have shown, however, that the best agreement with observed drag coefficients resulted for

$$c_w = 0.185 + 0.147 H_e, \quad (2.5)$$

which is a modification of the *Banke and Smith* (1975) formulation. The parameterization was tested and well validated over closed sea ice with data from ship and aircraft so that, in lack of direct measurements, it can be a reliable substitute.

Note that Equation 2.3 is similar to the parameterization by *Lüpkes et al.* (2012) for drag coefficients in the marginal sea-ice zone (see their Equations 19 and 22) and inner Arctic with melt ponds and leads in the limit of sea-ice concentration going to 1. However, there are several differences between Equation 2.3 and the *Lüpkes et al.* (2012) parameterization. The first and main difference is that the *Lüpkes et al.* (2012) parameterization was developed especially to account for the 3D effect of ice floe and melt pond edges. Equation 2.3 considers obstacles only in 2D (elevation line e.g., along a flight track). Another difference is the neglect, in Equation 2.3, of a function that accounts for the sheltering of wind between ridges. We have tested the latter assumption by multiplying Equation 2.3 with S_c^2 where

$$S_c = 1 - \exp(-sx_e/H_e) \quad (2.6)$$

is the sheltering function proposed in *Hanssen-Bauer and Gjessing* (1988) with $s = 0.5$ as in *Lüpkes et al.* (2012). However, even for large ridge concentration as in the Lincoln Sea (see Section 2.3.1) the sheltering effect leads to a modification of the drag coefficients that is smaller than 0.05 % so that we finally neglect it.

The last difference is the ridge height dependence of c_w (Equation 4.9). In *Lüpkes et al.* (2012) a constant value of c_w can be used since the range of obstacle heights related to ponds and floe edge is much smaller than in the present case.

The *Garbrecht et al.* (2002) parameterization was developed to account for obstacles

on a closed ice surface without open water. However, the flights during summer considered in the present study, were carried out also over melt ponds. We have to consider that a parameterization like that of *Lüpkes et al.* (2012), which was especially constructed for a roughness dominated by melt pond and lead edges, may be superior in situations with large pond coverage. However, the ice surface considered in *Garbrecht et al.* (2002) was also characterized by a large variability in obstacle types (both extended and fractured ridges as well as sastrugi-like structures). Moreover, as already explained in Section 2.2.2, it was not possible to clearly distinguish ponds from sea ice on the basis of the used laser measurements. For these reasons we decided to use the above parameterization (Equations 2.3 - 4.9) that can be applied to the available data after x_e and H_e are determined. As it will be shown in Section 2.3.2, the calculated drag coefficients agree well with the range of drag coefficients determined from turbulence measurements.

2.3 Results

We split the total Arctic into five regions: Central Arctic, Fram Strait, Lincoln Sea, Laptev Sea, and Beaufort Sea. In Figure 2.1, the tracks of the laser measurements are shown for each region. In particular, for the Central Arctic, we can use data from summers 1996 (July-September), 2001 (August-September), 2007 (August-September), and 2011 (August-September), but the number of available data in 2001 is much smaller than in the other years. In the Fram Strait region, data were collected in 2003 (April), and 2004 and 2007 (August). For the Lincoln Sea, data result from the GreenICE project of two consecutive years: May 2004 and May 2005. For the Laptev Sea, we use data from 1995 and 1996 in the period August-September. Finally, for the Beaufort Sea, only one set of topographic data collected during the SHEBA campaign in summer 1998 (August-September) is available and the amount of data is smaller than for the other regions.

We present first the results regarding the variability of the sea-ice surface topography (Section 2.3.1). Then we show the calculated atmospheric drag coefficients (Section 2.3.2).

2.3.1 Surface Topography

Results for sea-ice topography are presented as PDFs of mean heights and mean separations between obstacles (large pressure ridges as well as bumps, piles, and rubbles) where the means are calculated over the 10 km sections (see Section 2.2.2). Equation 2.3 shows that actually the drag coefficients depend on the aspect ratios H_e/x_e so that we could consider alternatively only these ratios. However, we decide to show spectra of both H_e and x_e since both values being looked at separately yield

a clearer picture of the surface structure.

From Figures 2.2a and 2.3a we see that the typical values averaged over 10 km profiles are 0.45 m for the mean height and about 20 m for the mean spacing between obstacles.

Regarding the mean heights of all measurements together, Figure 2.2a shows also a secondary mode around 0.7 m due to the 2004 data over the Fram Strait seen in Figure 2.2c and to the Lincoln Sea data shown in Figure 2.2d. The right tail of the distribution (2.2a) goes only slowly to zero due to data in the Lincoln Sea (Figure 2.2d).

Considering Figures 2.2b-2.2f, it is obvious that there is a large variability between the different regions. H_e -spectra of the Central Arctic, Laptev Sea, and Beaufort Sea are relatively similar, while especially the Fram Strait PDF for 2004 and Lincoln Sea PDFs differ strongly from the other ones since in both regions the peak of H_e occur at larger values and the width of the spectra is larger than in all other regions. Regarding individual regions, we mention the following points: In the Central Arctic, we have data from four years which might allow to consider a temporal development, but the H_e -spectra do not show a clear trend.

In the Lincoln Sea (Figure 2.2d), the shape of the H_e -distributions for both years, 2004 and 2005, is very similar with maxima between 0.6 m and 0.7 m. This shows that the sea ice in the Lincoln Sea is characterized by, on average, higher obstacles, as well known from other studies (*Martin, 2007*).

In the Laptev Sea (Figure 2.2e), the PDFs of H_e show that there has been an increase in the maximum values of mean heights from 0.3 m in 1995 to 0.45 m in 1996. The 1996 spectrum looks similar to that for the Central Arctic from 1996 and the peak from 1995 is closer to the peak in the Beaufort Sea.

In Figure 2.3, we show the spectra for the mean spacings x_e between obstacles which give also information on the concentration. When we consider data of all regions together in one spectrum (Figure 2.3a), we see that x_e is varying between few meters and 100 m with a maximum of occurrence around 20 m. Figures 2.3b-2.3f show a large temporal and spatial variability, which is more clearly pronounced than for the H_e -spectra.

In the Central Arctic, the mean spacing (2.3b) shows a large variability between individual years that concerns especially the large difference between 1996 (maximum at ca 40 m) and the other years (maximum at about 17-20 m).

A large variability can be seen also in the Fram Strait spectra of x_e (Figure 2.3c): There is a higher obstacle concentration in 2004 and a smaller one in 2003 and particularly in 2007. The 2004 campaign was closer to Greenland, which would explain the similarity to the Lincoln Sea spectra. We thus observe a high spatial, rather than temporal, variability.

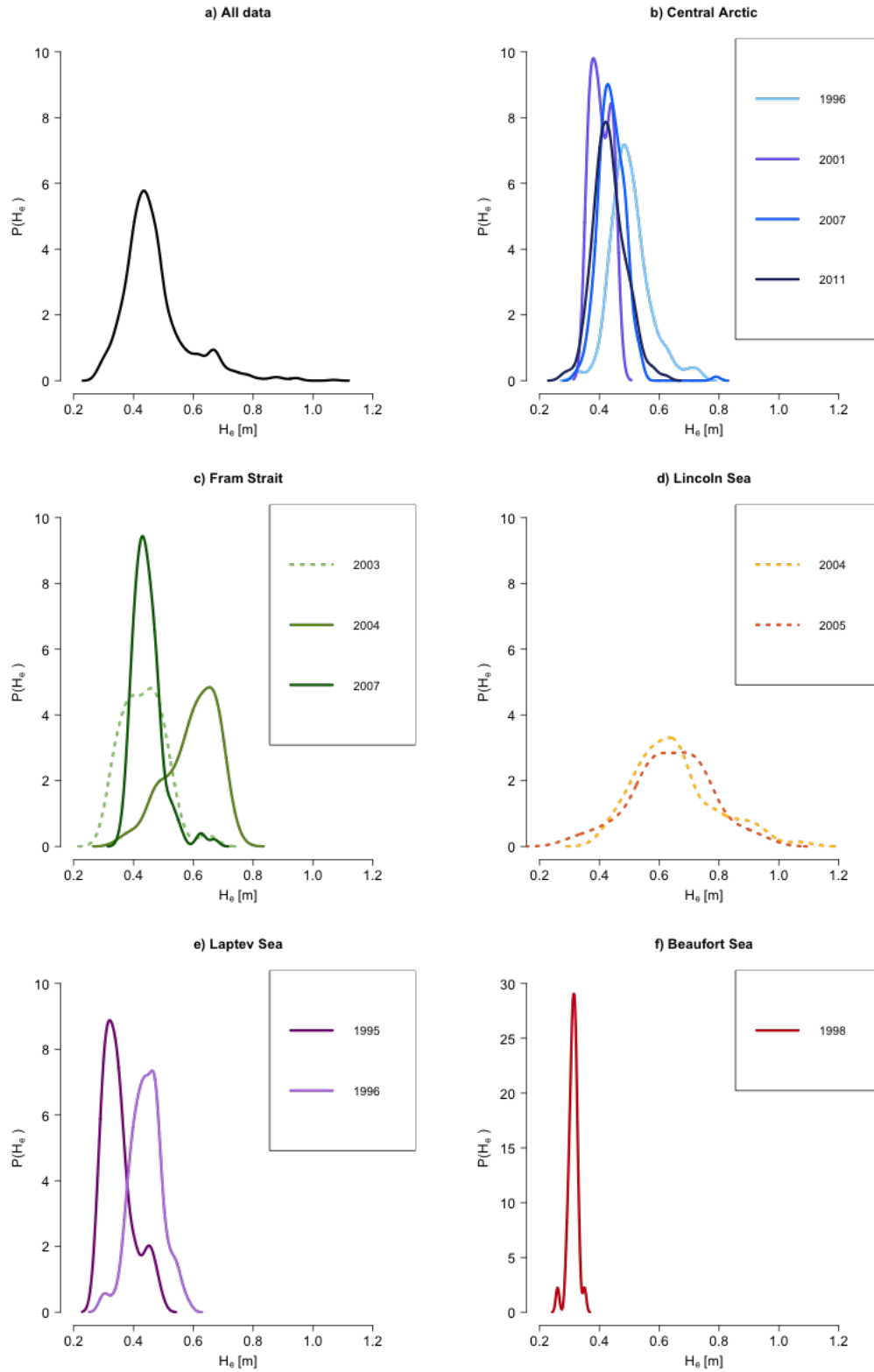


Figure 2.2: PDFs for mean heights of obstacles for all data sets (a) and for each region separately (b-f). We use a full line for the data taken in summer (July-September) and the dotted lines for data taken during winter (December-May)

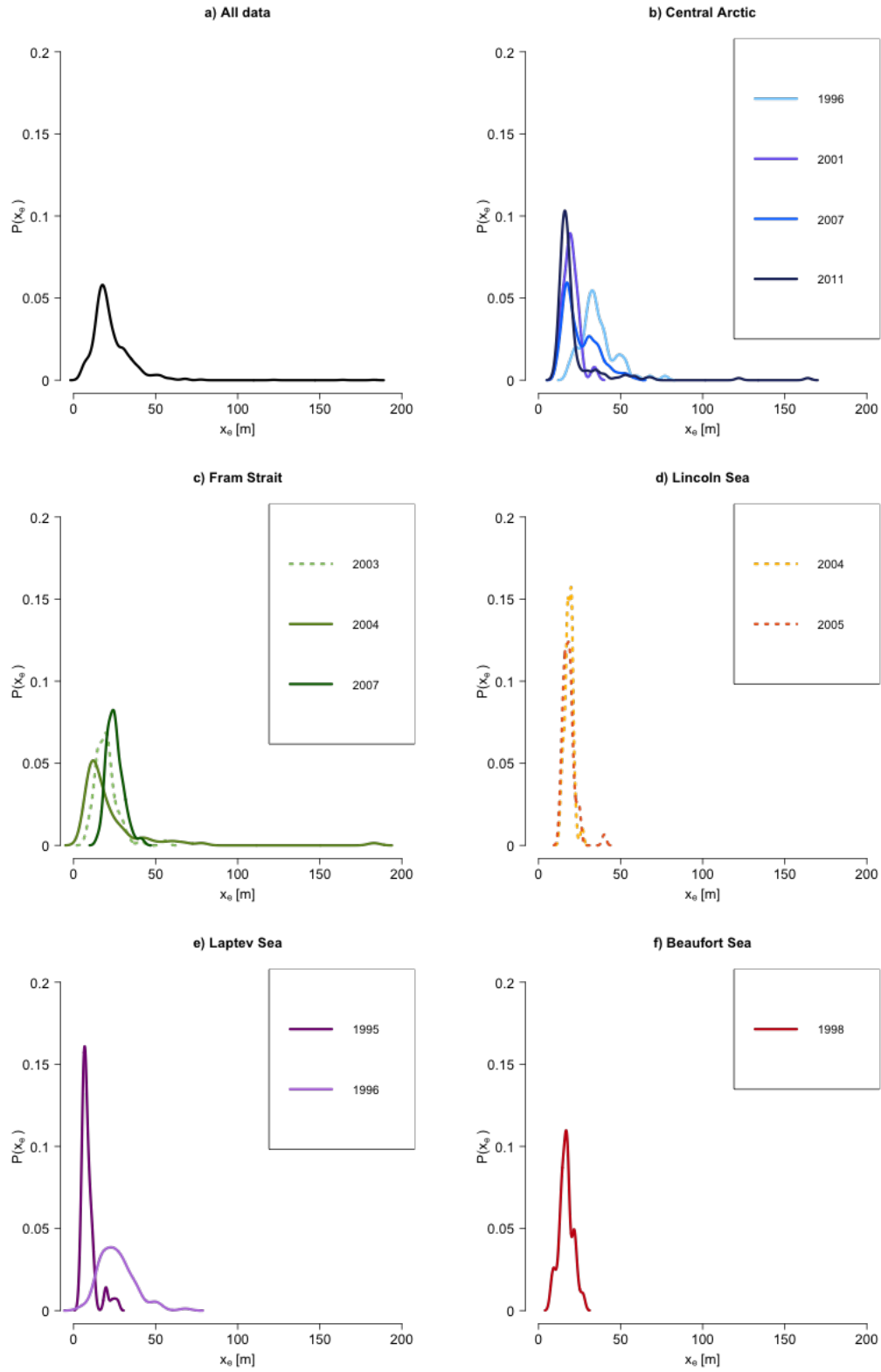


Figure 2.3: PDFs for mean spacings between obstacles for all data sets (a) and for each region separately (b-f). We use a full line for the data taken in summer (July-September) and the dotted lines for data taken during winter (December-May)

Table 2.2: Total mean drag coefficients and standard deviations computed for each region and each year in the three different ranges: only Large obstacles considered (LR range), only Small obstacles considered (SR range) and All topographical Features considered (AF range). Columns 5 and 6 show the maximum and minimum values for the considered region and year for AF. All the presented values of drag coefficients are multiplied by 10^3 .

Region	year	n° of profiles	C_{dn10} (AF)	max	min	C_{dn10} (LR)	C_{dn10} (SR)
Laptev Sea	1995	68	2.43 ± 0.44	3.35	1.19	1.52 ± 0.38	2.09 ± 0.36
	1996	96	1.60 ± 0.29	2.85	1.12	1.39 ± 0.22	1.31 ± 0.23
Central Arctic	1996	77	1.47 ± 0.19	2.01	1.10	1.38 ± 0.22	1.15 ± 0.09
	2001	25	1.66 ± 0.14	1.92	1.35	1.34 ± 0.11	1.38 ± 0.16
	2007	245	1.64 ± 0.35	2.75	1.06	1.20 ± 0.18	1.40 ± 0.23
	2011	157	1.84 ± 0.4	2.80	0.95	1.24 ± 0.26	1.56 ± 0.24
Lincoln Sea	2004	71	2.59 ± 0.57	4.29	1.64	3.00 ± 0.92	1.35 ± 0.08
	2005	49	2.59 ± 0.58	3.68	1.16	2.89 ± 0.89	1.39 ± 0.1
Beaufort Sea	1998	30	1.65 ± 0.18	2.17	1.42	1.16 ± 0.09	1.48 ± 0.16
Fram Strait	2003	71	1.79 ± 0.34	2.70	1.21	1.66 ± 0.5	1.39 ± 0.18
	2004	79	2.65 ± 0.82	4.66	0.88	1.58 ± 0.31	1.96 ± 0.6
	2007	125	1.59 ± 0.26	3.02	1.17	1.22 ± 0.17	1.34 ± 0.18

In the Laptev Sea, we see a smaller separation between the obstacles (2.3e) in 1995 and thus a higher concentration, while in 1996 we have fewer but higher obstacles. Moreover, the shape of the distribution for the mean separation (2.3e) varies strongly between 1995 and 1996, showing that the distribution and concentration of obstacles in 1996 were less uniform than in the previous year.

2.3.2 Drag Coefficients

In the following we analyze not only the full spectral range as shown in Figures 2.2 and 2.3 but also subsets considering small and large obstacles separately.

Results for the Entire Topography Spectrum

In Table 2.2, we list the drag coefficients calculated with Equations 2.1 and 2.3 as averages over each campaign in different regions and years together with the maximum and minimum values.

We see from Table 2.2 that these mean values of drag coefficients range from $1.47 \cdot 10^{-3}$ (Central Arctic) to $2.65 \cdot 10^{-3}$ (Fram Strait). Thus they are in a reasonable range that is known from turbulence measurements in different polar regions over sea ice which are mentioned in Section 2.2 (see, e.g., publications mentioned in *Andreas et al.* (2010), *Lüpkes et al.* (2012) and *Overland* (1985), their Table 3). The maximum values are found in the Lincoln Sea in 2004 ($4.29 \cdot 10^{-3}$) and in the Fram Strait in the same year ($4.66 \cdot 10^{-3}$) while the minimum values are found in the Central Arctic in 2011 ($0.95 \cdot 10^{-3}$) and in the Fram Strait in 2004 ($0.88 \cdot 10^{-3}$). Minimum values in other regions are close to these ones, while for the maxima we see more variability. In Figure 2.4, we show the PDFs for the calculated drag coefficients. The PDF for

all data (2.4a) shows a peak around $1.5 \cdot 10^{-3}$. This agrees well with the value of $1.4 \cdot 10^{-3}$ that is proposed by *Andreas et al.* (2010) as skin drag coefficient for sea ice based on SHEBA turbulence measurements, which includes the average effect of obstacles. A secondary mode is present at around $2.5 \cdot 10^{-3}$.

Looking at all regions, we notice the great variability of drag coefficients as can be expected from the variability in the topography (Section 2.3.1). This variability concerns the shape of the spectra as well as absolute values, maxima, and minima. In few spectra, the peak of the PDFs occurs at a value higher than the main peak for the PDF of all data. These spectra are those for Lincoln Sea (2004 and 2005), Fram Strait in 2004, and Laptev Sea in 1995. In particular, for Lincoln Sea (both years) and for the Fram Strait (2004) also the shape of the distribution differs strongly from others with a longer tail towards higher values of the drag coefficients. This is consistent with PDFs for mean heights (Figure 2.2c-2.2d) showing higher values, and with the small values in the PDFs for mean spacings (Figures 2.3c-2.3d). In the Laptev Sea, high values in 1995 seem to be caused by the very small spacing between obstacles (2.3e).

Results for Spectral Subranges

We introduce in this section another higher threshold for the topography data namely a value of 0.8 m instead of the 0.2 m used before. Those obstacles that are higher than 0.8 m will be called pressure ridge (LR range) and those whose height is in between 0.2 m and 0.8 m will be called small obstacles (SR range) in the following. The choice of 0.8 m as a threshold value for ridges was already used in *Martin* (2007) and *Rabenstein et al.* (2010). We use the same procedure for detecting obstacles that was explained in Section 2.2.2, but now limited to the spectral subranges SR and LR. Thus, for each 10 km profile we obtain mean values of H_e and x_e for the LR and SR ranges. These values are used to calculate once more the drag coefficients.

We stress that the drag coefficients referring only to SR and LR are artificial ones which would not occur in nature. Furthermore, it is important to understand that the sum of drag coefficients related to the SR range and LR range is not necessarily equal to the results for the entire range (called AF in the following). The reason is that drag coefficients depend on mean quantities which cannot be simply added. Furthermore, the dependence on H_e is not linear in Equation 2.3. Another point that needs clarification is the question if the entire topography spectra would support such a splitting into different spectral ranges, e.g., by a bimodal structure. However, this is not the case (not in Figure 2 and also not in spectra of other authors (*Rabenstein et al.*, 2010)). Nevertheless, for the present goal, namely to clarify the range of main impact on drag coefficients, our splitting is justified since the structures of the H_e or x_e spectra do not necessarily determine the range of impact on the drag coefficients.

So, it might happen that only the large ridges and their spectra determine surface drag.

We consider the results for different spectral ranges for three different regions only, namely for the Lincoln Sea, Central Arctic, and Laptev Sea. Figures 2.5 - 2.7 show the PDFs of the mean height and mean spacing related to the LR and SR ranges for these regions. In Figures 2.8 - 2.9 we show PDFs of drag coefficients calculated for the two ranges, LR and SR, in the different regions.

Figures 2.5a and 2.5c show that in the Lincoln Sea region typical pressure ridges have a height of 1.5-1.6 m and a separation of 50 m. The small topographic features (2.5b and 2.5d), instead, have a typical height of 0.35 m and separation of 30-40 m. It is remarkable that the LR range related drag coefficients (Figure 2.8) do not differ much from those for the AF range. They are even larger than for the AF range. This can be explained by the dependence on the aspect ratio H_e/x_e (see Equation 2.3) that is obviously decreasing for the AF range as compared to the LR range. This means that in regions as Lincoln Sea which are characterized by a high degree of deformation, the drag coefficients are dominated by large obstacles, such as pressure ridges.

The described behavior points probably also to a general weakness of this type of parameterization which is using only statistical moments (like the mean values) rather than the entire topography spectrum. Obviously, an addition of roughness elements must not necessarily result in an increase of drag coefficients.

Further insight is possible by considering the Laptev Sea (Figures 2.6 and 2.9). The pressure ridges have a typical height around 1.1 m which is a lower value than in the Lincoln Sea region. The typical spacing is around 150-200 m, three times larger than in the Lincoln Sea. What is interesting, is that the two years show PDFs for the mean obstacle heights and distances which are very similar in the LR range, while they differ a lot in the SR range. For the latter, we see a shift in the peaks for the mean heights and distances towards larger values in 1996 compared with 1995. Thus, the differences already seen for the whole topography spectrum (Figures 2.2e-2.3e) are due to the small topographic features and not caused by changes of the pressure ridge height and/or concentration. This is an important result, since it shows that the consideration of only large pressure ridges is not enough to characterize the roughness degree of an ice field. Moreover, it appears from Figure 2.9 that this behavior is reflected in the drag coefficients. We also see that the contribution of the LR range to the drag coefficients is very low in 1995 compared to 1996.

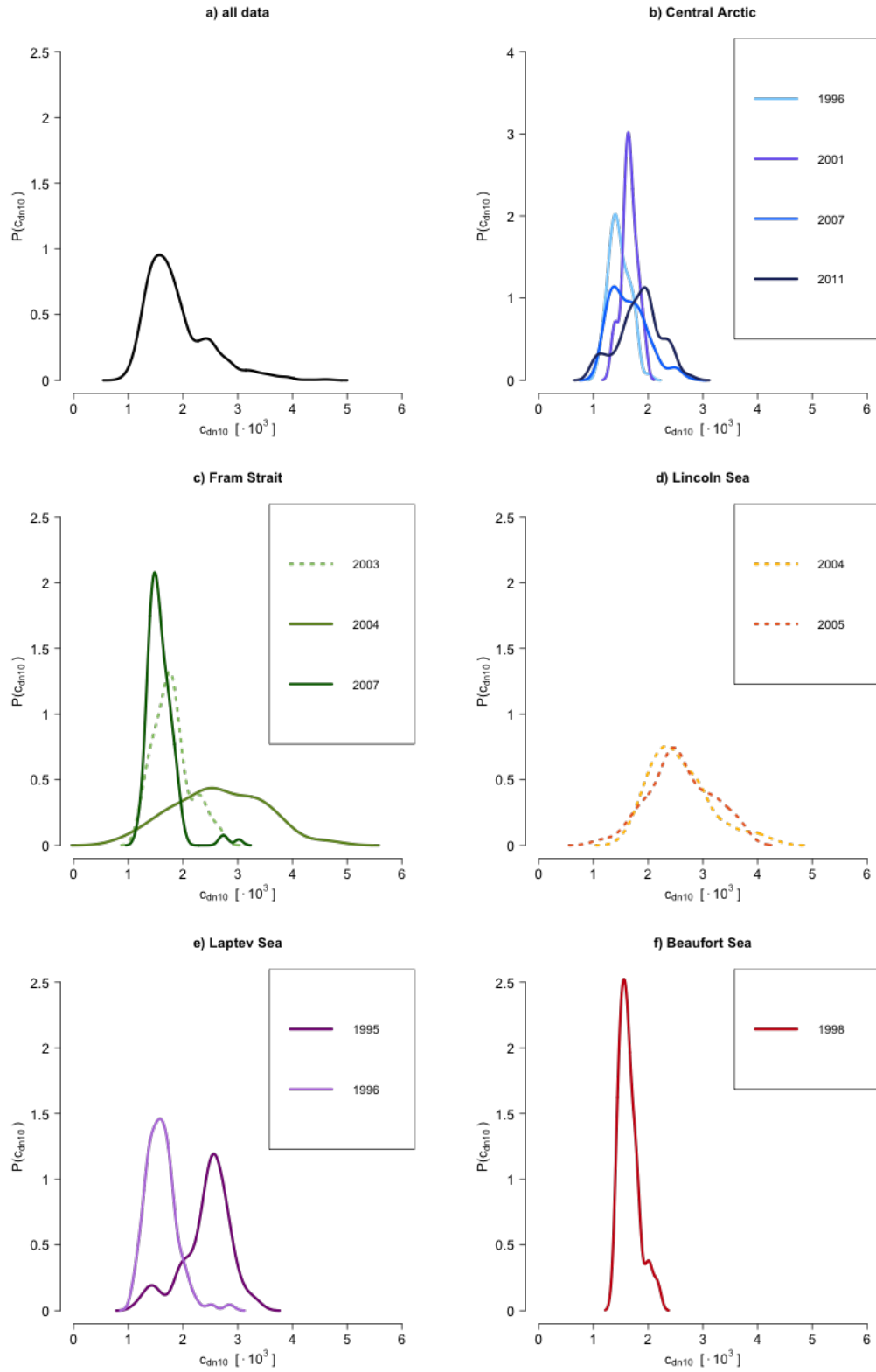


Figure 2.4: PDFs for calculated drag coefficients for all data sets (a) and for each region separately (b-f). We use a full line for the data taken in summer (July-September) and the dotted lines for data taken during winter (December-May)

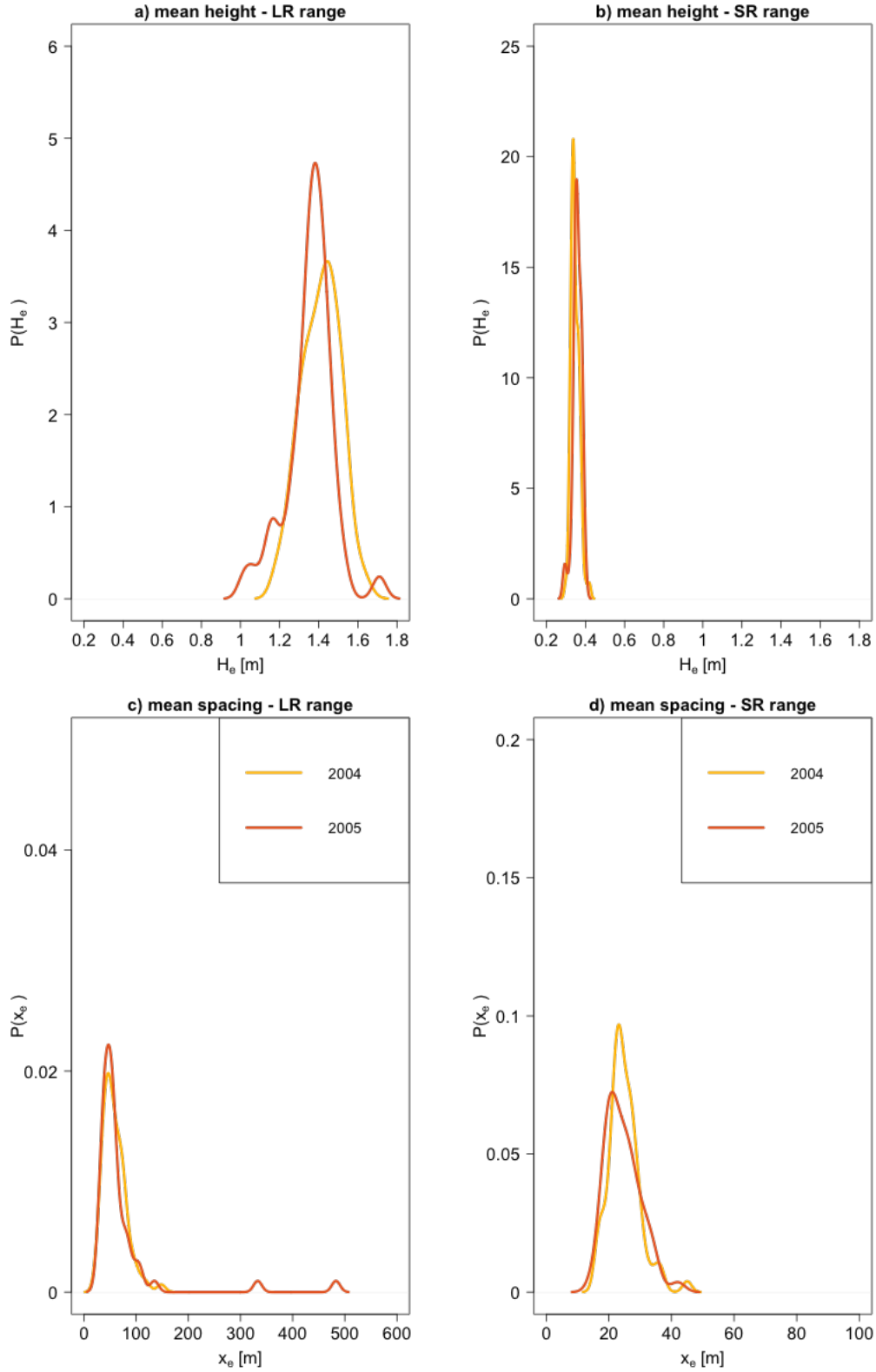


Figure 2.5: PDFs for mean heights of topographic features (a-b) and for mean spacings between topographic features (c-d) in the Lincoln Sea. The case of large ridges (LR) is shown in a) and c), while the case of small obstacles (SR) is shown in b) and d).

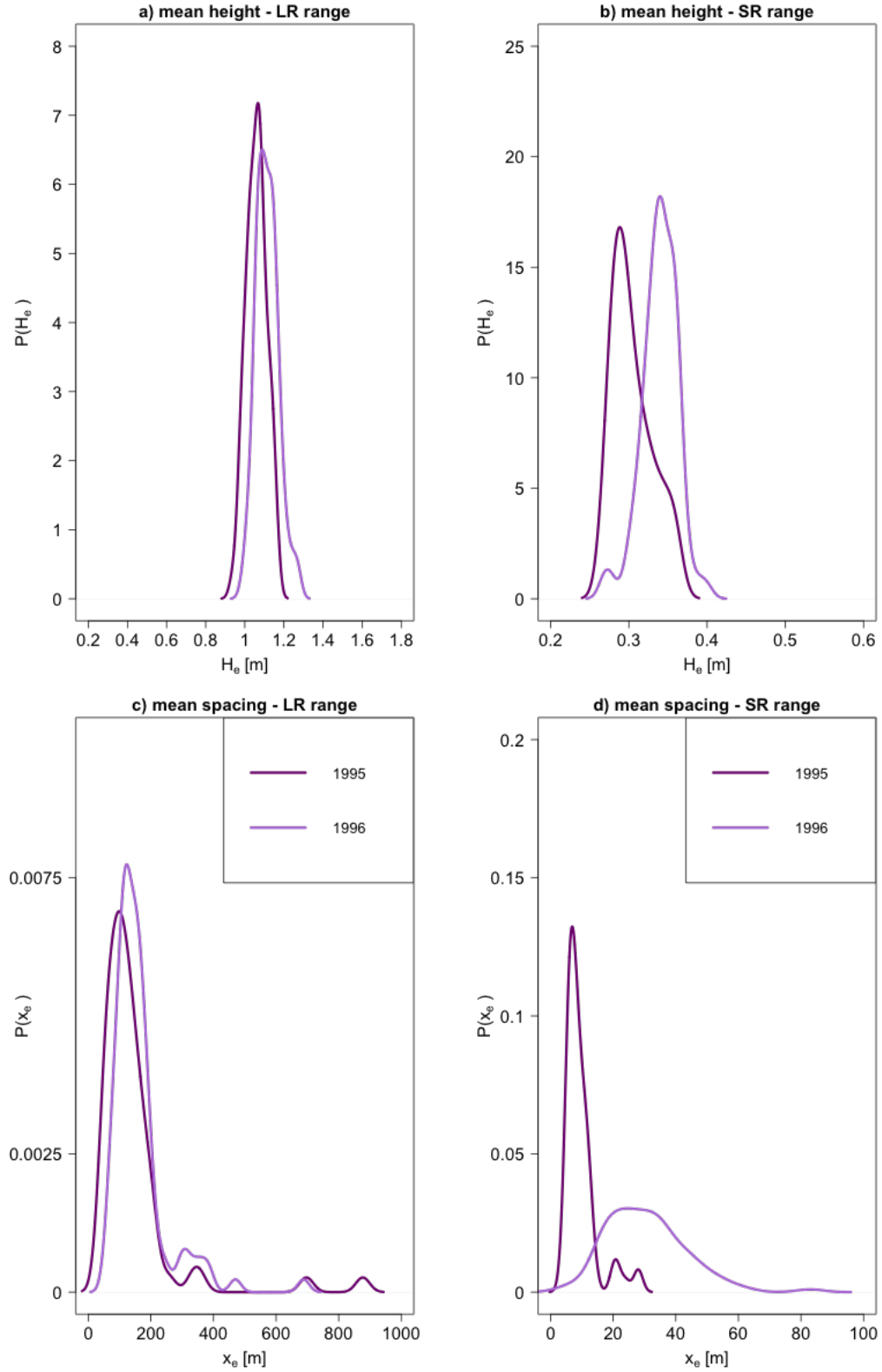


Figure 2.6: PDFs for mean heights of topographic features (a-b) and for mean spacings between topographic features (c-d) in the Laptev Sea. The case of large ridges (LR) is shown in a) and c), while the case of small obstacles (SR) is shown in b) and d).

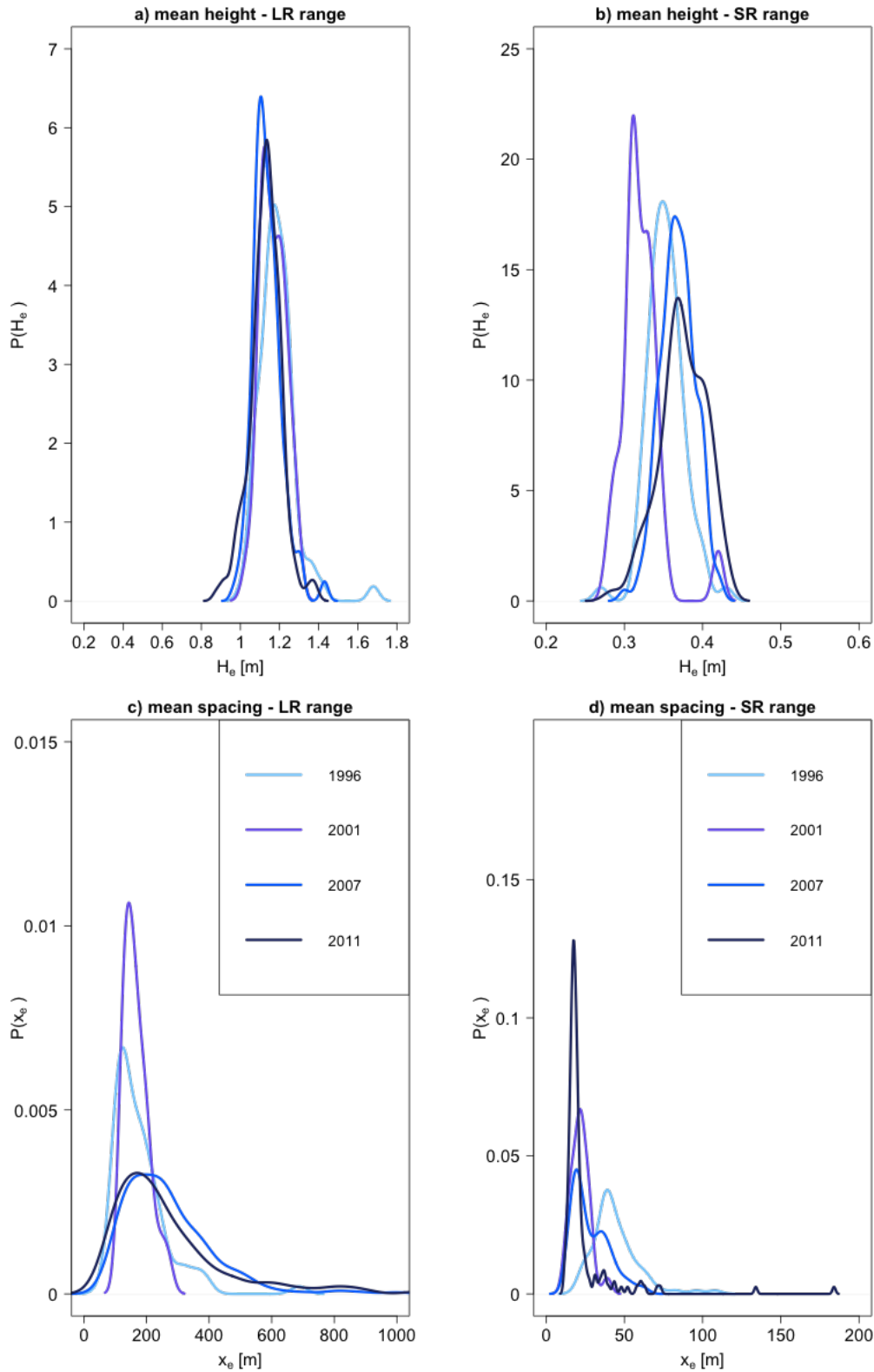


Figure 2.7: PDFs for mean heights of topographic features (a-b) and for mean spacings between topographic features (c-d) in the Central Arctic. The case of large ridges (LR) is shown in a) and c), while the case of small obstacles (SR) is shown in b) and d).

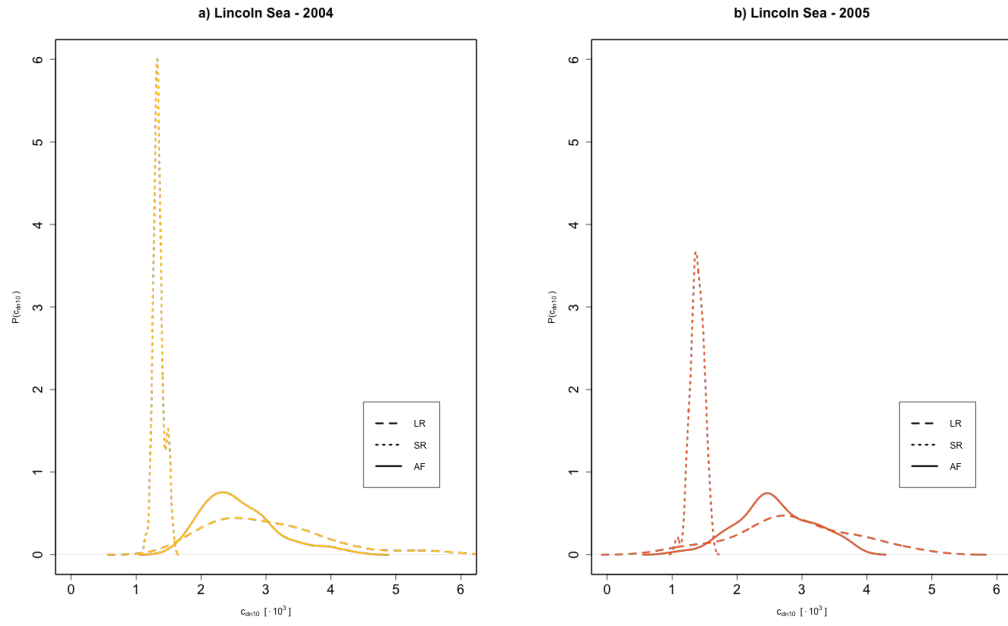


Figure 2.8: PDFs of drag coefficients calculated using Equations 2.1 and 2.3 for the Lincoln sea in 2004 (a) and 2005 (b) for the three ranges: all obstacles together (AF) represented by the solid line, the case of only large ridges considered (LR) represented by the dashed line and the case of only small topographic features (SR) represented with the dotted line.

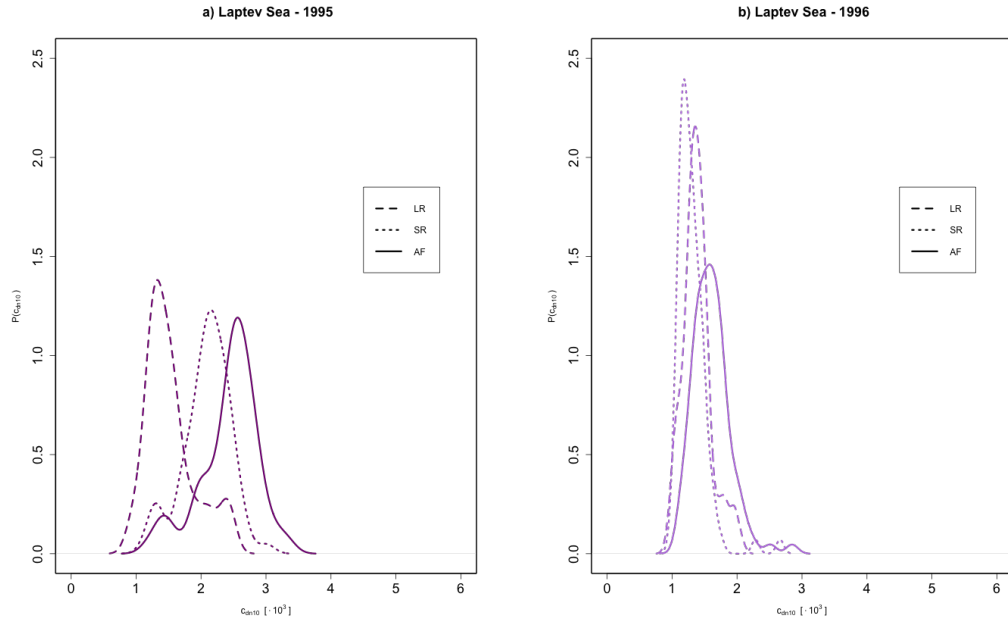


Figure 2.9: PDFs of drag coefficients calculated using Equations 2.1 and 2.3 for the Laptev Sea in 1995 (a) and 1996 (b) for the three ranges: all obstacles together (AF) represented by the solid line, the case of only large ridges considered (LR) represented by the dashed line and the case of only small topographic features (SR) represented with the dotted line.

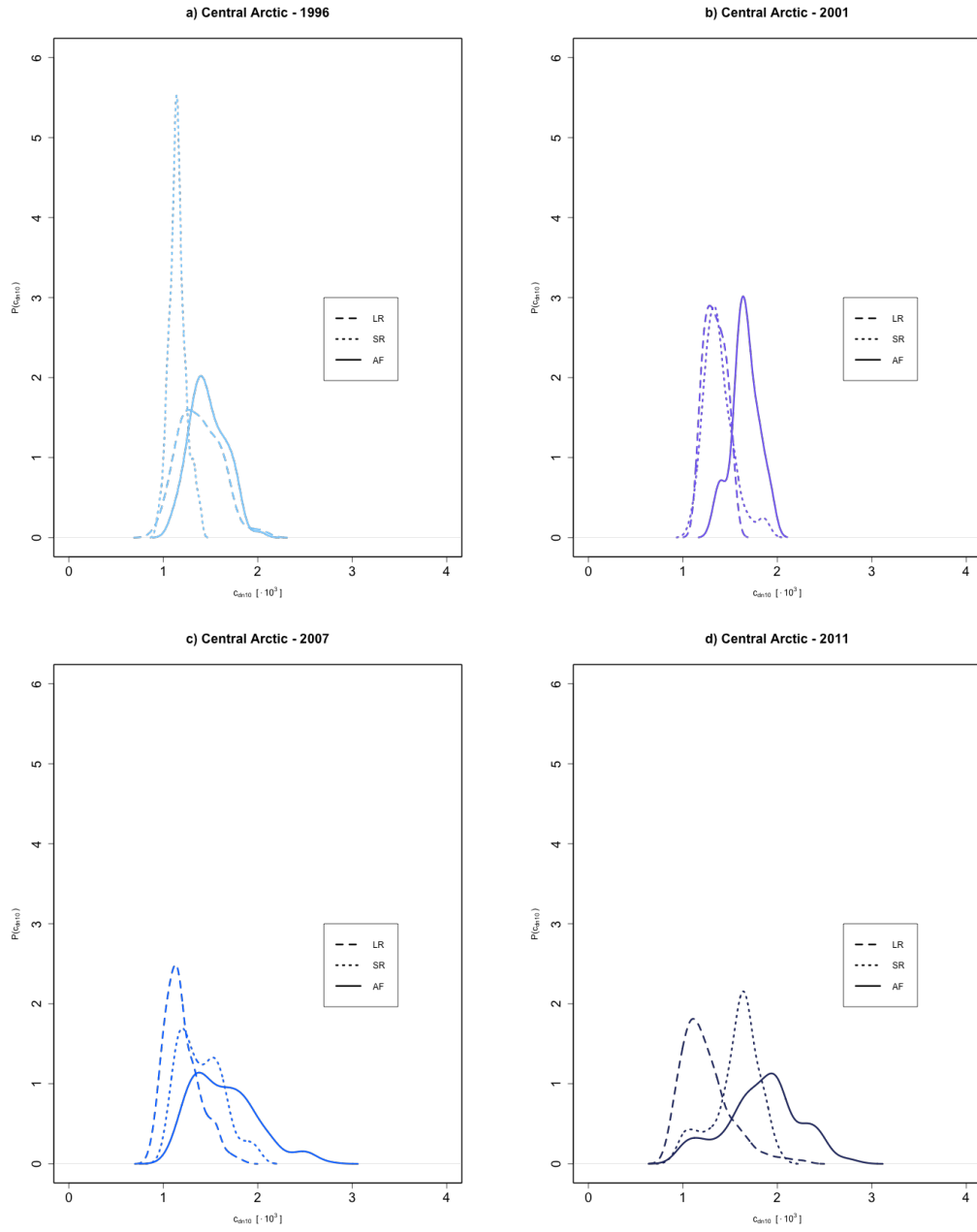


Figure 2.10: PDFs of drag coefficients calculated using Equations 2.1 and 2.3 for the Central Arctic in 1996 (a), in 2001 (b), in 2007 (c) and in 2011 (d) for the three ranges: all obstacles together (AF) represented by the solid line, the case of only large ridges considered (LR) represented by the dashed line and the case of only small topographic features (SR) represented with the dotted line.

As concerns the impact of the different spectral ranges on drag coefficients in the Central Arctic, we see different situations for the different years: In 1996 the drag coefficients are mostly dominated by the LR range, while in 2007 and 2011 the SR range has the largest impact. We will come back to this important finding in the next section.

2.4 Discussion

In the following, we aim to relate the topography parameters presented in Section 2.3.1 to different sea-ice regimes characterized by a different degree of deformation, age of sea ice and its thickness. Moreover, we establish a qualitative relationship between these ice characteristics and the drag coefficients.

For these purposes, it is helpful to consider once more Table 2.1 which contains for each region and year the predominant sea-ice regime characterized by the occurrence of multi-year (MY) ice or first-year (FY) ice taken from the literature (*Haas and Eicken, 2001; Haas and Lieser, 2001; Von Saldern et al., 2006; Haas et al., 2006; Lieser, 2005; Schauer, 2008*). According to Table 2.1, during most campaigns FYI was predominant, but MYI was predominant in the Fram Strait (2004), Lincoln Sea (2004, 2005) and Central Arctic (in the Transpolar Drift, TPD) (1996, 2001).

We turn now to a discussion of results related to the specific regions. In the **Central Arctic**, the mean height of obstacles (2.2b) (AF-range) shows year-to-year differences that do not clearly reflect changes in sea-ice thickness found by others (see, e.g., *Rabenstein et al. (2010); Haas (2004a)*). This shows that the height of obstacles relative to the level ice does not necessarily correlate with the ice thickness. The same conclusion was drawn by *Martin (2007)*, who showed that a relationship between level ice thickness and sail height was not detectable.

When we consider the LR range, the large difference in ridge parameters between 1996/2001 on one hand and 2007/2011 on the other might reflect the shift from MYI in 1996 and 2001 to FYI in 2007 and 2011 as documented by, e.g., *Rabenstein et al. (2010)*. It is also noteworthy that there is at least a hint that the concentration of small topographic features (Figure 2.7d) increases from 1996, 2001 to 2007, 2011. These changes in topography have consequences for the drag coefficients: The higher concentration of obstacles in 2007 and 2011 leads to values roughly 20 % larger than in 1996 and 2001 (Table 2.2). We hypothesize that this contributes to the increase in sea-ice drift speed observed over the last decades (*Spren et al., 2011; Kwok et al., 2013*). Further observational evidence and support from model simulations is desirable. Finally, it is remarkable that in 1996 the values of drag coefficients are mainly dominated by the LR range (as for the Lincoln Sea and Laptev Sea in 1996), while in 2007 and 2011 the SR range has the larger impact on the calculated drag

coefficients.

In the **Fram Strait**, the large differences in the PDFs for mean heights (Figure 2.2c), mean distances (Figure 2.3c) and drag coefficients (Figure 2.4c) between 2004 on one hand side and the years 2003 and 2007 on the other hand might be explained by the age of ice: in 2004 we have predominantly MYI whereas in 2003 and 2007 the ice was mostly FYI. We can deduce also from the corresponding drag coefficients that older ice, but only in this region, has a rougher surface. Nevertheless, the ice that is found in the Fram Strait can originate from different inner Arctic regions along the Transpolar Drift or from the western part of the Arctic. Thus it is possible that the 2004 conditions are a consequence of variability in other regions, such as the Lincoln Sea, rather than of local processes.

The **Lincoln Sea** region is characterized by a high degree of deformation (*Martin*, 2007). Moreover, the ice found in this region is MYI (Table 2.1) and the observations were obtained in May before the beginning of the melt season. These factors together contribute to the large mean height of obstacles. In this region, as in the Fram Strait, we see a link between MYI and high values of the drag coefficients.

In the **Laptev Sea**, (2.2e-2.3e) the large difference between the years 1995 and 1996 cannot be explained by the age of the ice (see Table 2.1). A relevant point here is that in 1996 there was a deep snow layer which covered probably the smallest roughness elements. This can be the reason why in 1996 the LR range has the strongest impact on the drag coefficients. Vice versa, the contribution of the LR range to the drag coefficients is negligible in 1995.

In general, although Equation 2.3 suggests that H_e and x_e have a similarly strong effect on the drag coefficient, we find that the variability of x_e is greater than that of H_e and hence can dominate the drag coefficients. In line to what was shown by *Martin* (2007), the aspect ratio is dominated by the spacing between obstacles, since the order of magnitude of the variation of this quantity is greater than that of the obstacle height variations.

Finally, we emphasize that the drag coefficients presented here are based on a parameterization. The uncertainty is thus in the range of $\pm 20\%$. This number is based on comparison with measured drag coefficients. The largest source of uncertainty is probably the necessary assumption on the random orientation of the obstacles (see Section 2.2.3). However, the good agreement of the calculated values with SHEBA data shows that our assumption is reasonable.

Our results have shown that there are some implications for modelling as well. The large variability of atmospheric drag coefficients by roughly half an order of magnitude would result in the same variability of near-surface atmospheric momentum fluxes. It can be expected that there is a large response in the modelled sea-ice concentration when the topography dependent parameterizations are used in both

sea-ice stand alone and coupled air-ice-ocean models, which has most recently been demonstrated by *Tsamados et al.* (2014). Thus a first step for models could consist in the use of Table 2.2 providing mean values of drag coefficients that can be used for sensitivity studies. The values presented for different regions can also be used in regional models. Finally, the PDFs presented for the drag coefficients offer, for different regions, mean values and a measure of possible variability that can be used to compare results obtained with numerical models where a parameterization of drag coefficients is implemented.

2.5 Summary and Conclusion

A data set of more than 10000 km of sea-ice topography obtained by laser altimeter measurements was used for the present study. This data set is inhomogeneous, since it covers different regions, years, and times of the years. Nevertheless, the high spatial resolution of the data allows us to investigate the variability of the sea-ice surface over key regions of the Arctic basin and its implication for the atmospheric drag coefficients. Following the work done by *Garbrecht et al.* (1999), *Garbrecht et al.* (2002) and also motivated by *Andreas* (2011), this study represents an attempt to relate the measured sea-ice topography to atmospheric drag coefficients.

In particular, the PDFs for mean heights and mean spacings between topographic features, calculated over 10 km profiles, have been presented for different regions of the Arctic (Laptev Sea, Central Arctic, Beaufort Sea, Lincoln Sea, Fram Strait), different years (1995, 1996, 2001, 2003, 2004, 2005, 2007, 2011) and different seasons (summer and late winter). Typical values are 0.45 m for the mean height and 20 m for the mean spacing, but the variability is high, in particular that of the mean separation between obstacles. Moreover it is shown that the spatial variability is stronger than the temporal variability.

Further insight is obtained by splitting the total spectrum into two ranges, one representing the small topographic features between 0.2 m and 0.8 m height and another one representing the large pressure ridges (≥ 0.8 m). Such analysis shows the important result that the consideration of only pressure ridges is not enough to characterize the roughness degree of an ice field. In the Lincoln Sea, the ice topography is dominated by large pressure ridges, while it is dominated by the small roughness elements in other regions (e.g., Central Arctic). Moreover, in the Central Arctic the spacing of small obstacles is much smaller in the later years than in 1996/2001 and the number of the large pressure ridges decreases between 1996 and 2011. This suggests a shift to a different ice regime that is consistent with a reduction of MYI: A thinner ice is more easily broken forming fields of rubbles and piles but it is not able to stand the high stress that can generate large pressure ridges

(Parmeter, 1975).

The large variability in the surface topography is reflected in the drag coefficients. This was shown by calculating drag coefficients on the basis of a parameterization using the topography data. Obtained values are close to those found from direct turbulence measurements described in the literature. In particular, it is shown here that the drag coefficients are more affected by the separation between obstacles (i.e., by their concentration) than by their height, which confirms the results of *Lüpkes and Birnbaum* (2005) for the marginal sea-ice zone. It is furthermore interesting that the increase in concentration of obstacles and the shift in sea-ice regime in the Central Arctic is reflected in the drag coefficients: Mean values are larger in 2011 and 2007 than in 1996 and 2001, especially due to a tail of the spectra towards larger values.

Based on the splitting into two spectral ranges, it was found that the impact of the large pressure ridges on the drag coefficients is relevant only in ice regimes characterized by heavily deformed ice (e.g., the Lincoln Sea) with mean ridge spacing smaller than 100 m. In other regions, the largest impact is due to minor roughness elements. Thus, it is desirable to further study the impact of small topographic features, such as melt pond and floe edges, in the future.

Acknowledgments

Part of this work was funded by the German Federal Ministry of Education and Research (FKZ: 01LP1126A) as part of Miklip. We thank the crew of RV Polarstern and the HeliService International GmbH. We are also thankful to all the people who contributed to collect the laser altimeter data and in particular to Christian Haas. Finally, we thank the reviewers and Dr. Tsamados for their constructive comments. All data used for this study are made available on request.

Chapter 3

Paper II: Impact of Sea Ice Bottom Topography on the Ekman Pumping

Abstract

Sea-ice elevation profiles and thickness measurements have been collected during summer 2011 in the Central Arctic. These two different data sets have been combined in order to obtain surface and bottom topography of the sea ice. From the bottom profile, the keels of ridges are detected. Then, a parameterization of oceanic drag coefficients that accounts for the keels depth and density is applied. The calculated oceanic drag coefficients are highly variable (between about $2 \cdot 10^{-3}$ and about $8 \cdot 10^{-3}$) within the range of observed values. In order to estimate the contribution of variable drag coefficients on the Ekman pumping, the calculated drag coefficients are used in an idealized model experiment, where sea ice is drifting at constant velocity on an ocean at rest. The resulting variations of the Ekman vertical velocity are in the same order of magnitude as for variable ice velocity at the surface. In most state-of-the-art general circulation models, the variations of drag coefficients are not taken into account. The simple experiment carried out in the present study suggests that neglecting this contribution can lead to an incorrect representation of the momentum exchange between ice and ocean and to an underestimation of the Ekman pumping, with consequences for the large scale ocean circulation.

3.1 Introduction

The sea ice in the Arctic Ocean has a surface and bottom topography that is characterized by many different scales from small hummocks and piles of ice to large ridges. A pressure ridge consists of a part that extends into the atmosphere (sail) and a part that extends into the ocean (keel).

The sails are usually above one meter, sometimes they can be as high as 2 m. In order to satisfy the hydrostatic equilibrium, the keels usually extend much deeper into the ocean and may reach depths of 30 m (*Pite et al.*, 1995). The formation of these topographic features depends on the ice motion. In particular, large pressure ridges are formed when the ice is exposed to strong convergence.

The main forces that govern the ice motion are the internal forces (*Steele et al.*, 1989), the local winds and the ocean currents (*Thorndike and Colony*, 1982). In the momentum balance equation that describes the ice motion, the interactions between air, ice and water are parameterized by drag coefficients. These drag coefficients must account for sea-ice surface characteristics on the near-surface transport of momentum. The sea-ice surface is spatially and temporally inhomogeneous and thus we can expect spatial and temporal variations of the drag coefficients as well.

Many studies addressed the dependence of the drag coefficients on the surface topography of the ice. In particular, for the atmospheric drag coefficients, parameterizations for numerical models have been developed (see, e.g., *Birnbaum et Lüpkes* (2002); *Garbrecht et al.* (2002); *Lüpkes and Birnbaum* (2005); *Lüpkes et al.* (2012, 2013)). In these parameterizations the atmospheric drag coefficients are a function of surface characteristics of the ice (i.e., melt ponds, pressure ridges, floe edges). Only very few studies focused on the oceanic drag coefficients. Among these few, the studies by *Steiner et al.* (1999) and *Steiner* (2001) relate the drag coefficients to the roughness of the ice, whereas in *Lu et al.* (2011) the oceanic drag coefficients are expressed as a function of observable geometric parameters of the sea ice such as the depth of keels, the mean separation between ridges, and the floe edges.

The momentum transferred by wind or ice to the ocean is redistributed by vertical turbulent mixing from the surface to a certain depth. The layer with turbulence, that is where the vertical variations of the surface stress are not negligible, is called the *Ekman layer*. The fluxes of momentum lead to the formation of a velocity field in the surface layer of the ocean. Associated with the induced velocity is the vertical *Ekman pumping* (when directed downwards) or *Ekman suction* (when directed upwards). The Ekman pumping (suction) depends on the wind stress applied at the upper surface and represents the amount of volume pumped from below into (or from above out of) the Ekman layer. It was also shown (*Rabe et al.*, 2011) that variations in Ekman pumping affect the depth of the 34-isohaline with consequences for the entire ocean circulation. In most state-of-the-art global circulation models, the stress at

the ice-ocean interface depends on the variability of the wind field, while variations in the drag coefficients are usually not taken into account. In the present study we calculate oceanic drag coefficients as function of observed ice topography. These drag coefficients are then used to illustrate the effects on Ekman pumping when only the spatial variations of the oceanic drag are considered.

3.2 Data and Methods

The data used for this study were collected by helicopter flights over the Arctic Ocean during a campaign with the ice breaker *RV Polarstern* in summer 2011. The map with the tracks along which the data have been collected is shown in Figure 3.1.

During the campaign, two different types of data have been collected: sea-ice surface elevation profiles using a laser altimeter and sea-ice thickness using the so-called ‘EM-bird’. The laser altimeter profiles are collected using a Riegel LD90-3100HS that was introduced in 2001. This instrument has a wavelength of 905 nm, a sampling frequency of 100 Hz and an accuracy of ± 1.5 cm. The point spacing is about 30-40 cm. The profiles recorded by the laser altimeter show an altitude variation due to the surface roughness of the ice and a variation at a lower frequency due to the movement of the helicopter. In order to remove this movement, a combination of low and high pass filters is used (*Hibler, 1972*).

The EM-bird is a device to measure the sea-ice thickness directly using electromagnetic induction (*Haas, 2004b; Haas et al., 2009*). The EM-bird contains two coils for transmission and receptions of electromagnetic fields and can measure the distance between the instrument and the ice-ocean interface by using the electromagnetic field generated by induction in the conductive sea water. In addition, a laser altimeter (as described above) gives the distance of the instrument to the surface (ice or snow), hence the thickness is obtained by the difference between laser and EM measurements. The sea-ice thickness is sampled at 10 Hz, which leads to an average point spacing of ~ 4 m. The footprint of the instrument is about 40 m (*Kovacs et al., 1995; Reid et al., 2006*). Ice thickness samples thinner than 0.1 m are considered as open water. Since sea-ice surface and underside profiles are recorded at the same time we can have a complete description of the ice topography on the surface and underneath the ice.

In order to obtain information about the bottom topography of the ice, in each point where both measurements are available, the thickness recorded with the EM-bird is subtracted from the filtered laser altimeter profiles. The spatial resolution is lower than the one for the upper surface (30-40 cm) since the thickness measurements are recorded every ~ 4 m. A routine is then applied to the filtered profile to select

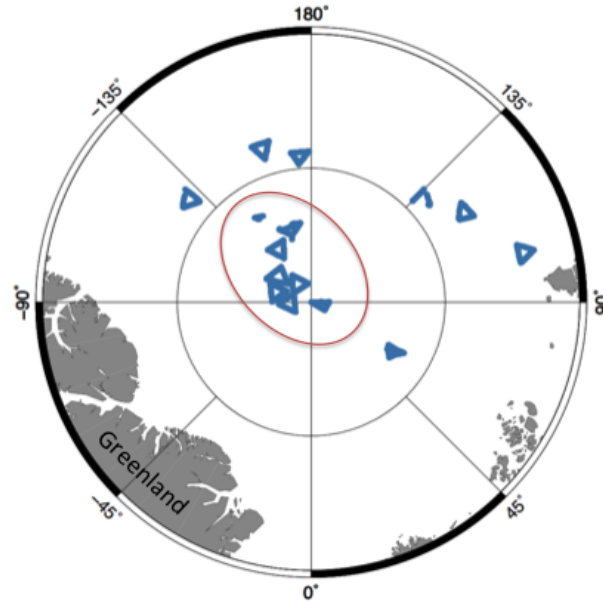


Figure 3.1: Map of the Arctic Ocean with the location of the laser altimeter and EM-bird measurements. The red circle encloses the measurements taken in the area that in the present study is referred to as the Central Arctic.

minima that are deeper than a certain threshold value. The procedure is the same as used in other studies for the detection of sails from surface ice profiles (e.g. *Von Saldern et al.* (2006) and *Rabenstein et al.* (2010)). Values ranging from -5 m to -9 m can be used as thresholds for keel detection (*Williams et al.*, 1975; *Davis and Wadhams*, 1995). Here we assume a sail height to keel depth ratio of 4 (*Timco and Burden*, 1997). In the studies by, e.g., *Rabenstein et al.* (2010) and *Von Saldern et al.* (2006) a sail height of 0.8 m is used as threshold value for the identification of sails. This gives a threshold value for the keel depth equal to -3.2 m. Since the EM-bird underestimates the real thickness of ridges by up to 50-60% (*Haas*, 2004b), we finally choose a cut-off depth of -1.5 m. Moreover, two adjacent keels have to satisfy the Rayleigh criterion: the minima points must be separated by a point whose depth is less than half of the depth of the keel in order to be resolved as separate entity (*Hibler*, 1975; *Wadhams and Davy*, 1986; *Wadhams and Horne*, 1980). An example of a final profile is shown in Figure 3.2. The depth of the keels that are detected and shown in Figure 3.2 are then multiplied by a factor of 2 in order to account for the systematic underestimation of the maximum draft by a factor of 2 due to the EM technique (*Martin*, 2007; *Haas*, 2004b).

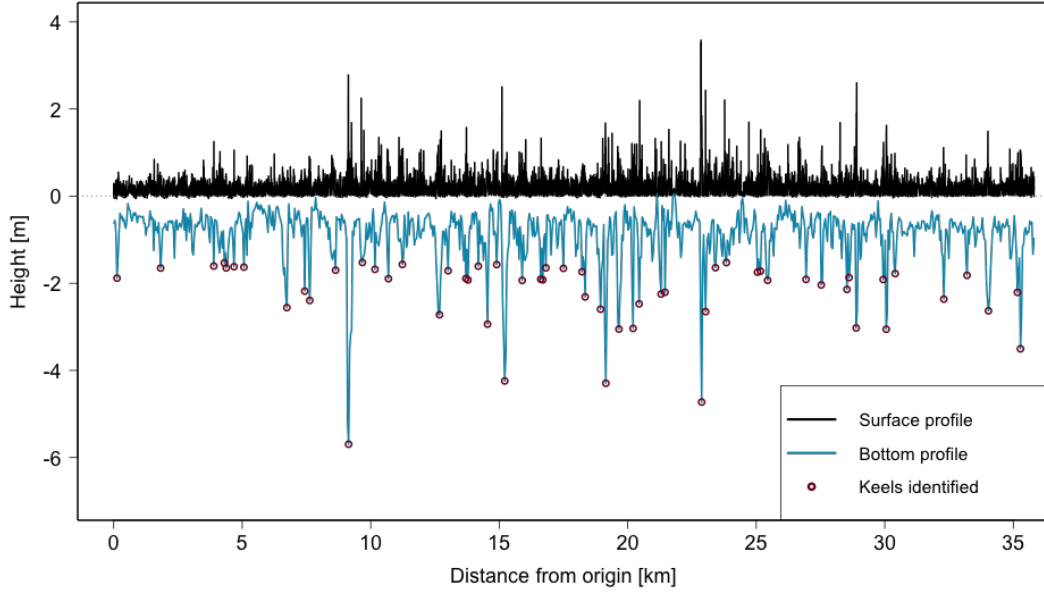


Figure 3.2: An example of a sea-ice profile of ca. 35 km length. The black line shows the upper surface profile obtained by the filtered laser altimeter data. The light blue line represents the bottom profile of the ice obtained by subtracting the thickness from the laser altimeter profiles. The circles represent the detected keels. The depth of the keels is then multiplied by a factor of 2 as described in Section 3.2.

3.3 Calculation of Oceanic Drag Coefficients

In order to calculate the oceanic drag coefficients we make use of a parameterization presented in *Lu et al.* (2011). This parameterization is based on a partitioning concept that was already introduced for atmospheric drag coefficients in *Arya* (1973, 1975). The parameterization in *Lu et al.* (2011) distinguishes between the influence of small scale roughness (skin drag) and larger obstacles such as the keels associated with ridges and the edges of the ice floes (form drag). Since we focus our analysis on areas with 100% sea-ice cover, the contribution of floe edges can be neglected.

The oceanic drag coefficient c_w is then the sum of the skin drag c_w^s and the form drag due to ridges c_w^r :

$$c_w = c_w^s + c_w^r. \quad (3.1)$$

The drag contributions, in the case of sea-ice concentration A equal to 1, are calculated as following:

$$c_w^s = C_s \left(1 - m \frac{H_r}{D_r} \right), \quad (3.2)$$

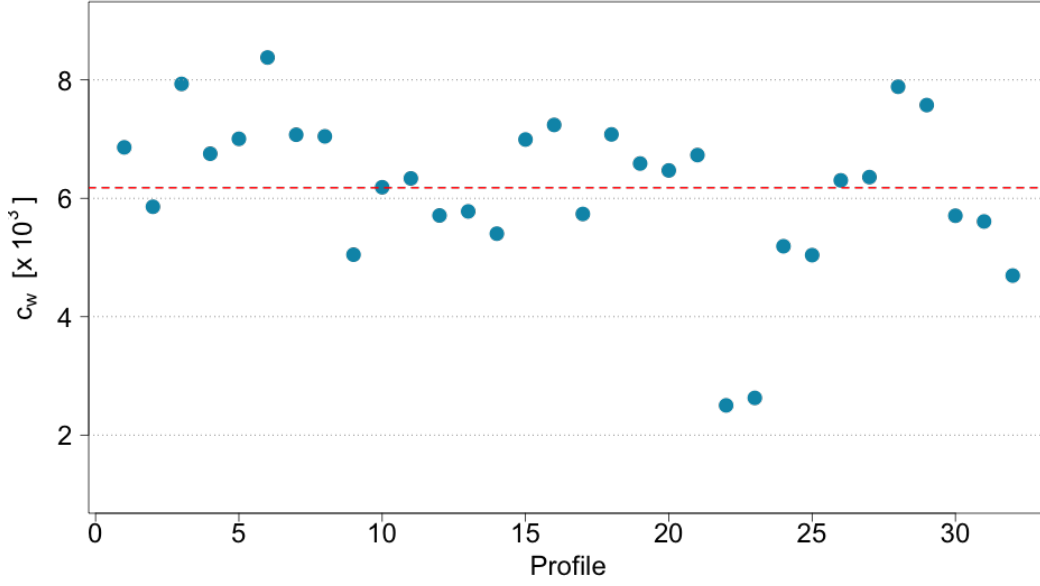


Figure 3.3: Values of the oceanic drag coefficients c_w calculated for the Central Arctic. The red line represents the mean value.

$$c_w^r = \frac{C_r H_r}{\pi D_r} \left[1 - \left(\frac{H_r}{D_r} \right)^{1/2} \right]^2. \quad (3.3)$$

H_r and D_r are the mean depth of the keels and the mean separation between them respectively. The remaining constants are: $m = 1$, $C_r = 0.5$ and $C_s = 2 \times 10^{-3}$.

For the calculation of the drag coefficients we need to compute the mean depth of the keels H_r and the mean separation D_r between them as obtained from the available data. We focus on the Central Arctic region (see Figure 3.1). There, we have 320 profiles. The length of each profile varies between ca. 10 km and 30 km for a total of more than 700 km of data. For each profile we detect the keels as described in Section 3.2 and we calculate the mean depth and the mean spacing between them. With this information we can calculate the drag coefficients for each profile. The results are shown in Figure 3.3.

Only a few measurements of oceanic drag coefficients are available for comparing the results obtained with Equations 3.2 and 3.3. *Lu et al. (2011)* showed (see their Table 1) that oceanic drag coefficients can vary from 1×10^{-3} to even 22×10^{-3} . Our calculated values lie within this range. We stress that the oceanic drag coefficients vary strongly with the sea-ice topography and that the choice of a constant value used in global circulation models might imply a bias in the estimation of the momentum exchange between the ice and the ocean.

3.4 Ekman Pumping

Ekman pumping in the ocean depends on the spatial variation of the stress applied at the surface. This spatial variation is a consequence of variations in both the velocity field and the drag coefficients. In this section we want to evaluate the contribution to Ekman pumping that is caused only by variations of the drag coefficients. We thus set up a very simple experiment. 32 grid cells aligned along y , each 20 km wide, form a domain of 20 km \times 640 km. This domain is covered completely with sea ice (100 % sea-ice cover). The surface and bottom properties of the ice are varying from one cell to the other, so that the drag coefficients are also different. In particular, to each grid cell we assign a value for the drag coefficient that was calculated (see Section 3.3) on the basis of real sea-ice topography. We assume that the ice is in motion along x with a constant velocity $v_{\text{ice}} = 0.05$ m/s while the ocean is at rest. We then compute the Ekman pumping with:

$$w_E = \hat{z} \cdot \nabla \times \frac{\boldsymbol{\tau}}{\rho_0 f}, \quad (3.4)$$

where ρ_0 is the mean density of the sea water, $\boldsymbol{\tau}$ is the stress at the surface, f is the Coriolis parameter. The stress term $\boldsymbol{\tau}$ is given by:

$$\boldsymbol{\tau} = \rho_0 c_w |\mathbf{v}_{\text{ice}}| \mathbf{v}_{\text{ice}}. \quad (3.5)$$

The formulation (Equation 3.4) of the Ekman vertical velocity is only valid for large domains in a steady state and our 20 km grid axes may be too small. Nevertheless we can use such a simplified formulation because we are not primarily interested in quantifying actual Ekman pumping, but we would like to illustrate the importance of variations in the value of oceanic drag coefficients alone on the Ekman pumping. The results of our calculations are shown in Figure 3.4. In this simple experiment there would not be Ekman pumping if the drag coefficients were constant in the whole domain. The range of variations of the vertical velocity is between -20 cm/day and 30 cm/day. Simulated variations in the Ekman vertical velocity based on variations of the surface stress when no keels are taken into account are shown in *Rabe et al.* (2011) (their Figure 6): Here the range of variations of annual mean vertical velocities over different regions in the Arctic is between -5 cm/day and 3 cm/day. In *Rabe et al.* (2011) the variations in the ocean-surface stress are caused by variations only in the wind field and not by variations in the drag coefficients. In our study we see a much higher variation than in *Rabe et al.* (2011) but we stress once more that their result shows variations averaged over the entire basin while here we focus on local variations.

From the results of this calculation we can conclude that the variations in Ekman

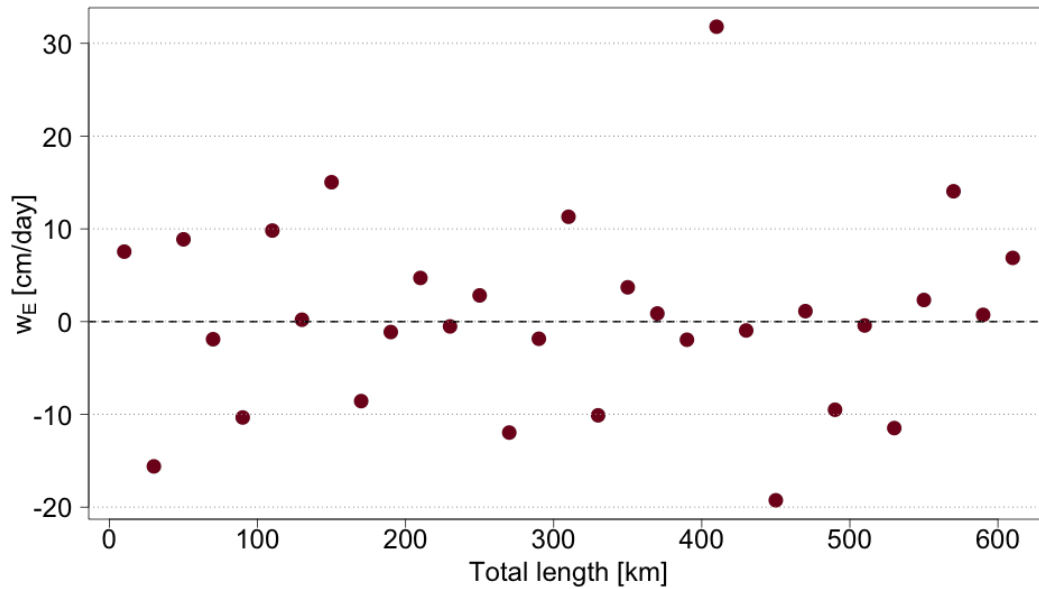


Figure 3.4: Ekman pumping calculated for the idealized situation described in Section 3.4.

pumping associated with variable oceanic drag coefficients is at least in the same order of magnitude as the variations due to changes in the surface velocity of the ice. Even though the strong local effect might be damped when averages are taken over a larger area, we can still assume that the effect will remain of the same order of the velocity variations shown by *Rabe et al.* (2011). Thus we speculate that the presence of different sea-ice regimes on a large scale may induce a basin-scale variation in Ekman pumping that then would have consequences for the Ekman transport and the large scale ocean circulation. Numerical experiments and simulations with large scale sea ice-ocean models could help to investigate the effect on an Arctic basin scale ocean circulation.

3.5 Summary and Conclusion

Airborne altimetry and EM-bird observations have been used in the present study to reconstruct the surface and bottom topography of the sea ice.

From the obtained profiles we detected the keels and calculated keel mean depth and keel mean separation along profiles of different length. This information is then used to calculate the oceanic drag coefficients. These coefficients are calculated by applying a parameterization presented in *Lu et al.* (2011) to a hypothetical situation of 100% sea-ice cover. The calculated drag coefficients are in the range of values obtained by in-situ observations. The range of variability is large and this suggests that the choice of a constant drag in sea-ice numerical models might lead

to a misrepresentation of the actual ice-ocean momentum transfer.

The calculated oceanic drag coefficients have been used for a rough calculation of Ekman pumping. The results provide an insight into the expected magnitude of Ekman pumping caused by the variability of the oceanic drag coefficients. The upper layer vertical velocity generated by variations in drag coefficients is on the same order of magnitude as for variable ice velocity at the surface. In order to better understand the importance of the variable drag coefficients on the large scale oceanic circulation, Pan Arctic simulations with global circulation models are required. The results shown here suggest that neglecting the contribution of variable oceanic drag coefficients in the momentum transfer between ice and ocean can lead to considerable errors in numerical models or data analysis.

Acknowledgments

We would like to thank the crew of the RV Polarstern and the HeliService International GmbH. Moreover we thank all the people who contributed to collect the laser altimeter data and EM-bird data, in particular Stefan Hendricks. We are also very thankful to Michael Karcher for the interesting and constructive discussions. Finally we thank the Earth System Science Research School (ESSReS) for any support to this study and to the PhD project.

Chapter 4

Paper III: Sea Ice Drag as Function of Deformation and Ice Cover: Effects on Simulated Sea Ice and Ocean Circulation in the Arctic

Abstract

Many state-of-the-art coupled sea ice-ocean models use atmospheric and oceanic drag coefficients that are at best a function of the atmospheric state but otherwise constant in time and space. Since observations of turbulent fluxes imply high variability of drag coefficients, constant drag coefficients might lead to an incorrect representation of the ice-air and ice-ocean momentum exchange. We compare two model runs, one with constant drag coefficients and one with drag coefficients varying as function of ice concentration and deformation. The main sea ice parameters, that is ice concentration, thickness and drift, are affected. In particular, the ice moves faster with variable drag coefficients and this leads to a stronger Beaufort Gyre and to a stronger Transpolar Drift Stream. Large changes in thickness are seen in the Lincoln Sea, from where more ice is removed and exported through the Fram Strait due to higher atmospheric drag coefficients, leading also to a larger export of sea ice. The ocean is also affected by the implementation of variable drag coefficients. The mixed layer is deeper and the stream function shows a clearer anticyclonic pattern in the Beaufort Sea. The stronger Beaufort Gyre increases the downwelling in the central Beaufort Sea which leads to a depression of the 34-isohaline. As a consequence the Atlantic Water cyclonic circulation slows down in that region.

4.1 Introduction

The Arctic ocean has undergone drastic changes during the last decades. In particular, the most striking evidence of climate warming is revealed in changes of the most defining feature of the Arctic Ocean, the sea ice. The last thirty years saw sea ice thinning and its areal extent shrinking (*Rothrock et al.*, 1999; *Serreze et al.*, 2003, 2007; *Stroeve et al.*, 2007, 2011, 2012; *Laxon et al.*, 2013). But besides this area and volume reduction, also the surface characteristics of the sea ice are changing. Mostly in the last decade, the sea ice regime underwent a shift from predominantly multi-year ice (MYI) to predominantly first-year ice (FYI) (*Haas et al.*, 2008; *Rabenstein et al.*, 2010). Moreover, the abundance and height of pressure ridges are decreasing (*Rabenstein et al.*, 2010; *Castellani et al.*, 2014), mostly in the central Arctic.

These sea ice changes feed back into global climate change because sea ice is coupled to atmosphere and oceans. Sea ice insulates the oceans from the polar atmosphere, it contributes to the ice-albedo feedback mechanism, and, while drifting, it exerts a drag on the oceanic surface layer. This leads to fluxes of momentum into the ocean. The momentum fluxes between ice and ocean affect the upper surface circulation with consequences for the interior ocean circulation and the outflow into the Nordic Seas as well as the Pacific and Atlantic Ocean. Understanding the dynamic coupling between ice, atmosphere and ocean requires a detailed representation of the momentum fluxes. In a period of substantial changes, the physics describing the sea-ice evolution and its coupling with atmosphere and ocean has been substantially improved in global circulation models. Following this line, in the present work we investigate how numerical simulations are affected by a new description of ice-atmosphere and ice-ocean coupling that accounts for the sea-ice roughness.

Nowadays, most sea-ice codes resolve both dynamic and thermodynamic processes. In particular, the sea ice momentum equation is solved for drift velocities that are then used to advect the ice variables and that contribute to the stress acting on the ocean. Sea-ice motion is determined by three main forces: the internal stresses in the ice, the atmospheric drag force and the oceanic drag force (*Steele et al.*, 1989). In most sea-ice models (*Hibler*, 1979; *Hunke*, 2010), the atmospheric and oceanic drag is described by a quadratic relationship:

$$\boldsymbol{\tau}_{a,w} = \rho_{a,w} c_{a,w} |\mathbf{U}_{a,w} - \mathbf{u}| R_{a,w} (\mathbf{U}_{a,w} - \mathbf{u}), \quad (4.1)$$

where $\rho_{a,w}$ is the air or water density, $\mathbf{U}_{a,w}$ is the velocity of the wind or currents, \mathbf{u} is the velocity of the ice, $R_{a,w}$ are rotation matrices that act on the wind or current vector to account for unresolved Ekman layers and $c_{a,w}$ are the transfer coefficients for momentum, called air or water drag coefficients. These coefficients determine the intensity of air-ice and ocean-ice interactions. It is well established by many observa-

tions of turbulent fluxes over Arctic sea ice (*Overland*, 1985; *Lüpkes and Birnbaum*, 2005; *Andreas et al.*, 2010, 2012) that the atmospheric and oceanic drag coefficients depend on sea-ice surface characteristics. Reported values are about 1×10^{-3} to 9×10^{-3} for the atmospheric drag coefficients and about 1×10^{-3} to 35×10^{-3} for the oceanic drag coefficients (*Overland*, 1985; *Guest and Davidson*, 1991; *Lu et al.*, 2011). Many sea-ice models that are used in coupled GCM today, use constant drag coefficients, thus they do not account for the observed spatial and temporal variability. Nevertheless, in recent years many parameterizations have been developed to relate sea-ice surface characteristics to drag coefficients (*Garbrecht et al.*, 2002; *Birnbaum et al.*, 2002; *Lüpkes and Birnbaum*, 2005; *Lüpkes et al.*, 2012, 2013; *Andreas et al.*, 2010; *Lu et al.*, 2011). In particular, *Tsamados et al.* (2014) present the results of a simulation with the Los Alamos sea-ice model CICE where some of the mentioned parameterizations are used to compute the atmospheric and oceanic drag coefficients as function of floe edges, ridges and melt ponds. *Tsamados et al.* (2014)'s approach requires a dynamic ice thickness distribution (ITD) as well as an explicit description of ridges and melt ponds formation (*Flocco and Feltham*, 2007; *Flocco et al.*, 2010). In a different approach (*Steiner et al.*, 1999; *Steiner*, 2001) deformation energy is introduced to account for surface roughness. The deformation energy depends on the history of the mechanical properties of the ice and on changes in its thickness. The drag coefficients are parameterized as function of the deformation energy and ice concentration (*Steiner*, 2001). With this formulation it is possible to implement drag coefficients in sea-ice models without additional parameterizations for ridges and melt ponds formation.

Tsamados et al. (2014) and *Steiner* (2001) used stand alone sea-ice models. But the variations of oceanic drag coefficients also affect the oceanic momentum through the drag coefficients in the expression for τ_w and the drift velocities of the ice that are themselves functions of the atmospheric and oceanic stress. For example *Castellani et al.* (2015) (Chapter 3) showed, based on an idealized experiment, that variations in the Ekman vertical velocity associated with variable oceanic drag coefficients are on the same order of magnitude as the variations due to changes in the surface velocity of the ice.

Sea-ice drift and surface layer currents in the Arctic are characterized by two main flow fields (*Carmack*, 2000): The first is the Transpolar Drift (TPD), in which sea ice and surface waters move from the Eurasian Basin across the North Pole and then through the Fram Strait. The second is the anticyclonic Beaufort Gyre in the Canadian Basin. The Atlantic Water (AW) occupies the so called Atlantic Water Layer (AWL) which extends in the intermediate depth range of about 200 to 1200 m below the halocline. It forms cyclonic gyres in the Eurasian Basin and the Canadian Basin (*Rudels et al.*, 1994). The Arctic pathways of the AW has been thoroughly

investigated by using observations (*Carmack et al.*, 1995; *Rudels et al.*, 1999; *Swift et al.*, 1997) and model simulations (*Holland et al.*, 1996; *Karcher and Oberhuber*, 2002; *Karcher et al.*, 2003). Nevertheless, the stability of surface and intermediate water circulation and its relation to climate forcing has not been fully understood yet. According to *Karcher et al.* (2012), a stronger Beaufort Gyre results in a suppression of the cyclonic boundary current of mid-depth Atlantic water in the Beaufort Sea. Thus we might expect that changes in the surface stress representation and in the resulting sea-ice drift might affect the ocean circulation at different depths.

In the present study we investigate the effects of atmospheric and oceanic drag coefficients that depend on the degree of sea-ice deformation. In contrast to *Tsamados et al.* (2014), we follow the *Steiner* (2001) deformation energy approach and apply it to a coupled sea ice-ocean model. In particular, we focus on the simulated sea-ice properties, but also on effects and changes in the ocean circulation, with the aim to answer the following questions: 1) which of the main physical parameters describing the large scale sea ice cover (ice concentration, thickness and drift) is affected the most? 2) In which regions of the Arctic we see larger changes? 3) To which extent is the ocean affected?

In Section 4.2 we introduce the model configuration and the implemented parameterizations. The results presented in Section 4.3 for sea ice and ocean are then discussed in Section 4.4. A summary and conclusion follow in Section 4.5.

4.2 Methods

4.2.1 Model Description and Setup

We use the Massachusetts Institute of Technology general circulation model (MIT-gcm) (*Marshall et al.*, 1997; *MITgcm group*, 2014) in a coupled ocean-sea ice Arctic Ocean configuration. The configuration is similar to the NAOSIM configuration of (*Karcher et al.*, 2011) and was already used and described in *Castro-Morales et al.* (2014). The domain covers the Arctic Ocean, the Nordic Seas, and the North Atlantic down to approximately 50°N. The horizontal resolution of 1/4° corresponds to ~28 km on a rotated grid with the equator passing through the North Pole. In the vertical, the domain is discretized in 33 levels. The upper ocean spanning from 0 to 200 m is resolved in 10 levels with varying thickness between 10 m (first 5 layers) and ~40 m. The mid-depth ocean between 200 and ~1200 m is resolved in 11 levels with thickness ranging from ~40 m to ~180 m. The deep ocean layer from ~1200 m to ~5000 m is resolved in 12 levels with thickness increasing from ~180 m to ~350 m. The AWL is defined by the constant depth boundaries of 200 m and 1250 m. Vertical mixing in the ocean is parameterized by a K-Profile Parameterization (KPP) scheme (*Large et al.*, 1994) and tracers are advected with an unconditionally stable seventh-

order monotonicity preserving scheme (*Daru and Tenaud, 2004*) that requires no explicit diffusivity.

The ocean model is coupled with a dynamic-thermodynamic sea-ice model (*Losch et al., 2010*). The sea-ice model of the MITgcm uses a viscous-plastic rheology and the so-called zero-layer thermodynamics (i.e., zero heat capacity formulation) (*Semtner, 1976*) with a prescribed ice thickness distribution (ITD) (*Hibler, 1979, 1980, 1984; Castro-Morales et al., 2014*). There are seven ice thickness categories between 0 and a maximum thickness of twice the mean thickness. The distribution of these seven thicknesses is flat, normalized and fixed in time (*Hibler, 1984*) (see also *Castro-Morales et al. (2014)*, their Figure 1). We also use a parameterization for the snow distribution. According to the chosen parameterization, the snow is distributed proportionally to the ice thickness distribution. With this choice, the present configuration is the same as experiment 2 in *Castro-Morales et al. (2014)*, which gives a good agreement with IceSat data (see Figure 8 in *Castro-Morales et al. (2014)*).

The model is forced by realistic atmospheric fields. We use the data of the Coordinate Ocean Research Experiment (CORE) version 2 for the spin-up and the NCEP Climate Forecast System Version 2 for the analyzed simulations. Both data sets include 6 hourly wind, atmospheric temperature and specific humidity, daily downward long and short-radiative fluxes and monthly precipitation field. A monthly climatology of river runoff for the main Arctic rivers follows the AOMIP (Arctic Ocean Model Intercomparison Project) protocol.

The model is spun up from the first day of January 1948 to the last day of December 1978. The spin-up is done with the model in a baseline (control) configuration, i.e., with constant drag coefficients. The subsequent simulations are forced with NCEP reanalysis data from the first day of January 1979 to the last day of December 2010.

4.2.2 Parameterization of Atmospheric and Oceanic Drag Coefficients

In the baseline configuration the sea ice-ocean model runs with constant atmospheric and oceanic drag coefficients ($c_a = 1 \times 10^{-3}$ and $c_w = 5.4 \times 10^{-3}$). In order to have drag coefficients depending on the sea-ice topography, we introduce the deformation energy R as a prognostic variable into the sea-ice model. The deformation energy represents the sea-ice roughness and its evolution equation is presented in *Steiner et al. (1999)*. Deformation energy changes with the work performed by internal forces in the ice E_{int} and with melting M (*Martin, 2007*):

$$\frac{\partial R}{\partial t} = E_{\text{int}} + mRM - \nabla \cdot (\mathbf{u}R), \quad (4.2)$$

where m is a constant ($=1$) and $\nabla \cdot (\mathbf{u}R)$ represents the changes of R due to advection ($\mathbf{u} \cdot \nabla R$) and convergence $R(\nabla \cdot \mathbf{u})$ of ice. The term E_{int} is derived as the scalar product of the stress tensor $\boldsymbol{\sigma}$ and the strain rate tensor $\dot{\boldsymbol{\epsilon}}$ (*Rothrock*, 1975; *Martin*, 2007):

$$E_{\text{int}} = \boldsymbol{\sigma} \cdot \dot{\boldsymbol{\epsilon}} = \sigma_I \varepsilon_I + \sigma_{II} \varepsilon_{II}, \quad (4.3)$$

where

$$\dot{\varepsilon}_I = \dot{\varepsilon}_{11} + \dot{\varepsilon}_{22}, \quad (4.4)$$

$$\dot{\varepsilon}_{II} = \sqrt{(\dot{\varepsilon}_{11} - \dot{\varepsilon}_{22})^2 + 4\dot{\varepsilon}_{12}^2} \quad (4.5)$$

and

$$\sigma_I = \frac{1}{2}(\sigma_{11} + \sigma_{22}), \quad (4.6)$$

$$\sigma_{II} = \sqrt{\eta^2 (\dot{\varepsilon}_{11} - \dot{\varepsilon}_{22})^2 + \eta^2 4\dot{\varepsilon}_{12}^2} \quad (4.7)$$

are the invariants of the tensors $\boldsymbol{\sigma}$ and $\dot{\boldsymbol{\epsilon}}$. This formulation for the deformation energy was already implemented in uncoupled sea-ice models by *Steiner et al.* (1999) and *Martin* (2006, 2007).

The atmospheric and oceanic drag coefficients depend on the deformation energy R and on the ice concentration A . We follow *Steiner* (2001):

$$c_a = m_a R + b_a - 4d_a \left(A - \frac{1}{2}\right)^2 + d_a, \quad (4.8)$$

$$c_w = m_w R + b_w - 4d_w \left(A - \frac{1}{2}\right)^2 + d_w. \quad (4.9)$$

The values of the constants $m_a = 1.9 \times 10^{-9}$, $b_a = 0.8 \times 10^{-3}$, $d_a = 2.6 \times 10^{-3}$, $m_w = 6.0 \times 10^{-8}$, $b_w = 1.2 \times 10^{-3}$ and $d_w = 2.6 \times 10^{-3}$ are taken from *Steiner* (2001). According to Equations 4.8 and 4.9, the drag coefficients increase linearly with the deformation energy. The second contribution to the coefficients varies in conjunction with the ice concentration. It has a maximum for $A = 0.5$ and it is zero for $A = 0$ and $A = 1$ (see also Figure 1 in *Steiner* (2001)).

In our configuration, the deformation energy as a variable does not affect the sea ice or the ocean directly. This means that we do not redistribute the ice in thickness categories according to variations of deformation energy. The only feedback in the physics of the model is then through the atmospheric and oceanic drag coefficients

that enter the momentum equation of the sea ice and of the ocean.

4.3 Results

In this section we show results for climatologies obtained from the first day of January 1990 to the last day of December 2010. The first ten years of the simulations are not used because during this time the model adapts to the new forcing and to the new physics. We focus our analysis on the months of March (maximum sea-ice extent) and September (minimum sea-ice extent). We present (except when stated) climatology maps for the control run (CTRL), for the run with variable drag coefficients (DRAGS) and for differences DRAGS - CTRL. For selected regions and selected variables we also show time series.

In Figure 4.1 we show the September climatology ice concentration for the CTRL run with the regions selected for our analysis.

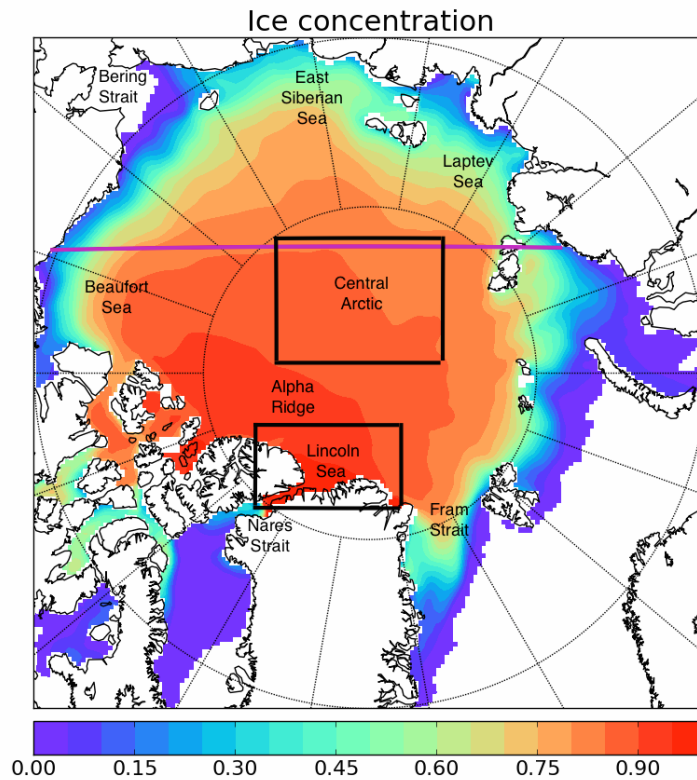


Figure 4.1: Map of the model domain with September climatology for the ice concentration in colors. The two black boxes represents the regions that in this study are referred to as Central Arctic and Lincoln Sea. The purple line represents an oceanographic section in the Beaufort Sea. Other regions of interest for our analysis are also indicated.

4.3.1 Simulated Deformation Energy and Drag Coefficients

In Figure 4.2 we show the deformation energy, the atmospheric drag coefficients and the oceanic drag coefficients. Values for deformation energy in the Arctic basin vary between 20 and 300 KJ/m². Lower values are found toward the marginal sea ice zone while higher values characterize the coastal areas, particularly along the north coast of Greenland in the Lincoln Sea, where the ice is usually pushed against the land and thus is more deformed. In the Central Arctic the values are around 50 to 80 KJ/m². This is in agreement with what is shown in *Steiner et al.* (1999). High values are found also in the northern part of the Canadian Archipelago. In summer, values are everywhere smaller since the deformation energy decreases due to melting. The atmospheric (4.2d-c) and oceanic (4.2e-f) drag coefficients show a pattern similar to the deformation energy, as expected from the linear dependence on the latter. The differences in the spatial pattern are due to the term depending on ice concentration in Equations 4.8 and 4.9. The drag fields agree with those of *Steiner* (2001). Moreover, the spatial pattern also agrees with the results presented in *Tsamados et al.* (2014) even though in their work the empirical formulations for computing the drag coefficients are based on different theoretical concepts and parameterizations. In the Lincoln Sea and along the coast of the Canadian Arctic Archipelago, the drag coefficients are higher in winter (March) than in summer (September). In contrast, the Central Arctic shows higher drag coefficients in summer (mean $c_a = 2.05 \times 10^{-3}$ and mean $c_w = 3.13 \times 10^{-3}$) than in winter (mean $c_a = 1.5 \times 10^{-3}$ and mean $c_w = 3.56 \times 10^{-3}$).

We also analyze the temporal evolution of mean atmospheric drag coefficients in two selected regions: Lincoln Sea and Central Arctic (see black boxes in Figure 4.1). From Figure 4.3 we see that the averaged atmospheric drag coefficients are higher in the Lincoln Sea than in the Central Arctic. Moreover, in the Central Arctic the drag coefficients show almost no trend with the time, while in the Lincoln Sea they clearly decrease over the years. There is also a characteristic interannual pattern, that is a consequence of the interannual changes in ice concentration, but also in deformation energy that depends on ice melting (Equation 4.2). Figures 4.3b and 4.3c also show the temporal variation of the deformation energy and of the ice concentration, which are the variables the drag coefficients depend on. Obviously, both the systematic difference in drag coefficients between the two regions and the decrease over time in the Lincoln Sea can be traced back to the deformation energy. The ice concentration in summer is closer to 50% for the Central Arctic, thus its contribution to the drag coefficients is higher than in the Lincoln Sea.

Finally, we compare our results with atmospheric drag coefficients calculated by applying a parameterization to observed topography data (*Castellani et al.*, 2014). The mean values for the drag coefficients calculated for the Central Arctic and for

the Lincoln Sea (see their Table 2) are plotted in Figure 4.3a. Even though the calculations are based on different assumptions, there is very good agreement for the Central Arctic, but the model tends to underestimate the drag coefficients in the Lincoln Sea.

Table 4.1 contains the minimum, maximum, mean and median values for the simulated drag coefficients. The atmospheric drag coefficients vary between 0.8×10^{-3} and 8×10^{-3} , while the oceanic drag coefficients between 1.2×10^{-3} and 25×10^{-3} . Thus they both fall in the range of measured values. The drag coefficients used in the CTRL run fall into the range of the simulated drag coefficients thus comparing the two runs is reasonable. In Section 4.4.1 we will discuss the use of mean or median values of the drag coefficients for the CTRL run.

Table 4.1: Values of drag coefficients (multiplied by 10^3) obtained with the DRAGS run. The mean, median, minimum and maximum are calculated from the climatological year.

	min	max	mean	median	CTRL
c_a	0.8	8	1.6	1.5	1
c_w	1.2	25	3.5	3.1	5.4

4.3.2 Sea Ice

Figure 4.4 shows the differences DRAGS - CTRL in ice concentration, thickness and drift for March and for September. Differences in ice concentration are generally larger in summer than winter. In summer, the ice concentration is reduced in large part of the Arctic basin when we introduce variable drag coefficients, except for the region north of the Canadian Archipelago. Large differences are found along the north-east coast of Greenland and close to the Siberian Sea and Laptev Sea. While in the above mentioned regions the ice concentration is strongly reduced, in the marginal ice zone (MIZ) the concentration is higher in DRAGS than CTRL. This holds for the Nordic Seas, for the region south of the Fram Strait and south of the Bering Strait, thus we have a larger sea-ice extent in DRAGS than in CTRL.

The ice thickness shows differences in both March and September. The pattern is very similar to the ice concentration: Thinner ice in the Central Arctic and thicker in the MIZ. Particular features are visible in March in the Chukchi sea, where there is a large accumulation of ice in DRAGS compared to CTRL, in the Lincoln Sea with a vary large reduction of ice (larger than 1 m) in both seasons, and in the Canadian Archipelago. In both summer and winter the DRAGS run shows very large thickness in the Nares Strait (up to more than 10 m). This will be further discussed in Section 4.4.

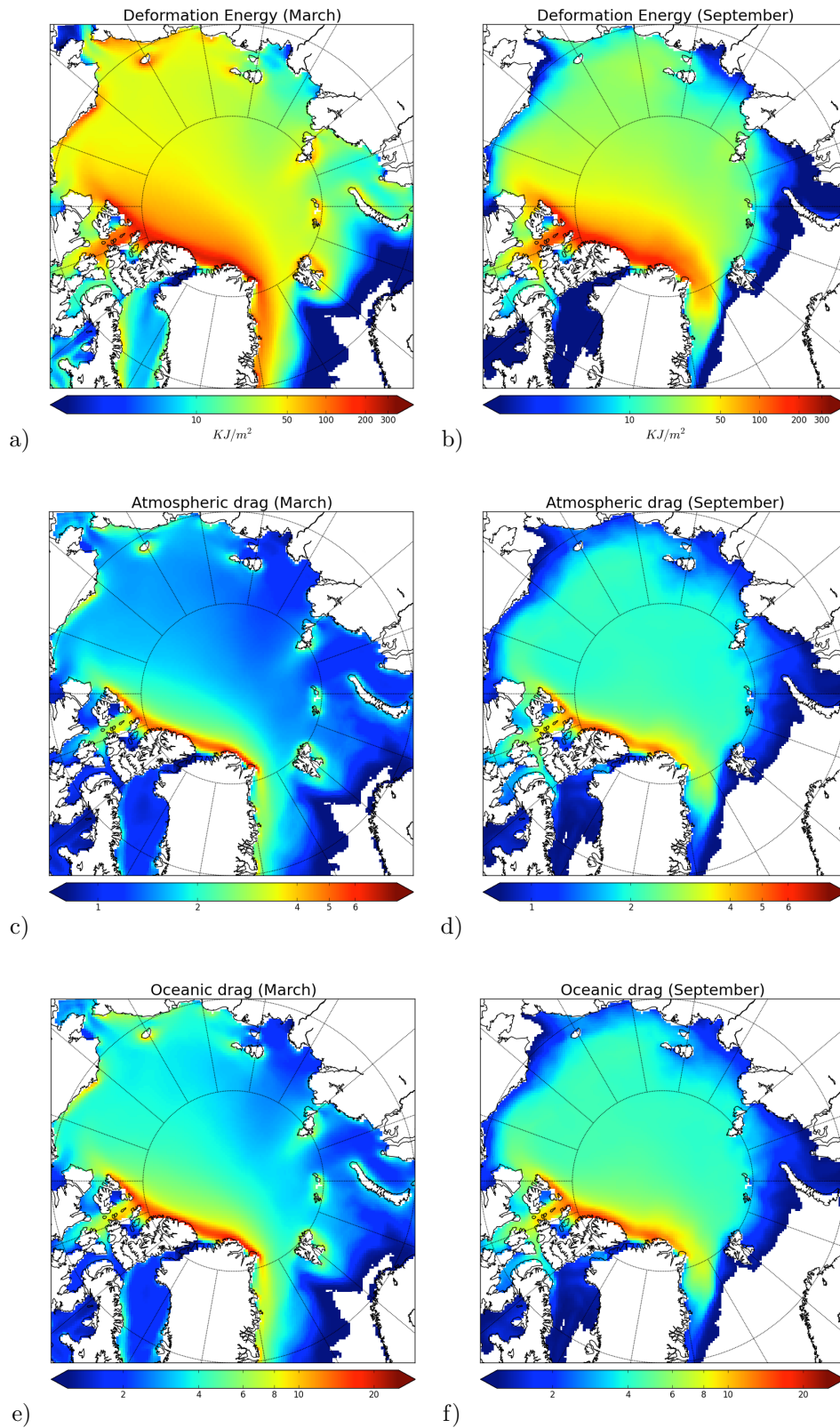


Figure 4.2: March (left column) and September (right column) climatology (1990-2010) for the new prognostic variables implemented in the DRAGS run: deformation energy (a-b), atmospheric drag coefficients (c-d) and oceanic drag coefficients (e-f) scaled by 10^{-3} .

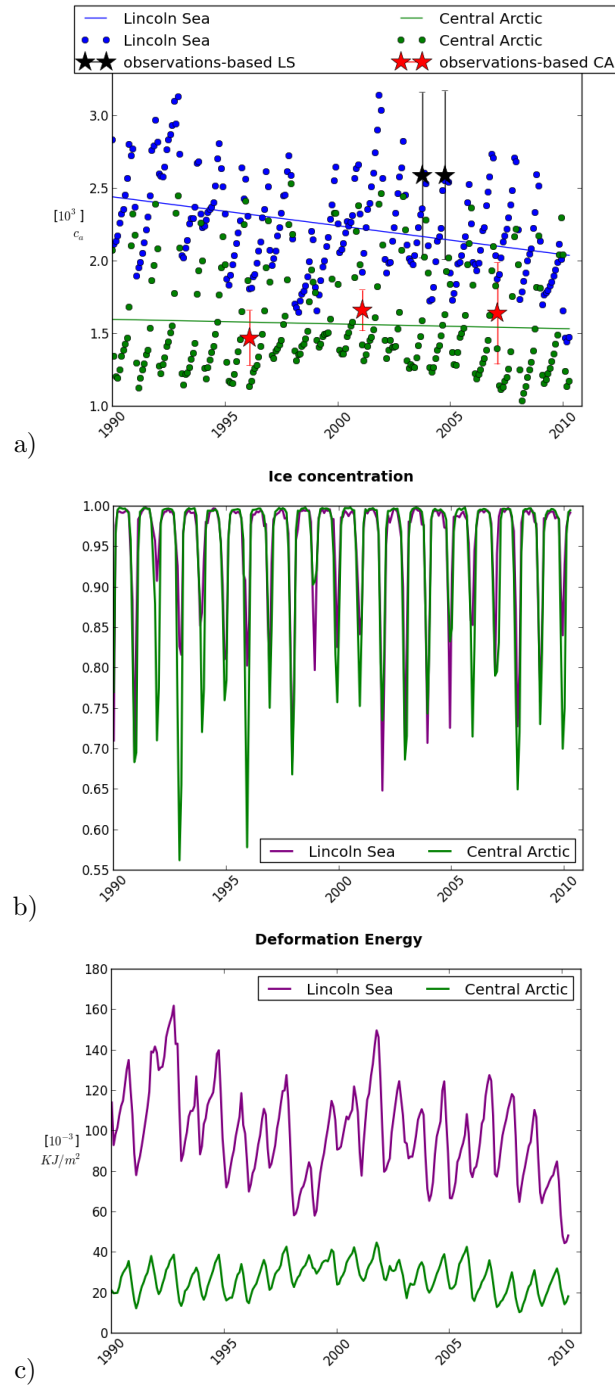


Figure 4.3: Monthly means of atmospheric drag coefficients (a) over the period 1990-2010 for two selected regions (see also the map in figure 4.1): Central Arctic (green) and Lincoln Sea (blue). The stars represent the values taken from Table 2 of *Castellani et al.* (2014) for the Central Arctic (red) and the Lincoln Sea (black) together with the standard deviations. Monthly means of ice concentration (b) and of deformation energy (c) for the same two regions.

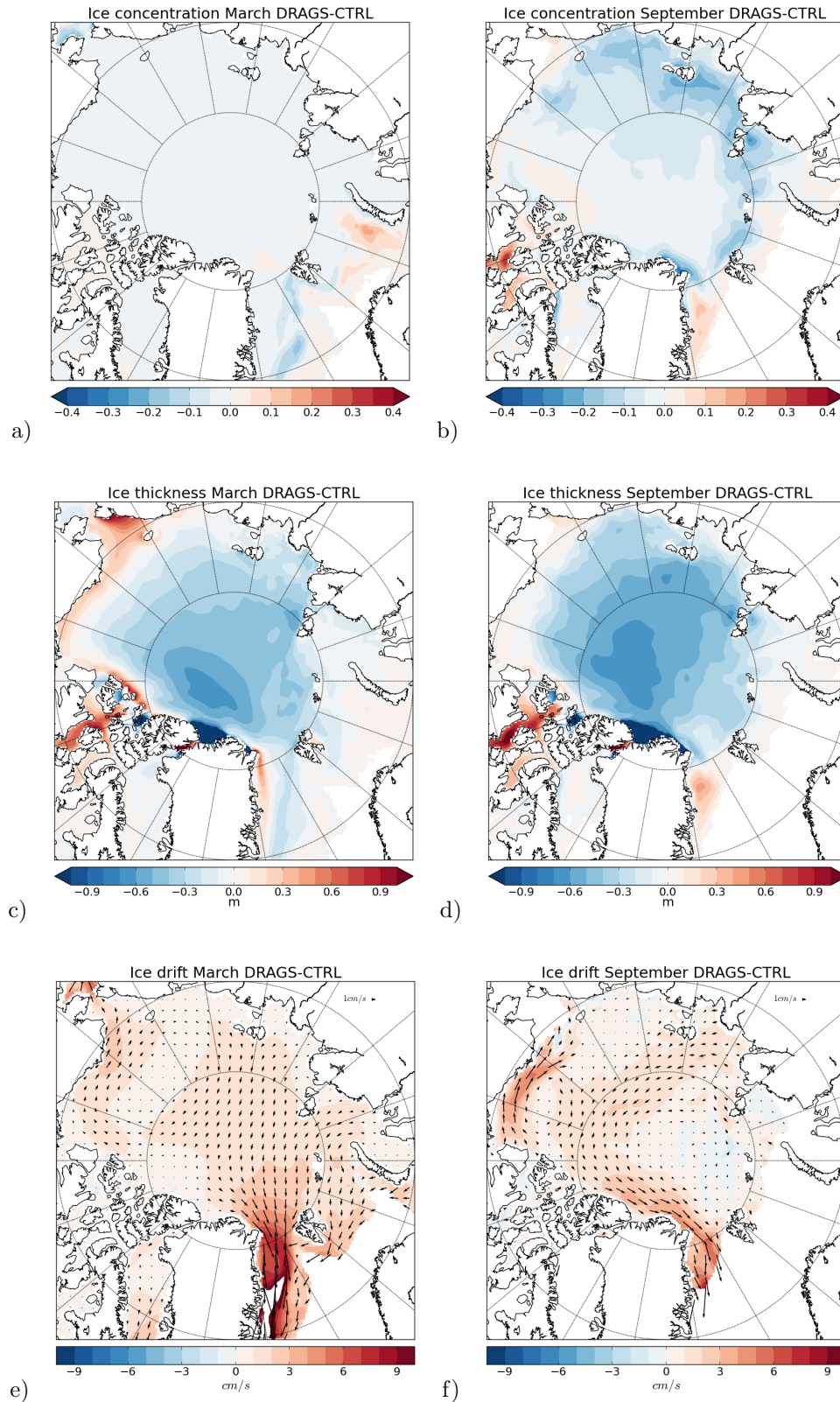


Figure 4.4: Differences DRAGS - CTRL for March (left column) and September (right column) in climatologies for Ice concentration (a-b), thickness (c-d) and drift (e-f).

There are important differences also in the sea-ice drift: In both seasons the ice in the DRAGS run moves faster, because the drag coefficients are generally larger. The Beaufort Gyre is enhanced, mostly in summer, with consequently a larger export through the Bering Strait. Also the flow from North Greenland southward through the Fram Strait is stronger in DRAGS than in CTRL. The arrows show clearly the anticyclonic pattern in March (Figure 4.4e) that dominates during winter, and the cyclonic pattern (Figure 4.4f) that usually dominates in summer. Thus, not only the ice moves faster in DRAGS, but the whole typical ice drift pattern is enhanced.

4.3.3 Ocean

In order to evaluate the effects of the new drag formulation on the ocean, we analyze mixed layer depth, the stream function, vertical velocity and the AWL circulation. The reasons for this choice of variables are the following. According to the KPP parameterization, changes in the intensity of the surface stress would result in a deepening or thinning of the mixed layer. The stream function gives information on the cyclonic or anticyclonic character of the flow. For the stream function we integrate the horizontal velocity field in the entire water column. The velocities used are climatologies for September. The vertical velocity represents the Ekman pumping in the Ocean that is then associated with the large scale ocean transport. For the vertical velocity we choose a depth of 100 m. Finally, the circulation of the AW is evaluated in the entire AWL (between 200 m and 1250 m depth) and in the mid AWL (between 350 m and 800 m depth). The circulation in the AWL gives a connection between changes in the ice and effects on the ocean circulation that can affect then the entire Arctic Basin and the overflow in the Nordic Seas.

More mixing in the DRAGS run leads to a deeper mixed layer. The mixed layer depth (Figure 4.5 a and c) diagnosed following a density criterion (the layer thickness is only 10 m), in the CTRL run reaches an average depth in the sea ice covered area of $7 \text{ m} \pm 3 \text{ m}$, where the mean and standard deviation are calculated for ice concentration larger than 0.1. The mixed layer in DRAGS has a mean depth of $12 \text{ m} \pm 3 \text{ m}$, thus it is almost 2 standard deviations deeper than in CTRL. Figure 4.5c shows larger differences in the Lincoln Sea and in the Canadian Basin. In these regions the mixed layer can be up to 20 m deep, this means a difference of up to 100% since in that region the CTRL run shows mixed layer depths of about 10 m. Figure 4.5c also shows a higher variability than Figure 4.5a, in the latter the mixed layer depth is constant over a large part of the ice covered Arctic Basin. Thus the DRAGS run shows a deeper mixed layer, but also a larger variability in the entire Arctic Basin. The stream function for the CTRL run (Figure 4.5b) shows the basic pattern with a more or less clear separation between the Eurasian and Canadian Basin. The differences DRAGS - CTRL (Figure 4.5d) point to a stronger Beaufort Gyre in

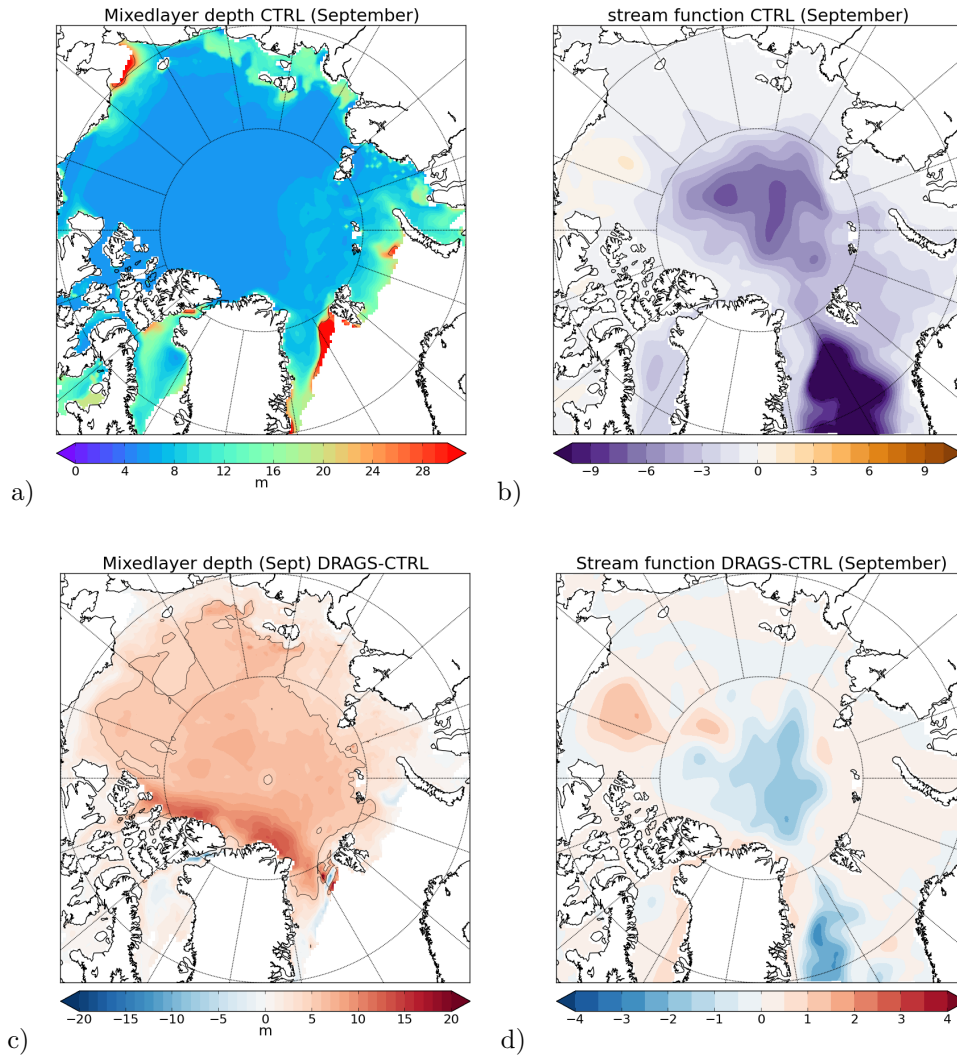


Figure 4.5: September climatologies, for the CTRL run, of mixed layer depth (a) and stream function (b) and differences DRAGS - CTRL for mixed layer depth (c) and stream function (d).

DRAGS in agreement with the ice drift: stronger ice drift leads to an intensified anticyclonic circulation also in the upper ocean layer.

The vertical velocity in Figure 4.6, even though contaminated by many small scale features in the Arctic Basin, shows a clear pattern in the Canadian Basin, mostly in September (see Figure 4.6b and Figure 4.6d, black box): The velocity is downward (violet color, the direction of the z-axis is positive upward) in the central Beaufort Sea and upward along the coast of Alaska. This pattern of upwelling-downwelling is stronger in September than March for both runs and it is stronger for the DRAGS run than for the CTRL run (Figures 4.6d). In DRAGS, a stronger downwelling in the center Beaufort Sea is compensated by a stronger upwelling along the continental slope. This will lead to more Ekman transport in the ocean interior.

Finally, we compare the AW circulation (Figure 4.7) in its intensity and direction for the two runs. We compare again only a climatological September. In Figure 4.7a-c-e we show the AW circulation in the entire AWL (200 m - 1200 m depth) while in Figure 4.7b-d-f we present the AW circulation in the mid AWL (350 m - 800 m depth). The CTRL run shows the typical pattern as inferred from observations and model results (*Karcher et al.*, 2011). This pattern is stronger for the mid AWL (Figure 4.7c) than for the full AWL (Figure 4.7a). There is cyclonic circulation in the Beaufort Sea-Canadian Basin and in the Makarov Basin. The inflow from the Fram Strait with a branch of Atlantic water flowing along the continental margins of the Eurasian and Makarov Basin is also represented. Finally the branch of AW is visible that separates from the Alpha Ridge and flows along the continental slope of Greenland to exit through the Fram Strait. The DRAGS run shows the same pattern, but some differences are visible in Figures 4.7e-f. In particular, the cyclonic circulation in the Makarov Basin is reduced (the difference arrows show an anticyclonic pattern) in both the mid AWL and full AWL. Also in the Canadian Archipelago, even though the differences are small, we see a weaker cyclonic flow in DRAGS than in CTRL. This difference is stronger in the full AWL than in the mid AWL.

4.4 Discussion

The sea ice in DRAGS is affected by the variable drag coefficients in its thickness and also in its area. The thickness distribution obtained is realistic in the entire Arctic Basin. A very high and unrealistic thickness (up to more than 10 m) is reached in the Nares Strait. Here the ice gets stuck and accumulates without the possibility to flow through the Strait. The parameter responsible for this is the sea-ice strength P . In both runs we use the formula for P introduced by *Hibler* (1979) for the viscous-plastic rheology:

$$P = P^* h e^{-C^*(1-A)}, \quad (4.10)$$

where h is the effective ice thickness, A is the ice concentration, P^* and C^* are sea-ice strength parameters that are empirical constants. In the present model configuration we set P^* equal to 27500 N/m² (see e.g., *Itkin et al.* (2014); *Sumata et al.* (2013); *Juricke et al.* (2013) for other possible values). Clearly, the value for P is high enough to prevent the ice to flow through small channels and straits. We tested this hypothesis by running a simulation with a lower value of P^* equal to 15000 N/m² as in *Itkin et al.* (2014). With a lower P^* the ice does not accumulate anymore in the Nares Strait. Thus, a solution could be to select a proper set of parameters that gives the best agreement to real observations when variable drag coefficients are used.

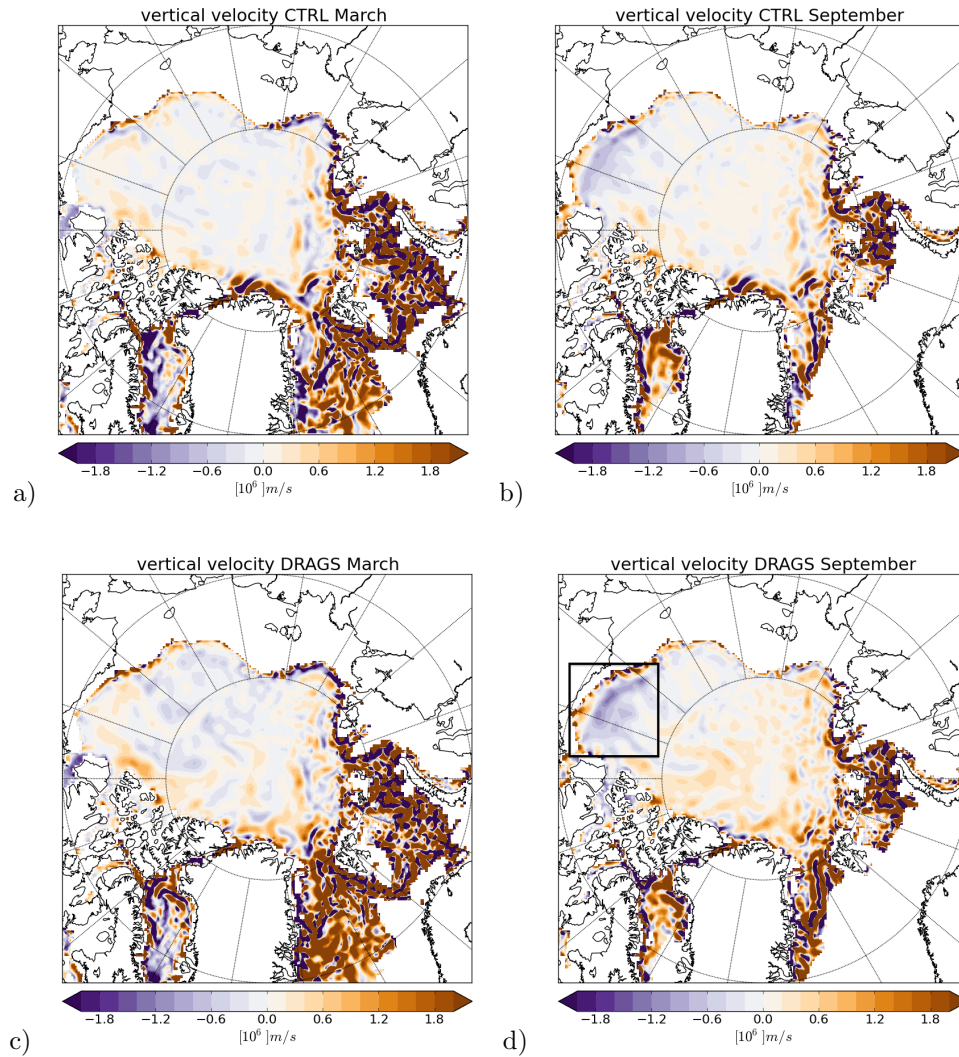


Figure 4.6: March (left column) and September (right column) climatologies of vertical velocities at 100 m depth for the CTRL run (a-b) and for the DRAGS run (c-d). The black box (d) encloses the Beaufort Sea, region where we see a strong upwelling-downwelling pattern.

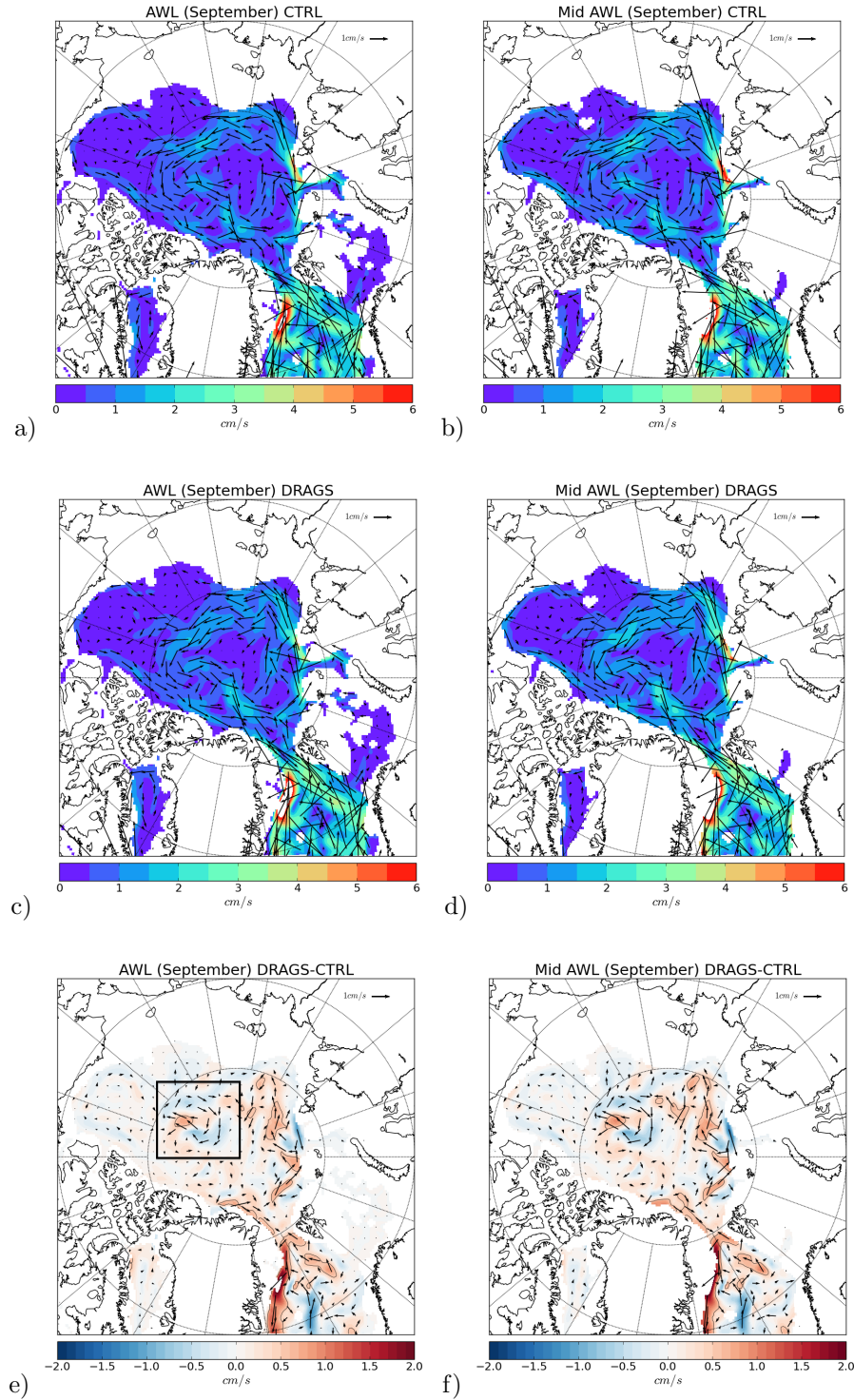


Figure 4.7: September climatology of Atlantic Water circulation in the entire AWL layer, i.e. between 200 m and 1250 m depth (left column) and for the inner part between 350 m and 800 m (right column). The climatologies are for the CTRL run (a-b), for the DRAGS run (c-d) and for the difference DRAGS-CTRL.

A physically more satisfying approach would be to find a new expression for the ice strength as function of the implemented deformation energy. We use the deformation energy to calculate the drag coefficients, we could also find an expression for the strength of the ice that depends on the deformation energy.

Other differences can be explained by differences in the sea-ice drift: the enhanced Beaufort Gyre is responsible for the increased thickness in the Canadian Basin and in the Bering Strait in March. On the other hand, the TPD is also stronger and more ice is transported away from the north coast of Greenland through the Fram Strait. This explains the reduction in thickness in the Lincoln Sea and along the north coast of Greenland, as well as the increase in thickness in the MIZ. We also analyze the effects on the Fram Strait export. Figure 4.8 shows that in DRAGS the variability is enhanced over CTRL and in general the export is larger. Since the Fram Strait export has a strong link with the fresh water export, we expect consequences for the Atlantic Ocean circulation and salinity budget.

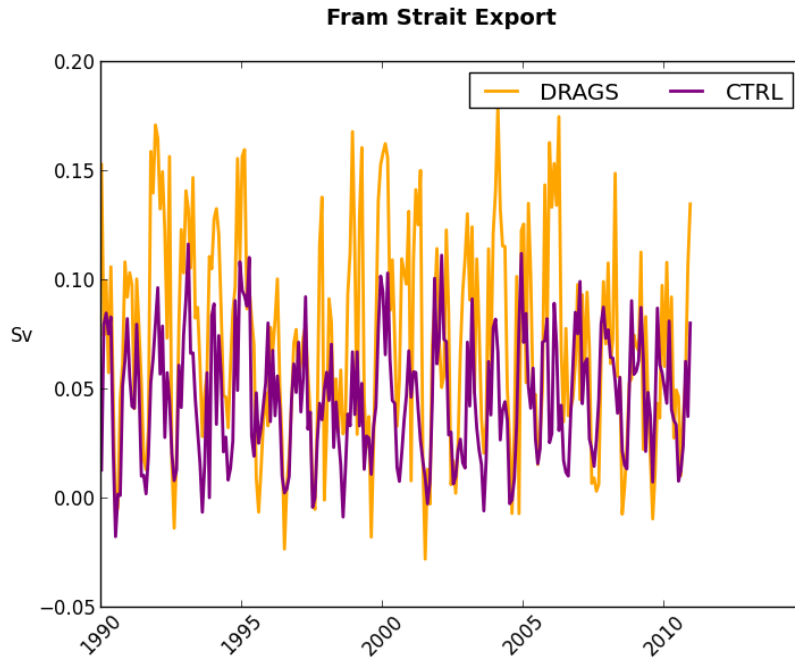


Figure 4.8: Monthly means of Fram Strait export for CTRL and DRAGS over the period 1990-2010.

The increase in the sea-ice drift is visible in the entire Arctic Basin. Even though it is plausible that higher atmospheric drag coefficients lead to faster ice pack, we stress that in many regions the oceanic drag coefficients are also much higher than in the CTRL run. One could have expected a balance, but clearly the atmospheric drag coefficients dominate the drift of the ice. Later, we discuss differences with a run with constant, but higher atmospheric drag coefficients.

The response of the ocean to the new parameterization of surface stress can be seen

not only in the surface, but also in the interior of the ocean. The mixed layer depth obtained with the new parameterization shows much larger variability. Accurate mixed layer depth representations are particularly important when biogeochemical model is coupled to the GCM.

The pattern of upwelling/downwelling in the Beaufort and Chukchi seas is also enhanced. As it was shown by *Yang* (2009), this pattern is associated with the offshore Ekman transport driven by easterly stress which the anticyclonic wind and ice velocity exert on the ocean. The upwelling is weaker in March than in September since in spring the wind and ice velocities are typically weak. Thus, the stronger anticyclonic pattern in the ice drift in DRAGS results in a stronger upwelling/downwelling in the Beaufort Sea. The seasonal cycle of Ekman transport is related with changes in salinity (*Yang and Comiso*, 2007). The Ekman pumping plays a key role in determining the changes in the depth of the 34 isohaline (*Rabe et al.*, 2011). The position of the 34-isohaline has an influence on the Liquid Fresh Water (LFW) content of the Arctic Ocean that has a direct impact on climate (*Häkkinen*, 1999; *Haak et al.*, 2003). Thus stronger Ekman pumping in the interior Beaufort Gyre leads to a depression of the halocline which then impacts the AWL circulation. In Figure 4.9, the position of the 34 isohaline in a cross section passing through the Beaufort Sea (see Figure 4.1) is deeper in the DRAGS run than in the CTRL run. A deeper 34 isohaline in the center of the Beaufort Sea leads to a stronger gradient along the coast and thus to a stronger anticyclonic flow in the ocean interior.

A stronger Beaufort Gyre causes a weaker AWL (*Karcher et al.*, 2011). The reason is that the Beaufort Gyre is very deep and the upper density interval of the AWL responds with large depression in the center of the gyre. Because of this depression, the upper AWL flows with the same sense of rotation and no counter current can establish. In the present case we still see the cyclonic circulation of the AW, but it is weaker in DRAGS than in CTRL.

4.4.1 Sensitivity to Different Constant Drag Coefficients

Can we arrive at the same effect of faster ice with a run using still constant, but larger, drag coefficients? To test this, we choose the mean and median values of drag coefficients from Table 4.1. With such a choice we expect faster ice as a result of the higher atmospheric drag coefficients (1.6×10^{-3} and 1.5×10^{-3} compared to 1×10^{-3}) and of the lower oceanic one (3.5×10^{-3} and 3.1×10^{-3} compared to 5.4×10^{-3}). We compare two additional runs performed with constant mean drag coefficients (MEAN) and with constant median drag coefficients (MEDIAN) and we compare some of the fields with the DRAGS run to see if the differences between DRAGS and CTRL still hold. In Figure 4.10 we show differences DRAGS-MEAN and DRAGS-MEDIAN for ice concentration, thickness and drift.

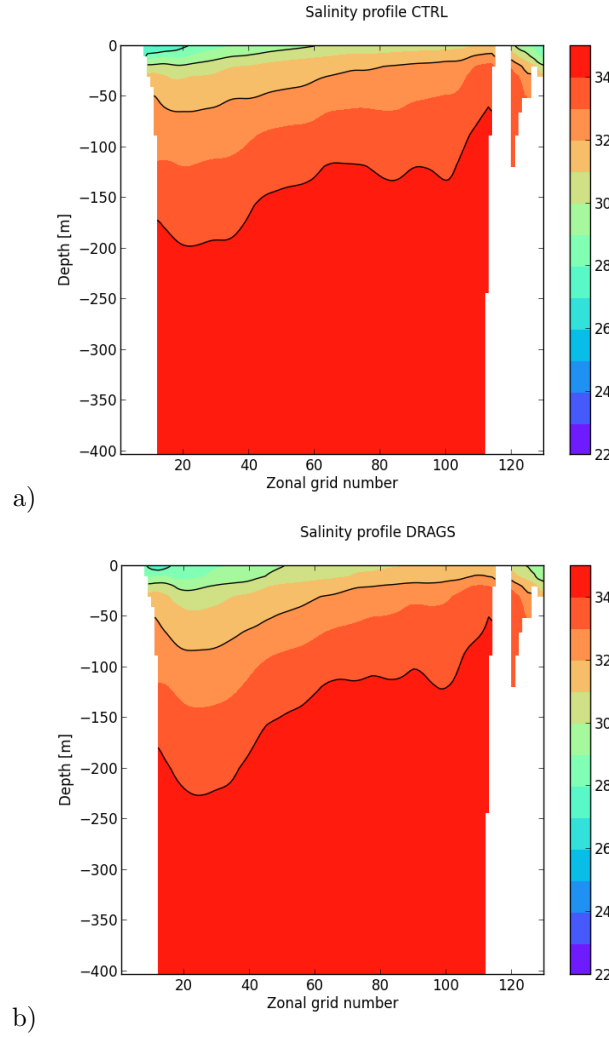


Figure 4.9: Salinity profile over a section crossing the Beaufort Sea (see figure 4.1). September climatologies for the CTRL run (a) and for the DRAGS run (b). The Beaufort Sea extends over the zonal grid number 1 to 40.

The differences DRAGS - MEAN and DRAGS - MEDIAN are very similar compared to each other, but the patterns are different compared to the DRAGS-CTRL comparison (Figure 4.4). The ice concentration and thickness are not reduced as much in the Arctic Basin as for DRAGS-CTRL, but we do not see anymore the large reduction of ice concentration and thickness. There is actually more and thicker ice in DRAGS than in MEAN and MEDIAN. On the other hand, the large reduction of ice along the coast of Greenland also appears in Figure 4.10, as well as the ice accumulation in the Nares Strait.

The constant but different drag coefficients also lead to a different ice drift difference pattern. On one hand we still see the enhanced transport of ice from the Lincoln sea towards the Fram Strait, this mechanism is responsible for the ice reduction along Greenland. On the other hand the direction of the arrows in the Beaufort Sea shows

that the Beaufort Gyre is weaker in DRAGS than in MEAN and MEDIAN.

4.5 Summary and Conclusion

Atmospheric and oceanic drag coefficients that vary in time and space affect the simulations of a coupled sea ice-ocean model. In our approach, we compare two simulations: a simulation with constant drag coefficients (CTRL) and a simulation where the drag coefficients are parameterized as a function of ice concentration and deformation (DRAGS). The model used in this study does not have any explicit parameterizations for topographic features (such as ridges and melt ponds) that modify the sea-ice surface and thus affect the momentum transfer, but the simple parameterization that we implemented, based on the degree of deformation and on the ice concentration, leads to the same patterns as the ones obtained with more sophisticated sea-ice models (*Tsamados et al.*, 2014). Drag coefficients in our simulation fall into the range of calculated and measured values from other sources and the observed variability is also represented accurately.

The dynamic sea-ice variables are strongly affected by the implemented parameterizations. In particular, the ice thickness shows differences of more than half meter in the Central Arctic and of more than 1 m in the Lincoln Sea. The thickness distribution points to a weakness in the model rheology that needs to be improved. We suggest that a key point is the expression for the sea-ice strength, P , that should depend also on the degree of deformation. Changes in the sea-ice drift are high: With the implemented parameterization the ice moves faster, and both the Beaufort Gyre and TPD are stronger. The latter causes a larger ice export through the Fram Strait. The implemented parameterization does not have a uniform effect in the Arctic basin, but the impact is larger in the Canadian Basin and largest in the Lincoln sea. This implies that the constants in the parameterizations of such a model require careful calibration against observation, if predictions were intended.

Our study represents the first implementation of a parameterization for surface dependent drag coefficients in a coupled sea ice-ocean model. Not only does this parameterization allow a more physical representation of the sea-ice evolution, but also it makes possible the analysis of its effects on the ocean circulation. The response of the ocean is large, both at the surface and in the AWL (200 to 1200 m). With the new implementation, the surface stresses are higher, though the ocean drag coefficients are smaller, and cause a deeper mixed layer. Higher sea-ice velocities cause a stronger anticyclonic pattern of the Beaufort Gyre in the upper ocean and enhances the TPD. The increase in the anticyclonic pattern of the Beaufort Gyre leads to stronger downwelling-upwelling in the Canadian basin, a deeper halocline, and consequently a slower cyclonic circulation of the AWL.

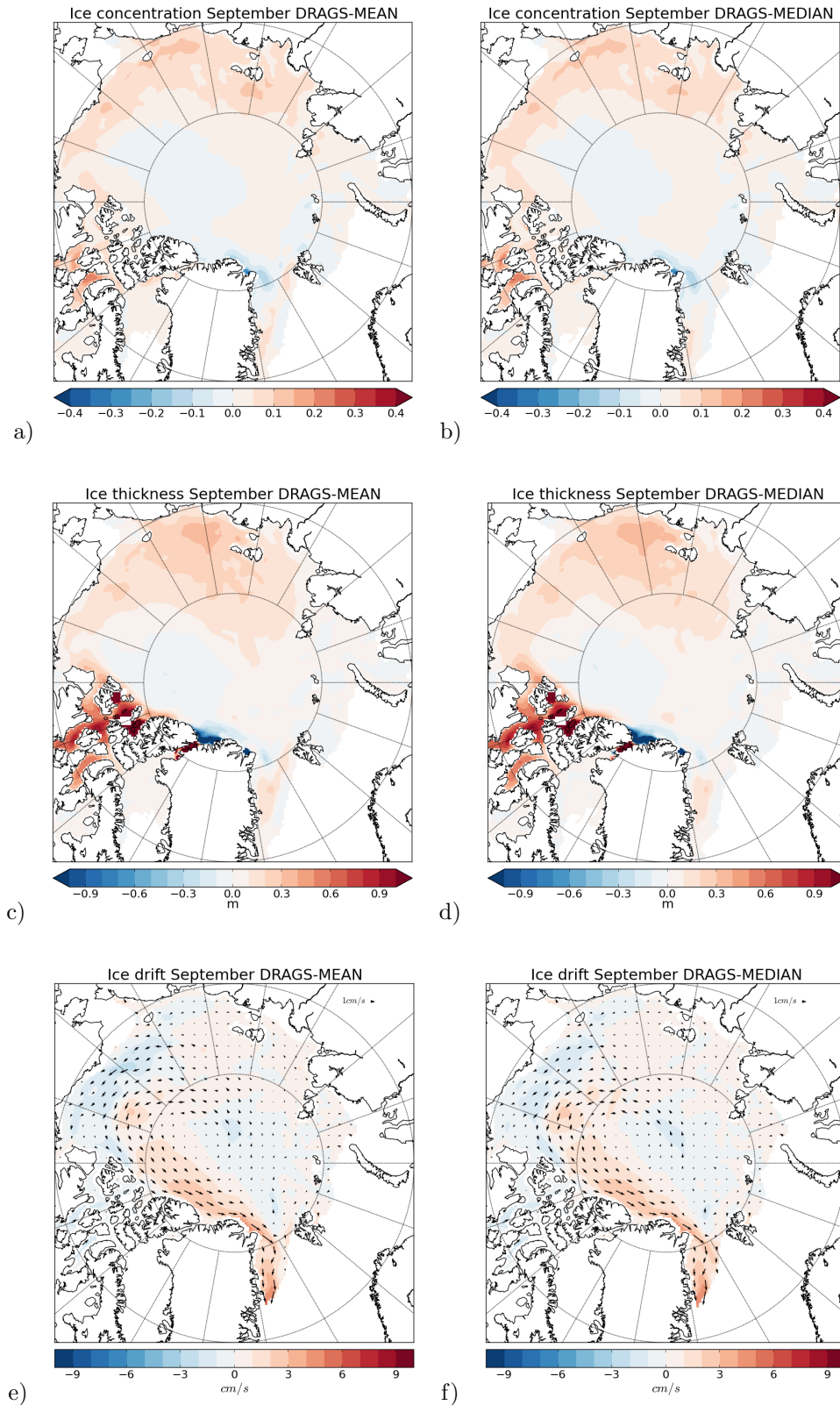


Figure 4.10: Differences in September climatologies for DRAGS-MEAN (left column) and DRAGS-MEDIAN (right column). Differences are computed for ice concentration (a-b), thickness (c-d) and drift (e-f).

Thus, not only the surface layer is affected by the new parameterization, but its effects can be seen also in the ocean interior. In a natural continuation of this study, the effect of our parameterization implementation on the atmosphere and ensuing feedbacks should be studied in a coupled atmosphere-ice-ocean model. Finally, in the light of the recent increase in sea-ice drift (*Spreen et al.*, 2011; *Kwok et al.*, 2013), our results maybe even more relevant to the community. Faster ice could lead to changes in the Ocean circulation that would then affect the other seas.

Acknowledgments

We are thankful to Michael Karcher, Frank Kauker, Hiroshi Sumata and Kathirn Riemann-Campe for the interesting discussions that helped to understand and improve the results.

Chapter 5

Conclusion

In the light of the recent changes affecting the Arctic region, a good understanding of the mechanisms determining the life, movement and evolution of sea ice is becoming necessary. The present PhD thesis focused on the investigation of the atmosphere-ice-ocean dynamic coupling, particularly on understanding how this coupling is affected by the surface roughness of the ice and how the sea-ice topographic features affect ultimately the Arctic Ocean circulation. Air-ice-ocean interactions depend strongly on drag coefficients; however, up to date, no Arctic wide observations are available and very few data exist to link the drag coefficients to sea-ice topography. Thus, in this work we calculated atmospheric and oceanic drag coefficients by applying existing parameterizations to topography profiles used to analyze the surface roughness of the ice. The results based on the topography data are validated and upscaled by numerical simulations. The numerical simulations also allowed us to investigate the ice-ocean feedback mechanisms.

The sea-ice topography data were used to estimate the concentration and height of topographic features in many key regions of the Arctic (e.g., the Lincoln Sea, Beaufort Sea, Central Arctic, Fram Strait, Laptev Sea). Such analysis revealed that different regions are characterized by different topographic elements. In general, the characteristics of the topography roughly follow the ice thickness distribution. Namely, in the Lincoln Sea, a region subject to high deformation events, it is common to find a high concentration of large obstacles (i.e., pressure ridges). In other regions, such as the Central Arctic where the ice is younger and thinner, the large pressure ridges are scarce and the ice field is generally characterized by smaller topographic elements with heights of about 40–50 cm. Nevertheless, each region presents differences due to the age of ice and to weather conditions and large variability is found not only on a spatial scale, but also in time. In particular, we saw a year-to-year variability due to weather conditions in e.g., the Laptev Sea. Moreover, we found that in the Central Arctic the large pressure ridges decreased over the period 1996-2011, together with an increase in small topographic elements. This is associated with a shift from a

prevalent Multiyear Ice regime to a prevalent First Year Ice.

Regarding the atmospheric drag coefficients, we obtained for the first time values over most of the Arctic domain. As for the topographic features, the atmospheric drag coefficients show a large variability and this points to the importance of considering such variability in numerical models. The calculated drag coefficients are in the range of those found from direct turbulence measurements described previously in literature. It is shown here that the drag coefficients are more affected by the separation between obstacles (i.e., by their concentration) than by their height, since the range of variation of the mean separation is one order of magnitude higher than the range of variation of the height. As a result of this study, we can assign mean values of atmospheric drag coefficients to different regions. We found that the atmospheric drag coefficients are systematically higher in regions characterized by large deformation events, such as the Lincoln Sea and along the coast of Greenland. Based on the topography data, we also investigated which topographic elements are more important for the atmospheric drag coefficients. We found that the impact of large pressure ridges on the drag coefficients is relevant only in regions characterized by high deformation, such as the Lincoln Sea. In other regions, such as the Central Arctic, the impact of small topographic elements is much higher and dominates the drag. Thus, one of the main conclusion of this work is that the consideration of only large topographic features, such as pressure ridges, is not enough to characterize the deformation degree of an ice field. This shows that the determination of drag coefficients is a large challenge since it is more difficult to measure or to numerically model the small topographic elements than the large pressure ridges.

Regarding the oceanic drag coefficients, our analysis focused only on the Central Arctic. Here we found a large variability, also within a region, as function of keels depth and concentration. When estimating the Ekman pumping, we found that the variation in upper ocean vertical velocity due to variable drag coefficients is at least in the same order of magnitude as the variations due to changes in the surface velocities of the ice. Such result points to the importance of considering variable oceanic drag coefficients when estimating the momentum transfer between ice and ocean in numerical models.

The results regarding atmospheric and oceanic drag coefficients based on real topography data were validated and upscaled by using numerical simulations. We implemented a parameterization for atmospheric and oceanic drag coefficients as a function of sea-ice roughness and concentration in an Arctic domain coupled ocean-sea ice numerical model. The values of simulated oceanic and atmospheric drag coefficients in different regions of the Arctic show the same variability and agree well with the values calculated on the basis on topography data.

This model study also allowed us to evaluate the effects on the modeled ice and ocean

when we use variable drag coefficients. The large scale sea-ice variables, i.e., sea-ice concentration, thickness and drift, are strongly affected by the introduction of the new parameterization. In particular, the ice moves faster than in the simulation with constant drag coefficients and it shows an enhanced Beaufort Gyre and Transpolar Drift. The impact of the introduced parameterization is not the same for the entire Arctic. We see large changes in sea-ice thickness in the Lincoln Sea, where the calculated drag coefficients show the largest difference compared to the value used in the control simulation.

The ocean is also affected by the introduction of variable drag coefficients. In this simulation the mixed layer becomes deeper than in a control simulation with constant drag coefficients. Moreover, the depth of the mixed layer in the ice covered regions shows higher variability. The surface ocean circulation reflects the changes seen in the sea-ice drift, i.e., a stronger anticyclonic circulation in the Beaufort Sea and an enhanced Transpolar Drift.

Changes of the ocean circulation are seen also in the Atlantic Water Layer. The enhanced anticyclonic surface circulation as a response to the Beaufort Gyre leads to a stronger downwelling in the Beaufort Sea which slows down the cyclonic pattern of the Atlantic Water circulation in this region. This also suggests that the recently observed increase in sea-ice drift speed documented in other studies will not only affect the sea-ice movement and export, but might also have consequences for the inflow and outflow of Atlantic water.

5.1 Outlook

As a follow up of the analysis performed in this PhD work, we present some key points that need further investigation. By analyzing the sea ice topography, we found that the small topographic elements play an important role in both shaping the sea ice surface and affecting the momentum transfer. In the present work, we could not evaluate the effect on the drag coefficients due to the presence of melt ponds. Nevertheless, it has been shown that the melt ponds change the topography of the ice and increase the atmospheric drag due to the effect created by the pond edges (*Von Saldern et al.*, 2006; *Lüpkes et al.*, 2012, 2013). Recently, the methods for estimating the distribution of melt ponds have been substantially improved, by using both satellite and airborne photography (*Markus et al.*, 2003; *Rösel et al.*, 2012). Thus, a further step in the analysis performed here would be to analyze the melt pond cover, its changes in time and space and its impact on the atmospheric drag.

By conducting simulations with variable oceanic and atmospheric drag coefficients we found that both sea ice and ocean are largely affected. A further step in this

direction would be to introduce such parameterization in a coupled atmosphere-ice-ocean model to assess the effects on the atmosphere. Moreover, we found that the ice drift is affected by the variable drag coefficients. Thus, in the line of understanding the mechanisms driving the drift-speed increase that was recently observed, numerical simulations with variable drag coefficients should be used. Before doing this, an accurate validation of the model with observations is required.

This investigation also helped to find a weakness in the parameterization of the sea-ice strength. Currently, the sea-ice strength is parameterized as a function of ice thickness. We argue here that the ice strength should also depend on the deformation degree of an ice field, since more deformed ice is harder than ice that, despite having the same thickness, was subject to only thermodynamic growth. Based on the results presented in Paper III of this work, we propose an expression for the sea ice strength (P) based on former works by *Steiner et al.* (1999) and *Rothrock* (1975). In particular, we can express the potential energy (E_{pot}) of the ice as a function of the deformation energy (R) (*Steiner et al.*, 1999):

$$E_{\text{pot}} = c_R R, \quad (5.1)$$

where c_R is a constant. Moreover, we can relate the potential energy to the thickness h and thickness distribution $g(h)$ according to *Rothrock* (1975):

$$E_{\text{pot}} = c_p \int_0^{\infty} h^2 g(h) dh, \quad (5.2)$$

where c_p depends on the density of water and air (see *Rothrock* (1975) for details). If we equate Equation 5.1 and 5.2 and we apply the total derivative we obtain:

$$c_p \int_0^{\infty} h^2 \frac{D}{Dt} g(h) dh = c_R \frac{D}{Dt} R \quad (5.3)$$

According to *Rothrock* (1975), the derivative of the ice thickness distribution is:

$$\frac{D}{Dt} g(h) = -g(\nabla \cdot \mathbf{u}) - \frac{\partial}{\partial t}(fg) + \psi \quad (5.4)$$

where \mathbf{u} is the ice velocity, f is a thermodynamic growth source and ψ a redistribution function that describes how the ice is redistributed over thickness categories. The evolution equation for the deformation energy is presented in Paper III. By assuming that the thermodynamic terms in the deformation energy equation and in the thickness distribution function do eliminate each other, we arrive at:

$$-(\nabla \cdot \mathbf{u}) c_p \int_0^\infty h^2 g(h) dh - c_p \int_0^\infty h^2 g(h) \psi dh = c_R E_{\text{int}} - c_R R (\nabla \cdot \mathbf{u}) , \quad (5.5)$$

where E_{int} is the internal work (see Paper III). Finally, by substituting the expression for the strength P found in *Rothrock* (1975):

$$c_p \int_0^\infty h^2 g(h) \psi dh = |\dot{\varepsilon}| \alpha_r P \quad (5.6)$$

and by using relations 5.1 and 5.2 we arrive at:

$$P = \frac{c_R}{|\dot{\varepsilon}| \alpha_r} E_{\text{int}} . \quad (5.7)$$

For a description of the terms in Equation 5.7 see *Rothrock* (1975). As a first step, in the development of Equation 5.7 we did not consider the term that represents the frictional energy loss in ridging (see *Rothrock* (1975), Equation 14). Equation 5.7 has been implemented in the MITgcm in a preliminary stage of testing. Future work will be done to improve this new description of the ice strength.

Bibliography

- Aagaard K., L. K. Coachman and E. C. Carmack (1981) On the halocline of the Arctic Ocean. *Deep Sea Research, Part A: Oceanographic Research Papers*, **28(6)**, pp. 529-545, DOI: 10.1016/0198-0149(81)90115-1.
- Aagaard K. (1982) Inflow from the Atlantic Ocean to the Polar Basin, In: *The Arctic Ocean, the Hydrographic Environment and the Fate of Pollutants*, L. R. Rey and B. Stonehouse (Editors), Wiley Publisher, pp. 69-82. ISBN:9780471874645.
- Aagaard K. (1989) A synthesis of the Arctic Ocean circulation, *Rapp. P.-V. Reun. Cons. Int. Explor. Mar.*, **188**, pp. 11-22.
- AMAP Assessment Report: Arctic Pollution Issues. Arctic Monitoring and Assessment Program (AMAP)*, xii + 859 pp., Oslo, Norway, 1998.
- Anderson, R. J. (1987) Wind stress measurements over rough sea ice during the 1984 Marginal Ice Zone Experiment. *J. Geophys. Res.*, **92(C7)**, pp. 6933-6941, doi:10.1029/JC092iC07p06933.
- Andreas, E. L. (1995) Air-ice coefficients in the western Weddell Sea: 2. A model based on form drag and drifting snow. *J. Geophys. Res.*, **100(C3)**, pp. 4833-4843, doi:10.1029/94JC02016.
- Andreas E. L., T. W. Horst, A. A. Grachev, P. O. G. Persson, C. W. Fairall, P. S. Guest and R. E. Jordan (2010) Parametrizing turbulent exchange over summer sea ice and the marginal ice zone. *Q. J. R. Meteorol. Soc.*, **138**, pp. 927-943, DOI:10.1002/qj.618.
- Andreas, E. L. (2011) A relationship between the aerodynamic and physical roughness of winter sea ice. *Q. J. R. Meteorol. Soc.*, **137**, pp. 1581-1588, doi: 10.1002/qj.842
- Andreas E. L., L. Mahrt and D. Vickers (2012) A new drag relation for aerodynamically rough flow over the ocean. *J. Atmos. Sci.*, **69**, pp. 2520-2537, doi: <http://dx.doi.org/10.1175/JAS-D-11-0312.1>

- Arya, S. P. S. (1973) Contribution of Form Drag on Pressure Ridges to the Air Stress on Arctic Ice. *J. Geophys. Res.*, **78**(30), pp. 7092-7099, doi:10.1029/JC078i030p07092.
- Arya, S. P. S. (1975) A Drag Partitioning Theory for Determining the Large-Scale Roughness Parameter and Wind Stress on the Arctic Pack Ice. *J. Geophys. Res.*, **80**(24), pp. 3447-3454, doi:10.1029/JC080i024p03447.
- Augstein, E. (1997), The Expedition ARCTIC '96 of RV "Polarstern" (ARK XII) with the Arctic Climate System Study (ACSYS). Volume 234 of Berichte zur Polarforschung. Publisher: Alfred-Wegener-Institute für Polar- und Meeresforschung.
- Banke E. G. and S. D. Smith (1975) Measurement of form drag on ice ridges. *AIDJEX Bull.* **28**, 21-27.
- Beszczynska-Möller A., E. Fahrbach, U. Schauer and E. Hansen (2012) Variability in Atlantic water temperature and transport at the entrance to the Arctic Ocean, 1997-2010. *ICES Journal of Marine Science*, doi:10.1093/icesjms/fss056.
- Birnbaum G. and C. Lüpkes (2002) A new parameterization of surface drag in the marginal sea ice zone. *Tellus A*, **54**, pp. 107-123, doi: 10.1034/j.1600-0870.2002.00243.x.
- Brauch J. P. and R. Gerdes (2005) Response of the northern North Atlantic and Arctic oceans to a sudden change of the North Atlantic Oscillation. *J. Geophys. Res.*, **110**, C11018, doi:10.1029/2004JC002436.
- Budëus R. and P. Lemke (2007) The expeditions ARKTIS-XX/1 and ARKTIS-XX/2 of the Research Vessel "Polarstern" in 2004, *Rep. Polar Res.*, **544**, pp. 242. Available at <http://hdl.handle.net/10013/epic.10549>.
- Carmack E. C., R. W. Macdonald, R. G. Perkin, F. A. McLaughlin, and R. J. Pearson (1995) Evidence for warming of Atlantic water in the Southern Canadian Basin of the Arctic Ocean: Results from the Larsen-93 expedition. *Geophys. Res. Lett.*, **22**, 9, pp. 1061-1064, DOI: 10.1029/95GL00808.
- Carmack, E. C. (2000) The Arctic Ocean's freshwater budget: Sources, storage and export, In: *The Freshwater Budget of the Arctic Ocean*, E. L. Lewis (Editor), pp. 91-126, NATO ASI Series 2: Environmental Security, **70**, Kluwer Academic Publishers, Dordrecht, Netherlands, ISBN: 978-0-7923-6440-5.
- Castellani G., C. Lüpkes, S. Hendricks and R. Gerdes (2014) Variability of Arctic sea ice topography and its impact on the atmospheric surface drag. *J. Geophys. Res.*, **119**, pp. 6743-6762, doi:10.1002/2013JC009712.

- Castellani G., R. Gerdes, M. Losch and C. Lüpkes (2015) Impact of sea ice bottom topography on the Ekman pumping. G. Lohmann, H. Meggers, V. Unnithan, D. Wolf-Gladrow, J. Notholt, and A. Bracher (Editors), In: *Towards an interdisciplinary approach in Earth System Science* (Springer Earth System Science), Heidelberg [u.a.], Springer, 251 p., ISBN: 978-3-319-13865-7 . doi: 10.1007/978-3-319-13865-7_16.
- Castro-Morales K., F. Kauker, M. Losch, S. Hendricks, K. Riemann-Campe, and R. Gerdes (2014) Sensitivity of simulated sea ice to realistic ice thickness distributions and snow parameterizations. *J. Geophys. Res.*, **119**, pp. 559-571, doi:10.1002/2013JC009342.
- Comiso, J. C. (2012) Large Decadal Decline of the Arctic Multiyear Ice Cover. *J. Climate*, **25**, pp. 1176-1193, doi: <http://dx.doi.org/10.1175/JCLI-D-11-00113.1>
- Dalå N. S., R. Forsberg, K. Keller, H. Skourup, L. Stenseng and S. M. Hvidegaard (2005) Airborne Lidar Measurements of Sea Ice North of Greenland and Ellesmere Island 2004. *Danish National space Center*, Copenhagen, Technical Report No. 1.
- Daru V. and C. Tenaud (2004) High order one-step monotonicity-preserving schemes for unsteady compressible flow calculations. *J. Comput. Phys.*, **193**, 2, pp. 563-594. doi: 10.1016/j.jcp.2003.08.023.
- Davis N. R. and P. Wadhams (1995) A statistical analysis of Arctic pressure ridge morphology. *J. Geophys. Res.*, **100**, pp. 10915-10925, doi:10.1029/95JC00007.
- Dickson R. R., J. Meincke, S.-A. Malmberg and A. J. Lee (1988) The “Great Salinity Anomaly” in the northern North Atlantic 1968-1982. *Progress in Oceanography*, **20**, 2, Pergamon Press, pp. 103-151, doi:10.1016/0079-6611(88)90049-3.
- Ekman, V. W. (1905) *On the influence of the earth's rotation on ocean currents*. Arkiv för Matematik, Astronomi och Fysic. **2**, no.11, 1-52.
- Fairall C. W. and R. Markson (1987) Mesoscale variations in surface stress, heat fluxes, and drag coefficient in the Marginal Ice Zone During the 1983 Marginal Ice Zone Experiment. *J. Geophys. Res.*, **92**, C7, pp. 6921-6932, doi:10.1029/JC092iC07p06921.
- Fissel D. B., J. R. Marko, and H. Melling (2004) Upward looking ice profiler sonar instruments for ice thickness and topography measurements. *Oceans '04 MTTS/IEEE Techno-Ocean '04*, **3**, pp. 1638-1643, doi:10.1109/OCEANS.2004.1406369.
- Flocco D. and D. L. Feltham (2007) A continuum model of melt pond evolution on Arctic sea ice, *J. Geophys. Res.*, **112**, C08016, doi:10.1029/2006JC003836.

- Flocco D., D. L. Feltham and A. K. Turner (2010) Incorporation of a physically based melt pond scheme into the sea ice component of a climate model. *J. Geophys. Res.*, **115**, C08012, doi:10.1029/2009JC005568.
- Garbrecht T., C. Lüpkes, E. Augstein and C. Wamser (1999) Influence of a sea ice ridge on the low-level air flow. *J. Geophys. Res.*, **104**, D20, pp. 24499-24507, doi:10.1029/1999JD900488.
- Garbrecht T., C. Lüpkes, J. Hartmann and M. Wolff (2002) Atmospheric drag coefficients over sea ice – validation of a parameterisation concept. *Tellus A*, **54**, pp. 205-219, doi: 10.1034/j.1600-0870.2002.01253.x.
- Gerdes R., M. Karcher, C. Köberle, K. Fieg (2008) Simulating the long term variability of liquid freshwater export from the Arctic Ocean, In: *Arctic-Subarctic Ocean Fluxes: Defining the Role of the Northern Seas in Climate*, Dickson R. R., J. Meincke nad P. Rhines (Editors), Springer Netherlands, pp. 405-425, doi: 10.1007/978-1-4020-6774-7_18
- Gray J. M. N. T. and L. W. Morland (1994) A two-Dimensional Model for the Dynamics of Sea Ice. *Phil. Trans. R. Soc. Lond. A*. **347**, pp. 219-290, DOI: 10.1098/rsta.1994.0045.
- Gray J. M. N. T. and P. D. Killworth (1996) Sea Ice Ridging Schemes. *J. Phys. Oc.*, **26**, pp. 2420-2428.
- Guest P. S. and K. L. Davidson (1987) The effect of observed ice conditions on the drag coefficient in the summer East Greenland Sea Marginal Ice Zone. *J. Geophys. Res.*, **92**, C7, pp.6943-6954, doi:10.1029/JC092iC07p06943.
- Guest P. S. and K. L. Davidson (1991) The aerodynamic roughness of different types of sea ice. *J. Geophys. Res.*, **96**, C3, pp.4709-4721, doi:10.1029/90JC02261.
- Haak H., U. Jungclaus, U. Mikolajewicz, and M. Latif (2003) Formation and propagation of great salinity anomalies. *Geophys. Res. Lett.*, **30**, 1473, doi:10.1029/2003GL017065, 9.
- Haas C. and H. Eicken (2001) Interannual variability of summer sea ice thickness in the Siberian and Central Arctic under different atmospheric circulation regimes. *J. Geophys. Res.*, **106**, C3, pp. 4449-4462, doi:10.1029/1999JC000088.
- Haas C. and J. Lieser (2001) Sea ice conditions in the transpolar drift in August/September 2001: Observations during POLARSTERN cruise ARKTIS XVII/2, *Rep. Polar Res.*, **441**, pp. 123. Available at <http://hdl.handle.net/10013/epic.10446>.

- Haas, C. (2004a) Late-summer sea ice thickness variability in the Arctic Transpolar Drift 1991-2001 derived from ground-based electromagnetic sounding. *Geophys. Res. Lett.*, **31**, L09402, doi:10.1029/2003GL019394.
- Haas, C. (2004b) EM ice thickness measurements during GreenICE 2004 field campaign, *Tech. rep.*, EU project GreenICE (EVK2-2001-00280), Alfred Wegener Institute, Bremerhaven, Germany.
- Haas C., S. Hendricks and M. Doble (2006) Comparison of the sea ice thickness distribution in the Lincoln Sea and adjacent Arctic Ocean in 2004 and 2005. *Annals of glaciology*, **44**, pp. 247-252..
- Haas C., A. Pfaffling , S. Hendricks, L. Rabenstein, J.- L. Etienne and I. Rigor (2008) Reduced ice thickness in Arctic Transpolar Drift favors rapid ice retreat. *Geophys. Res. Lett.*, **35**, L17501, doi:10.1029/2008GL034457.
- Haas C., J. Lobach, S. Hendricks, L. Rabenstein and A. Pfaffling (2009) Helicopter-borne measurements of sea ice thickness, using a small and lightweight, digital EM system. *J. Appl. Geophys.*, **67**, pp. 234-241, doi: 10.1016/j.jappgeo.2008.05.005.
- Häkkinen, S. (1993) An Arctic source of the Great Salinity Anomaly: A simulation of the Arctic ice-ocean system for 1955-1975. *J. Geophys. Res.*, **98**, C9, pp. 16397-16410, doi:10.1029/93JC01504.
- Häkkinen, S. (1999) A simulation of the thermohaline effects of a great salinity anomaly. *J. Climate*, **12**, 6, pp. 1781-1795, DOI: 10.1175/1520-0442(1999)012<1781:ASOTEO>2.0.CO;2.
- Hanssen-Bauer I., and Y. T. Gjessing (1988), Observations and model calculations of aerodynamic drag on sea ice in the Fram Strait, *Tellus A*, **40**, pp. 151-161, doi: 10.1111/j.1600-0870.1988.tb00413.x.
- Harder M. and P. Lemke (1994) Modelling the extent of sea ice ridging in the Weddell Sea. In: *The Polar Oceans and Their Role in Shaping the Global Environment, Geophysical Monograph*, O. M. Johannessen, R. D. Muench and J. E. Overland (Editors), American Geophysical Union, Washington, D.C., pp. 373-381, doi: 10.1029/GM085p0187.
- Hartmann J., C. Kottmeier, C. Wamser, and E. Augstein (1994) Aircraft measured atmospheric momentum, heat and radiation fluxes over Arctic sea ice, In: *The Polar Oceans and Their Role in Shaping the Global Environment*, O. M. Johannessen, R. D. Muench and J. E. Overland (Editors), American Geophysical Union, Washington, D.C., pp.443-454, doi: 10.1029/GM085p0443.

- Hibler, W. D. III. (1972) Removal of aircraft altitude variation from laser profiles of the Arctic pack. *Journal of Geophysical Research*, **77**, 36, pp. 7190-7195, doi:10.1029/JC077i036p07190.
- Hibler, W. D. III. (1975) Characterization of cold-regions terrain using airborne laser profilometry. *J. Glaciol.*, **15**, No 73, pp. 329-347.
- Hibler, W. D. III (1979) A dynamic thermodynamic sea ice model. *J. Phys. Oceanogr.*, **9**, pp. 815-846, doi: [http://dx.doi.org/10.1175/1520-0485\(1979\)009<0815:ADTSIM>2.0.CO;2](http://dx.doi.org/10.1175/1520-0485(1979)009<0815:ADTSIM>2.0.CO;2).
- Hibler, W. D. III (1980) Modeling a variable thickness sea ice cover. *Mon. Weather Rev.*, **108**, pp. 1943-1973.
- Hibler, W. D. III (1984) The role of sea ice dynamics in modeling CO₂ increases, In: *Climate Processes and Climate sensitivity*, J. E. Hansen, and T. Takahashi (Editors), American Geophysical Union, Washington, D.C., DOI: 10.1029/GM029p0238.
- Hibler W. D. III and G. M. Flato (1992) Sea Ice Models, In: *Climate System Modeling*, K. E. Trenberth (Editor), pp. 413-436, Cambridge University Press., ISBN: 0521432316.
- Holland D. M., L. A. Mysak and J. M. Oberhuber (1996) An investigation of the general circulation of the Arctic Ocean using an isopycnal model. *Tellus A*, **48**, pp. 138-157, doi: 10.1034/j.1600-0870.1996.00008.x.
- Hunke, E. (2010) Thickness sensitivities in the CICE sea ice model. *Oc. Mod.*, **34**, 3, pp. 137-149.
- Itkin P., M. Karcher and R. Gerdes (2014) Is weaker Arctic sea ice changing the Atlantic water circulation? *J. Geophys. Res.*, **119**, pp. 5992-6009, doi:10.1002/2013JC009633.
- Jakobsson, M. (2002) Hypsometry and volume of the Arctic Ocean and its constituent sea. *Geochem. Geophys. Geosyst.*, **3**, 1, doi:10.1029/2001GC000302.
- Juricke S., P. Lemke, R. Timmermann and T. Rackow (2013) Effects of stochastic ice strength perturbation on Arctic finite element sea ice modeling. *J. Climate*, **26**, pp. 3785-3802, doi: <http://dx.doi.org/10.1175/JCLI-D-12-00388.1>.
- Karcher M. and J. M. O. Oberhuber (2002) Pathways and modification of the upper and intermediate water of the Arctic Ocean. *J. Geophys. Res.*, **107**, C6, doi: 10.1029/2000JC000530.

- Karcher M., R. Gerdes, F. Kauker and C. Köberle (2003) Arctic warming: Evolution and spreading of the 1990s warm event in the Nordic Seas and the Arctic Ocean. *J. Geophys. Res.*, **108**, C2, doi: 10.1029/2001JC001265.
- Karcher M., F. Kauker, R. Gerdes, E. Hunke, and J. Zhang (2007) On the dynamics of the Atlantic Water circulation in the Arctic Ocean. *J. Geophys. Res.*, **112**, C04S02, doi:10.1029/2006JC003630.
- Karcher M., A. Beszczynska-Möller, F. Kauker, R. Gerdes, S. Heyden, B. Rudels, and U. Schauer (2011) Arctic Ocean warming and its consequences for the Denmark Strait overflow. *J. Geophys. Res.*, **116**, C02037, doi:10.1029/2010JC006265.
- Karcher M., J. N. Smith, F. Kauker, R. Gerdes, and W. M. Jr. Smethie (2012) Recent changes in Arctic Ocean circulation revealed by 129-iodine observations and modeling. *J. Geophys. Res.*, **117**, C08007, doi: 10.1029/2011JC007513.
- Ketchum, R. D. Jr. (1971) Airborne laser profiling of the Arctic pack ice. *Remote Sens. Environ.*, **2**, No. 36, pp. 41-52, doi:10.1016/0034-4257(71)90076-9.
- Kottmeier C., J. N. Hartmann and C. Wamser (1994) Radiation and eddy flux experiment 1993 (REFLEX II), Berichte zur Polarforschung (Reports on Polar Research), Bremerhaven, Alfred Wegener Institute for Polar and Marine Research, **133**, 62 p.
- Kovacs A., J. S. Holladay and C. J. Bergeron (1995) The footprint altitude ratio for helicopter electromagnetic sounding of sea-ice thickness: Comparison of theoretical and fields estimates. *Geophysics*, **60**, 2, pp. 374–380. doi:10.1190/1.1443773.
- Köberle C. and R. Gerdes. (2003). Mechanisms Determining the Variability of Arctic Sea Ice Conditions and Export. *Journal of Climate*, **16**, pp. 2843-2858.
- Kurtz N. T., S. L. Farrell, M. Studinger, N. Galin, J. P. Harbeck, R. Lindsay, V. D. Onana, B. Panzer, and J. G. Sonntag (2013) Sea ice thickness, freeboard, and snow depth products from Operation IceBridge airborne data. *The Cryosphere*, **7**, pp. 1035-1056, doi:10.5194/tc-7-1035-2013.
- Kwok R., H. J. Zwally, and D. Yi (2004) ICESat observations of Arctic sea ice: A first look. *Geophys. Res. Lett.*, **31**, L16401. doi:10.1029/2004GL020309.
- Kwok R., and D. A. Rothrock (2009) Decline in Arctic sea ice thickness from submarine and ICESat records: 1958-2008. *Geophys. Res. Lett.*, **36**, L15501, doi:10.1029/2009GL039035.

- Kwok R., G. F. Cunningham, M. Wensnahan, I. Rigor, H. J. Zwally, and D. Yi (2009) Thinning and volume loss of Arctic sea ice: 2003-2008. *J. Geophys. Res.*, **114**, C07005, doi:10.1029/2009JC005312.
- Kwok R., G. Spreen, and S. Pang (2013) Arctic sea ice circulation and drift speed: Decadal trends and ocean currents. *J. Geophys. Res.*, **118**, pp. 2408-2425, doi:10.1002/jgrc.20191.
- Large W. G., J. C. McWilliams, and S. C. Doney (1994) Ocean vertical mixing: A review and a model with a nonlocal boundary layer parameterization. *Rev. Geophys.*, **32**, 4, pp. 363-403, doi:10.1029/94RG01872.
- Laxon S. W., K. A. Giles, A. L. Ridout, D. J. Wingham, R. Willatt, R. Cullen, R. Kwok, A. Schweiger, J. Zhang, C. Haas, S. Hendricks, R. Krishfield, N. Kurtz, S. Farrell, and M. Davidson (2013) CryoSat-2 estimates of Arctic sea ice thickness and volume. *Geophys. Res. Lett.*, **40**, pp. 732-737, doi:10.1002/grl.50193.
- Lensu M., B. Cheng and L. Axell (2003) The first implementation of ridging to the sea ice forecast models of FIMR and SMHI, *EU Project IRIS (EVK3-CT-2002-00083), Deliverable D10, Part 1, Internal report*, Helsinki University of Technology, Ship Laboratory, Helsinki, Finland, 2003.
- Lewis, E. L. (1982) The Arctic Ocean: Water Masses and Energy Exchanges, In: *The Arctic Ocean, the Hydrographic Environment and the Fate of Pollutants*, L. Rey (Editor), pp. 43-68, Wiley
- Lieser, J. L. (2005) Sea ice conditions in the northern North Atlantic in 2003 and 2004 Observations during RV POLARSTERN cruises ARKTIS XIX/1a and b and Arktis XX/2, *Berichte zur Polar- und Meeresforschung (Reports on Polar and Marine Research)*, Bremerhaven, Alfred Wegener Institute for Polar and Marine Research, **504**, 197 p.
- Losch M., D. Menemenlis, J. M. Campin, P. Heimbach P. and C. Hill (2010) On the formulation of sea-ice models: Part 1: Effects of different solver implementations and parameterizations. *Oc. Mod.*, **33(1-2)**, pp. 129-144, DOI: 10.1016/j.ocemod.2009.12.008.
- Lu P., Z. Li, B. Cheng and M. Leppäranta (2011) A parameterization of the ice-ocean drag coefficient. *J. Geophys. Res.*, **116**, C07019, doi:10.1029/2010JC006878.
- Lüpkes C. and G. Birnbaum (2005) Surface drag in the Arctic marginal sea-ice zone: a comparison of different parameterisation concepts. *Boundary-Layer Meteorology*, **117**(2), pp. 179-211, doi:10.1007/s10546-005-1445-8.

- Lüpkes C., V. M. Gryanic, J. Hartmann and E. L. Andreas (2012) A parameterization, based on sea ice morphology, of the neutral atmospheric drag coefficients for weather prediction and climate models. *J. Geophys. Res.*, **117**, D13112, doi:10.1029/2012JD017630.
- Lüpkes C., V. M. Gryanic, A. Rösel, G. Birnbaum and L. Kaleschke (2013) Effects of sea ice morphology during arctic summer on atmospheric drag coefficients used in climate models. *Geophys. Res. Lett.*, **40**, 2, pp. 446–451, doi:10.1002/grl.50081.
- Mai S., C. Wamser, and C. Kottmeier (1996) Geometric and aerodynamic roughness of sea ice, *Boundary Layer Meteorol.*, **77**(3-4), pp. 233-248, DOI:10.1007/BF00123526.
- Markus T., D. J. Cavalieri, M. A. Tschudi, and A. Ivanoff (2003) Comparison of aerial video and Landsat 7 data over ponded sea ice. *Remote Sens. Environ.*, **86**, pp. 458-469.
- Marshall J., A. Adcroft, C. Hill, L. Perelman, and C. Heisey (1997) A finite-volume, incompressible Navier Stokes model for studies of the ocean on parallel computers. *J. Geophys. Res.*, **102**(C3), pp. 5753-5766, doi:10.1029/96JC02775.
- Martin, T. (2006) Comparison of different ridge formation models of Arctic sea ice with observations from laser profiling. *Anna. Glaciol.*, **44**, pp. 403-410.
- Martin, T. (2007) Arctic Sea Ice Dynamics: Drift and Ridging in Numerical Models and Observations., PhD thesis *Ber. Polarforsch. Meeresforsch.*, **563**, ISSN 1618-3193.
- Martin T. and R. Gerdes (2007) Sea ice drift variability in Arctic Ocean Model Intercomparison Project models and observations. *J. Geophys. Res.*, **112**, C04S10, doi: 10.1029/2006JC003617.
- Maslanik J. A., C. Fowler, J. Stroeve, S. Drobot, J. Zwally, D. Yi, and W. Emery (2007) A younger, thinner Arctic ice cover: Increased potential for rapid, extensive sea-ice loss. *Geophys. Res. Lett.*, **34**, L24501, doi:10.1029/2007GL032043.
- Maykut, G. A. (1986) The surface heat and mass balance, In: *The Geophysics of sea ice*. N. Untersteiner (Editor), Springer Science. ISBN:978-1-4899-5354-4.
- McPhee, M. *Air-Ice-Ocean Interaction: Turbulent Ocean Boundary Layer, Exchange Processes* (2008), Springer-Verlag New York, DOI: 10.1007/978-0-387-78335-2.
- Melling H., and D. A. Riedel (1995) The underside topography of sea ice over the continental shelf of the Beaufort Sea in winter 1990. *J. Geophys. Res.*, **100**(C7), pp. 13641-13653, doi:10.1029/95JC00309.

- MITgcm User Manual, Online Documentation*, MIT/EAPS, Cambridge, Mass. [Available at http://mitgcm.org/public/r2_manual/latest/online_documents/manual.html.]
- Nortala-Hoikkanen A., K. Riska, O. Salmela, and G. Wilkman (1994) Methods to map ice conditions, measure ice properties and quantify ice features. *Hydrotechnical Construction*, **28**, No 3, pp. 180-188, doi:10.1007/BF01545936.
- Olason E. and D. Notz (2014) Drivers of variability in Arctic sea-ice drift speed, *J. Geophys. Res.*, **119**, pp. 5755-5775, doi:10.1002/2014JC009897.
- Overland, J. E. (1985) Atmospheric boundary layer structure and drag coefficients over sea ice. *J. Geophys. Res.*, **90**(C5), pp. 9029-9049, doi:10.1029/JC090iC05p09029.
- Parkinson C. L. and D. J. Cavalieri (2008) Arctic sea ice variability and trends, 1979-2006. *J. Geophys. Res.*, **113**, C07003, doi:10.1029/2007JC004558.
- Parmeter, R. R. (1975) A model of simple rafting in sea ice, *J. Geophys. Res.*, **80**(15), pp. 1948-1952, doi:10.1029/JC080i015p01948.
- Pite H. D., D. R. Topham and J. V. Hardenberg (1995) Laboratory Measurements of the Drag Force on a Family of Two-Dimensional Ice Keel Models in a Two-Layer Flow. *J. Phys. Oc.*, **25**, pp. 3008-3031, doi: [http://dx.doi.org/10.1175/1520-0485\(1995\)025<3008:LMOTDF>2.0.CO;2](http://dx.doi.org/10.1175/1520-0485(1995)025<3008:LMOTDF>2.0.CO;2).
- Proshutinsky A. Y. and M. A. Johnson (1997) Two circulation regimes of the wind-driven Arctic Ocean. *J. Geophys. Res.*, **102**(C6), pp. 12493-12514, doi:10.1029/97JC00738.
- Proshutinsky A. Y., R. H. Bourke, and F. A. McLaughlin (2002) The role of the Beaufort Gyre in Arctic climate variability: Seasonal to decadal climate scales. *Geophys. Res. Lett.*, **29**(23), 2100, doi:10.1029/2002GL015847.
- Rabe B., M. Karcher, U. Schauer, J. M. Toole, R. A. Krishfield, S. Pisarev, F. Kauker, R. Gerdes, T. Kikuchi (2011) An assessment of Arctic Ocean freshwater content changes from the 1990s to the 2006-2008 period. *Deep Sea Research Part I: Oceanographic Research Paper*, **58**, 2, pp. 173-185, doi:10.1016/j.dsr.2010.12.002.
- Rabenstein L., S. Hendricks, T. Martin., A. Pfaffhuber and C. Haas (2010) Thickness and surface-properties of different sea-ice regimes within the Arctic Trans Polar Drift: Data from summers 2001, 2004 and 2007. *J. Geophys. Res.*, **115**, doi:10.1029/2009JC005846.

- Rachor, E. (1997), Scientific Cruise Report of the Arctic Expedition ARK-XI-1 of RV "Polarstern" in 1995: (German-Russian Project LADI: Laptev Sea - Arctic Deep Basin Interrelation). Volume 226 of Berichte zur Polarforschung. Publisher: Alfred-Wegener-Institute für Polar- und Meeresforschung.
- Rampal P., J. Weiss, and D. Marsan (2003) Positive trend in the mean speed and deformation rate of Arctic sea ice, 1979-2009. *J. Geophys. Res.*, **114**, C05013, doi:10.1029/2008JC005066.
- Reid J., A. A. Pfaffhuber and M. Vrbancich (2006) Airborne electromagnetic footprints in 1D earths., *Geophysics*, **71**(2), DOI: 10.1190/1.2187756.
- Rigor I. G., J. M. Wallace, and R. L. Colony (2002), Response of Sea Ice to the Arctic Oscillation, *J. Climate*, **15**, pp. 2648-2663, doi: [http://dx.doi.org/10.1175/1520-0442\(2002\)015<2648:ROSITT>2.0.CO;2](http://dx.doi.org/10.1175/1520-0442(2002)015<2648:ROSITT>2.0.CO;2).
- Ropers, M. (2013) Die Auswirkung variabler Meereisrauigkeit auf die atmosphärische Grenzschicht , PhD thesis, University of Bremen. <http://epic.awi.de/34818/>.
- Rothrock, D. A. (1975) The Energetics of the Plastic Deformation of Pack Ice by Ridging. *J. Geophys. Res.*, **80**(33), pp. 4514-4519, doi:10.1029/JC080i033p04514.
- Rothrock D. A., Y. Yu, and G. A. Maykut (1999) Thinning of Arctic sea-ice cover. *Geophys. Res. Lett.*, **26**(23), pp. 3469-3472, doi:10.1029/1999GL010863.
- Rösel A., L. Kaleschke and G. Birnbaum (2012) Melt ponds on Arctic sea ice determined from MODIS satellite data using an artificial neural network. *The Cryosphere*, **6**, pp. 431-446, doi:10.5194/tc-6-431-2012.
- Rudels B., E. P. Jones, L. G. Anderson, and G. Kattner (1994) On the intermediate Depth Waters of the Arctic Ocean, In: *The Polar Oceans and Their Role in shaping the Global Environment: The Nansen Centennial Volume*, pp. 33-46, O. M. Johannessen, R. D. Muench and J. E. Overland (Editors), Washington, D. C., American Geophysical Union.
- Rudels B., H. J. Friedrich and D. Quadfasel (1999) The Arctic Circumpolar Boundary Current. *Deep-Sea Res. Part II: Topical Studies in Oceanography*, **46** 6-7, pp. 1023-1062.
- Rudels B., E. P. Jones, U. Schauer, and P. Eriksson (2004) Atlantic sources of the arctic ocean surface and halocline waters. *Polar Research*. **23**(2), pp. 181-208, ISSN 1751-8369.

- Schauer, U. (2008) The expedition ARKTIS-XXII/2 of the research vessel "Polarstern" in 2007, *Rep. Polar Res.*, 579, pp. 271. Available at <http://hdl.handle.net/10013/epic.30947>.
- Semtner, A. J. Jr. (1976) A model for the thermodynamic growth of sea ice in numerical investigations of climate. *J. Phys. Oceanogr.*, **6**, 379–389, doi: [http://dx.doi.org/10.1175/1520-0485\(1976\)006<0379:AMFTTG>2.0.CO;2](http://dx.doi.org/10.1175/1520-0485(1976)006<0379:AMFTTG>2.0.CO;2).
- Serreze M. C., J. A. Maslanik, T. A. Scambos, F. Fetterer, J. Stroeve, K. Knowles, C. Fowler, S. Drobot, R. G. Barry, and T. M. Haran (2003) A record minimum arctic sea ice extent and area in 2002. *Geophys. Res. Lett.*, **30**(3), 1110, doi:10.1029/2002GL016406.
- Serreze M. C., M. M. Holland, and J. Stroeve (2007) Perspectives on the Arctic's shrinking sea-ice cover. *Science*, **316**, 1533-1536, doi: 10.1126/science.1139426.
- Schulkes, R. M. S. M. (1995) A note on the evolution equations for the area fraction and the thickness of a floating ice cover. *J. Geophys. Res.*, **100**(C3), 5021-5024, doi:10.1029/94JC03375.
- Shinohara, Y. (1990) A redistribution Function Applicable to a Dynamic Model of Sea Ice. *J. Geophys. Res.*, **95**(C8), pp. 13413-13431, doi:10.1029/JC095iC08p13423.
- Spren G., R. Kwok, and D. Menemenlis (2009) Trends in Arctic sea ice drift and role of wind forcing: 1992-2009. *Geophys. Res. Lett.*, **38**, L19501, doi:10.1029/2011GL048970.
- Steele M., J. Zhang, D. Rothrock, and H. Stern (1989) The force balance of sea ice in a numerical model of the Arctic Ocean. *J. Geophys. Res.*, **102**(C9), pp. 21061-21079, doi:10.1029/97JC01454.
- Steele M., J. H. Morison, and N. Untersteiner (1997) The partition of air-ice-ocean momentum exchange as a function of ice concentration, floe size, and draft. *J. Geophys. Res.*, **94**(C9), pp. 12739-12750, doi:10.1029/JC094iC09p12739.
- Steiner N., M. Harder and P. Lemke (1999) Sea-ice roughness and drag coefficients in a dynamic-thermodynamic sea-ice model for the -arctic. *Tellus A*, **51**, 964-978, doi: 10.1034/j.1600-0870.1999.00029.x.
- Steiner, N. (2001) Introduction of variable drag coefficients into sea-ice models. *Annals of Glaciology*, **33**(1), pp. 181-186, DOI: 10.3189/172756401781818149.

- Stroeve J. C., M. M. Holland, W. Meier, T. Scambos, and M. Serreze (2007) Arctic sea ice decline: Faster than forecast. *Geophys. Res. Lett.*, **34**, L09501, doi:10.1029/2007GL029703.
- Stroeve J. C., M. C. Serreze, M. M. Holland, J. E. Kay, J. Malanik, and A. P. Barrett (2011) The Arctic's rapidly shrinking sea ice cover: A research synthesis. *Clim. Change*, **110**(3), pp. 1005-1027, DOI:10.1007/s10584-011-0101-1.
- Stroeve J. C., V. Kattsov, A. P. Barret, M. Serreze, T. Pavlova, M. Holland, and W. N. Meier (2012) Trends in Arctic sea ice extent from CMIP5, CMIP3 and observations *Geophys. Res. Lett.*, **39**, L16502, doi:10.1029/2012GL052676.
- Sumata H., F. Kauker, R. Gerdes, C. Köberle and M. Karcher (2013) A comparison between gradient descend and stochastic approaches for parameter optimization of a sea ice model. *Ocean Sci.*, **9**, 4, pp. 609-630, doi:10.5194/os-9-609-2013.
- Swift J. H., E. P. Jones, E. C. Carmack, M. Hingstone, R. W. Macdonald, F. A. McLaughling and R. G. Perkin (1997) Waters of the Makarov and Canada Basins. *Deep-Sea Res. Part II - Topical Studies in Oceanography*, **44**, 4, pp. 1503-1529.
- Thiede, J. (2002) Polarstern Arktis XVII/2: Cruise Report: AMORE 2001 (Arctic Mid-Ocean Ridges Expedition), *Rep. Polar Res.*, **421**, pp. 390. Available at <http://hdl.handle.net/10013/epic.10426>.
- Thomas D. N. and S. Dieckmann, *Sea Ice* (2010) Wiley-Blackwell Publications, 2nd Edition, ISBN: 978-1-4051-8580-6.
- Thorndike A. S., D. A. Rothrock, G. A. Maykut and R. Colony (1975) The Thickness Distribution of Sea Ice. *J. Geophys. Res.*, **80**(33), pp. 4501-4513, doi:10.1029/JC080i033p04501.
- Thorndike A. S. and R. Colony (1982) Sea ice motion in response to geostrophic winds. *J. Geophys. Res.*, **87**, pp. 5845-5852, doi:10.1029/JC087iC08p05845.
- Timco M. and R. P. Burden (1997) An analysis of the shape of sea ice ridges. *Cold Reg. Sci. Technol.*, **25**(1), pp. 65-77, DOI: 10.1016/S0165-232X(96)00017-1.
- Tsamados M., D. L. Feltham, D. Schroeder, D. Flocco, S. L. Farrell, N. Kurtz, S. W. Laxon, and S. Bacon (2014) Impact of variable atmospheric and oceanic form drag on simulations of Arctic sea ice. *J. Phys. Oceanogr.*, **44**, pp. 1329-1353, doi:10.1175/JPO-D-13-0215.1.
- Ukita J. and R. E. Moritz (1995) Yeld curves and flow rules of pack ice, *J. Geophys. Res.*, **100**, C3, pp. 4545-4557, doi:10.1029/94JC02202.

- Untersteiner, N. (1980) AIDJEX Review, in Sea Ice Processes and Models, edited by R. S. Pritchard, pp. 3-11, University of Washington Press, Seattle, Wash.
- Vihma T., J. Hartmann and C. Lüpkes (2003) A case study of an on-ice air flow over the Arctic marginal sea ice zone, *Boundary-Layer Meteorol.*, **107**, pp. 189-217, doi:10.1023/A:1021599601948.
- Vinje, T. E. (1982) The Drift Pattern of Sea Ice in the Arctic with Particular Reference to the Atlantic Approach, In: *The Arctic Ocean, the Hydrographic Environment and the Fate of Pollutants*, L. Rey (Editor), pp.83-96, Wiley.
- Von Saldern C., C. Haas and W. Dierking (2006) Parameterization of Arctic sea-ice surface roughness for application in ice type classification. *Anna. Glaciol.*, **44**(1), pp. 224-230, DOI: 10.3189/172756406781811411.
- Wadhams P. and R. J. Horne (1980) An analysis of ice profiles obtained by submarine sonar in the Beaufort Sea, *J. Glaciol.*, **25**, pp. 401-424.
- Wadhams P. and T. Davy (1986) On the spacing and draft distributions for pressure ridge keels. *J. Geophys. Res.*, **91**(C9), pp. 10697-10708, doi:10.1029/JC09p10697.
- Wadhams P. and J. C. Comiso (2013) The Ice Thickness Distribution Inferred Using Remote Sensing Techniques. In: *Microwave Remote Sensing of Sea Ice*, Frank D. Carsey (Editor), pp.375-383, Geophysical Monograph Series American Geophysical Union, Washington, D.C.
- Williams E., C. Swithinbank and G. de Q. Robin (1975) A submarine sonar study of Arctic pack ice. *J. Glaciol.*, **15**(73), pp. 349-362.
- Wingham D. J., C. R. Francis, S. Baker, C. Bouzinac, D. Brockley, R. Cullen, P. de Cahteau-Thierry, S. W. Laxon, U. Mallow, C. Mavrocordatos, L. Phalippou, G. Ratier, L. Rey, F. Rostan, P. Viau and D. W. Wallis. (2006) CryoSat: A mission to determine the fluctuations in Earth's land and marine ice fields. *Advances in Space Research*, **37**, pp. 841-871.
- Winton, M. (2011) Do climate models underestimate the sensitivity of Northern Hemisphere sea ice cover? *J. Clim.*, **24**(15), pp. 3924-3934, DOI:10.1175/2011JCLI4146.1
- Yang J., and J. C. Comiso (2007) An unexpected seasonal variability of salinity in the Beaufort Sea upper layer in 1996-1998. *J. Geophys. Res.*, **112**, C05034, doi:10.1029/2004JC002716.
- Yang, J. (2009) Seasonal and interannual variability of downwelling in the Beaufort Sea. *J. Geophys. Res.*, **114**, C00A14, doi:10.1029/2008JC005084.

- Zhang J. and W. D. Hibler III (1997) On an efficient numerical method for modeling sea ice dynamics. *J. Geophys. Res.*, **102**(C4), pp. 8691-8702, doi:10.1029/96JC03744.

Acknowledgments

I am grateful to Prof. Rüdiger Gerdes, my supervisor, for giving me the opportunity of a PhD at AWI. During these three years he always supported my research and he always found some time to discuss ideas and results. He has been able to listen and understand my needs as a PhD and as a person. I highly appreciate his interest in my new ideas and opinions, and mostly his ability to give me freedom but on the same time to guide me towards the right goal. Finally, thanks to him I now know all the 6 seasons of "The big bang theory".

I thank Dr. Michael Bau, Jacobs University, for being part of my dissertation committee.

I thank Christof Lüpkes for his patience in listening, for his ability of moderating my excessive enthusiasm and for all his detailed comments and suggestions. I am grateful for the time he spent working with me, not only on working days but also on Saturdays, Sundays and holidays.

Martin Losch helped me with the MITgcm and, with a lot of patience, he guided my first (and last) steps in the numerical implementation of the code. He constantly challenged my work and my ideas, but he also found the right word to give me the motivation that, sometimes, was missing.

Rüdiger, Martin and Christof always attended my PhD committee meetings. Their suggestions, comments and feedbacks helped me to grow as a scientist and as a researcher.

I am especially grateful to Karel. She revised big part of my PhD thesis and she offered a lot of support during the last period of my work. In these three years she has always been a "safe harbor" for talking, asking suggestions and getting (a lot of) moral support.

Many thanks go to the group of the "modelers-lunch", in particular to Polona, Karel, Kathrin, Malte, Hiroshi, Adriana, Michael, Frank, Cornelia, Ingrid. With them I had the possibility to discuss large part of my results and to develop new ideas.

The entire sea ice physics group supported my work, especially Thomas, Stefan, Marcel, Sandra and my colleagues Phd students: Robert, Lera, Polona, Priska, Steffi, Christian and last but not least Mario, with whom I shared the office, many desperate moments, and, sometimes, Nutella.

In particular, thanks to Robert and Lera for the coffee breaks, for their hugs, for their presence in the "I need to talk" moments, for the dinners together and for the days spent working, doing sports, playing games.

A special thanks to Michael Schröder for offering me the possibility to join the Polarstern cruise ANTXXIX/9 and thus to realize my big dream to see Antarctica. I also thank the CTD team and Sandra with whom I worked on board and shared this wonderful experience.

AWI is a great institute and it offered me the possibility to attend conferences and to discuss my results in a high level and interdisciplinary environment.

I thank the graduate school ESSReS, and especially Stefanie Klebe. ESSReS offered plenty of courses to help developing personal skills, but also to widen the field of research towards a more interdisciplinary approach. I thank ESSReS for supporting economically my research, for offering a good platform for discussing my experience and problems as PhD student, and for offering many excursions and social events that brought the students to share experiences and mostly a lot of fun.

I thank my closest friends Alex, Robert, Ilaria. Their friendship and love were constantly with me during these three years (and more) and helped me to move the hardest steps in my work as well as in personal life. Thanks!

Thanks to all my friends: Marco, Roberta, Babara, Anika, Marius, Carmen, Ella, Quentin, Francesca, Mauro, Charlotte, Shobhit, Yasemin, Jean, Julie, Tim, Ingrid, Ivan, Rafa, Fabio, Roy ... and many others, for being always ready for a chat, a beer, a walk, a dinner, a party, a day of hangover, a barbecue ... because where you have good friends you feel at home.

Finally, I am gratefully to my family for their encouragement and endless love. Thanks to mom Rosalba, for being able to move the steps that I couldn't. Thanks to dad Giovanni for being always able to read me and to see what I was not able to. Thanks to Marco and Erica for the chats, the laughs, the fights and all the love they gave me. Thanks to Ash who is always, patiently, here with me.

And thanks to me, for never stop dreaming.